2024

Altitude and Pitch Control of a Tethered Multi-Rotor Autogyro Using a Reduced Order Model

Tasnia Noboni
University of Central Florida

STARS Citation

Noboni, Tasnia, "Altitude and Pitch Control of a Tethered Multi-Rotor Autogyro Using a Reduced Order Model" (2024). *Graduate Thesis and Dissertation 2023-2024*. 453.
https://stars.library.ucf.edu/etd2023/453

ALTITUDE AND PITCH CONTROL OF A TETHERED MULTI-ROTOR AUTOGYRO USING A REDUCED ORDER MODEL

by

TASNIA NOBONI
B.Sc. Bangladesh University of Engineering and Technology, 2019

A thesis submitted in partial fulfilment of the requirements
for the degree of Master of Science
in the Department of Mechanical and Aerospace Engineering
in the College of Engineering and Computer Science
at the University of Central Florida
Orlando, Florida

Spring Term
2024

Major Professor: Tuhin Das

ABSTRACT

Long-duration deployment of UAVs for surveillance and communication purposes can be very energy-consuming and expensive. Tethered autogyro-based UAVs can provide an energy-efficient solution to this problem and produce energy in the presence of a strong and persistent wind field at higher altitudes. Instead of using an engine, the unpowered autogyro rotors produce lift by creating an upward thrust force while relative airflow passes up through the rotor blades. The tether provides mooring action and can be used bidirectionally for transmitting or receiving power from the autogyro. Thus, tethered autogyros can address recent environmental concerns by reducing carbon footprint via efficient use of renewable energy resources. This thesis presents a simple model-based altitude and pitch control method of a tethered multi-rotor autogyro as a starting step to make a contribution towards green technology in the low-altitude surveillance field.

This study adopts a quad-copter-based autogyro, connected to the ground by a tether, for modeling in the 2D plane assuming that the roll and yaw motions of the system are already being controlled by the rotors in the lateral direction which simplifies the highly nonlinear system by decreasing the number of states. Blade-Element-Momentum (BEM) theory combined with static catenary mechanics is employed to model the aerodynamic forces and tether tension which results in producing the equations of motion of the system. The equations of motion are solved to study transient behavior and characterize the equilibrium space of the tethered system, thereby identifying optimal operating ranges associated with the rotors' tip-speed ratio and the system's pitch angle.

A proportional-feedback controller is designed and a stability analysis is conducted for pitch actuation and altitude tracking of the system. Results suggest that the proportional controller efficiently tracks the higher reference altitude in both uniform and variable wind fields. However, it cannot track the reference altitude set at less than 85% of the tether length. This prompts the design of a PD-feedback controller. Stability analysis and simulation results show that the PD controller is more effective in modulating pitch and controlling the autogyro's altitude using the restoring effect from the tether tension within the entire operating region.

To my parents and my husband for their constant support. To my niece, Agnee, whose smile always keeps me sane.

ACKNOWLEDGMENTS

I am sincerely grateful to my supervisor, Dr. Tuhin Das, for providing me with the opportunity to work on this project and for his academic guidance and mental support to carry out this research. I would also like to acknowledge and thank the National Science Foundation (NSF), the funding agency of this project, for its financial support.

TABLE OF CONTENTS

LIST OF FIGURES

LIST OF TABLES

NOMENCLATURE

α_A, α_B	Angle of incidence at rotor A & B
β	Pitch angle
δ	Average drag coefficient
η_0	Tether angle at the base with horizontal
η_1	Tether angle at the autogyro with vertical
γ	Non-dimensional mass constant
λ_A, λ_B	inflow ratio of rotor A & B
μ_A, μ_B	Tip speed ratio of rotor A & B
Ω_1, Ω_2	Angular velocity of rotor A & B
ρ	Density of air
σ	Blade disc solidity
σ_t	Mass per unit length of tether
θ_0	Blade pitch angle at hub
θ_1	Blade pitch slope
ζ, q	Tether parameters
a	Slope of lift curve
a_0, a_1, b_1, a_2, b_2	Fourier coefficients

B	Blade radius fraction less tip losses
b	Number of blades
c	Blade chord
C_{t_1}, C_{t_2}	Rotor thrust coefficient
d_c	Damping constant
g	Acceleration due to gravity
I	Blade moment of inertia about flapping hinge
I_c	Moment of inertia of the system about center point C
I_r	Rotor moment of inertia
l	Length of frame
l_t	Length of tether
m_a	Total mass of the autogyro including frame
m_t	Mass of tether
M_W	Flapping moment from blade weight
Q_1, Q_2	Aerodynamic Torque about rotor A & B
q_1, q_2	Braking Torque about rotor A & B
R	Blade radius
T_0, T_t	Tether tension at the base and at the end
T_1, T_2	Thrust force in rotor A & B

V_w	Wind velocity
$V_{w/A}, V_{w/B}$	Relative wind velocity experienced by rotor A & B
x, z	Autogyro drift & altitude
x_e, z_e	Equilibrium point along the x-z axis
z_d	Desired altitude

CHAPTER 1: INTRODUCTION

1.1 Motivation

Today's fast-paced era identified with rapid technological advancement along with lacking concern about its effects on the environment is calling for environment-friendly alternatives to every high-tech invention. Following this thread, an environment-friendly surveillance system will be required in no time. To ensure public safety, mass control in crowded areas, air quality monitoring, nature conservation and achieve high-resolution surveillance data, the importance of low-altitude surveillance systems is immense. Drones can be distinguished as the most prominent technology in this field. Studies have been made to expand drone's usability not only for surveillance purposes but also as an aid to access remote areas [5], air delivery [6], ecological study of population [7] and so on. It is true that aerial surveillance sectors have achieved agility by expanding drone technologies. However, drones as a surveillance medium also face limitations. One of the limitations is short flight time due to its fuel capacity and battery life. Generally, drones have limited payload capacity which also affects the resolution of surveillance systems. Another important concern for the rapidly growing drone industry is the disposal of lithium-ion batteries as they contain harmful substances [8]. Also, fossil fuel-powered drones emit CO_2 in the environment. Aerostats are also popular big-scale aerial surveillance systems that produce lift using lighter-than-air gas by creating buoyant force. However, they require a consistent helium gas supply and continuous power supply from the ground.

A tethered autogyro system can alleviate the above-mentioned problems associated with drones and aerostats due to its ability to use wind energy for free rotation with its unpowered rotors. To replace drones and aerostats as effective surveillance systems, autogyro must have the ability to hover at different altitudes. Tether provides mooring action to the system that can facilitate hovering. However, there is sparse literature available on the altitude and stability control of such tethered autogyro systems. The motivation behind this thesis is to contribute to the establishment of an environment-friendly surveillance system by conducting an altitude control study of the tethered autogyro using model-based appraoch.

Tethered autogyros can serve dual purposes and they are: low-altitude surveillance medium and high-altitude energy extraction devices. From the limited research done on the tethered autogyro in the literature, it is evident that researchers have mostly studied the high-altitude energy extraction aspect of such systems where stronger and more persistent wind is available. In contrast, in this study, the focus is on the dynamic modeling of lightweight autogyros that can hover at lower altitudes. Furthermore, the developed dynamic model leaves the scope for changing the system into a heavy-weight autogyro system ideal for high-altitude energy extraction by changing the tether length and using proper inertia properties. This thesis should be considered as an introductory study of simple model-based control analysis of tethered autogyro for altitude and pitch control for surveillance within a confined area. Although for such cases continuous autorotation is not guaranteed due to the lack of consistency of wind speed in lower altitudes, the developed system can sustain hovering with the help of the tether's reeling action or by intermittent powering of the rotors. The overall system operates sustainably and regenerative braking torques in the mounted rotors are used for attitude and altitude control.

1.2 Thesis Objectives

This thesis aims to explore the feasibility of braking torque to be used as a control input for pitch modulation and altitude tracking of a tethered multi-rotor autogyro by taking the transient response of the system into account. This target is accomplished in incremental steps by completing the following objectives -

1. Modeling the system dynamics to capture both the transient and steady-state response by extending the steady-state model of small, light autogyro from [4, 9]
2. Analyzing the characteristics of equilibria of the system with the developed dynamic model with respect to the system's pitch angle and rotors' tip-speed ratio and also identification of the plausible operating regions of the system
3. Formulation of control algorithms that enable the system's altitude to converge to the reference altitude in both uniform and variable wind fields
4. Derivation of an approximate closed-loop dynamics of the coordinate representing altitude that explains the effectiveness of designed controllers
5. Implementation of the designed controllers on the developed model and evaluation of controller performance through simulation

A reduced-order model of a multi-rotor tethered autogyro system is considered in this study to demonstrate the viability of altitude and pitch control using the rotor braking technique. The use of regenerative braking for control purposes is a novel concept for such rotorcrafts. The feasibility of this technology is explored within a 2D framework. The modeling of the system in 2D helps alleviate some of the complexities of modeling such a highly nonlinear system and aids in staying focused on the main goal of this research by outlining important control characteristics of the system.

1.3 Thesis Outline

The rest of the thesis is divided into six chapters. In Chapter 2, a literature review on the existing tethered aerial device, the extant autogyro model and the existing control strategies of such systems is presented. Chapter 3 discusses the dynamic modeling of a tethered autogyro system in detail. The characteristics of equilibria are explored and the operating regions are identified through simulation for the developed tethered autogyro model in Chapter 4. Chapter 5 introduces the control strategies designed for such a system. Furthermore, the stability analysis of the designed controllers is conducted. Simulation results showing the performance of the controllers in both uniform and variable wind fields are presented in Chapter 6 which also expounds the performance comparison between two different controllers. Finally, Chapter 7 summarizes the contributions of this thesis and discusses the possible future expansions of the model.

CHAPTER 2: LITERATURE REVIEW

2.1 Tethered Aerial Devices

Tethered aerial devices have recently become popular for capturing wind power, especially at higher altitudes [10]. With regard to harvesting wind power, aerial devices are also known as airborne wind energy systems (AWEs). They can be categorized according to their characteristics for example, weight- Lighter than Air (LTA), Heavier than Air (HTA), and the aerodynamics properties -Helicopter, Airfoil, and Aerostat, Autogyro [11]. The tethers in such systems are required to transfer the energy down to the ground. Among the popular AWEs designs proposed by the researchers, tethered kite systems are the most popular in literature [1, 2, 12, 13, 14, 15, 16, 17, 18, 19].

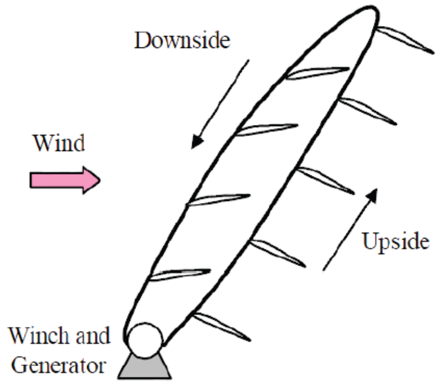

Figure 2.1: Original Laddermill design from [1]

Williams et al. [14, 15, 16] adopted a single kite setup connected to a movable base with a variable length tether for designing a control algorithm with a combination of tether length, roll angle and angle of attack of the kite to extract wind energy. The Laddermill setup [1, 13], shown in Fig. 2.1,

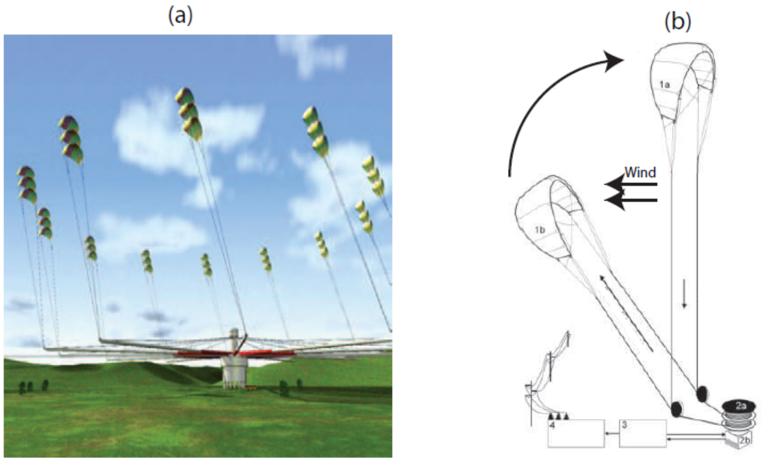

Figure 2.2: (a) The Kitegen setup [2], (b) Schematic of single Kitegen unit

is composed of several kites in series connection and can drive an electric generator with a single cable. Canale et al. [17, 2] introduced the concept of Kitegen with several kites with a circular base foundation. The base is installed on, as shown in Fig. 2.2, arms of a vertical axis rotor to generate power.

Tethered aerostats, shown in Fig. 2.3, are another popular aerial device, especially in the surveillance field and communication sector [20, 21, 22]. Aerostats fall into the category of lighter-than-air devices [23] as they use helium gas to create buoyancy force for producing lift. Jones and Krausman [24] studied tethered aerostat system's response to turbulence and other disturbances via developing a nonlinear dynamic simulation computer program. A dynamics analysis of a tethered aerostat was presented by Lambert and Nahon [25] using a component breakdown approach and the tether is modeled using a lumped mass approach. Rajani et al. [26] studied the stability characteristics of aerostats and also presented an equilibrium analysis for such a system. Hot-air

Figure 2.3: Tethered aerostat radar system [3]

balloons are another type of aerial surveillance device, the autonomous maneuverability of which was investigated by posing it as an optimal control problem in [27].

Researchers have recently been interested in exploring the potential of tethered systems as wind energy harvesting devices. Floating offshore wind turbine modeling [28] and mooring system design [29, 30] have drawn significant attention from researchers for harvesting wind energy due to the abundance of offshore wind. The contemporary design of tethered autogyro as a wind energy harvesting device can also be found in the literature [9]. However, inadequate studies are found in the literature regarding the tethered autogyro system in the context of being used for surveillance purposes as mentioned in Chapter 1. The next two sections are dedicated to presenting the reviews of the existing literature on autogyro modeling and control.

2.2 Autogyro Modeling

Following the successful piloted flight of autogyro in the early by its inventor Juan de la Cierva, the early development of the steady-state model of autogyro employing the blade element momentum

(BEM) approach [31] was initiated by Glauert [32]. In this model, a constant pitch of the rotor blade was considered and a higher power of tip speed ratio was ignored by the author. A theoretical model of autogyro was developed by Lock [33, 34] that included the higher power of the tip-speed ratio of the rotor in the model. Wheatley [4, 35] proposed a detailed autogyro model by introducing a linear variation in pitch and periodic blade twist and also validated the result experimentally using a commercial autogyro available at that time. The fascinating chronicle of autogyro development of 80 years time span was presented in [36]. The forward and vertical flight performances of the autogyro were given in [37] and the performance of an autogyro was compared with that of a helicopter. The blade element-momentum theory was modified by Cuerva et al. [38] to explain vertical autorotation in the context of the helicopter. In fact, most of the theories regarding autorotation came from the analysis of the autorotation phase of helicopters [39, 40, 41]. However, constant and high rotor speed can be assumed in mathematical modeling for helicopters to study autorotation, this assumption is not valid for autogyro. A multi-body model of rigid bodies in autorotation was proposed by Seter and Rosen [42] using the Newton-Euler approach. Houston [43] investigated the relationship between the rotor speed and longitudinal low-frequency rigid-body modes of autorotative rotorcraft. The effect of design parameters of autogyro on the limiting speeds of autorotation was described by McCormick [44] via a numerical model.

Roberts et al. [45] proposed a tethered quadcopter-based setup for harvesting power from an airborne wind energy (AWE) device at high altitudes. Following that, researchers have recently started to explore more about the autogyro's harvesting power [46, 47, 48, 49, 50, 9] at higher altitude. The theory of the autogyro was reviewed in [46] as an initial study to investigate the feasibility of it as an energy harvesting device. Das et al. [51] investigated the stable equilibrium characteristics of a tether-airfoil system mounted on a horizontally movable base. Author of [47] also analyzed a mathematical model of a tethered-airfoil system and designed a lab-scale experimental setup to generate experimental results for validation purposes.

In [48], a simple dynamic model of an untethered autogyro with a single rotor was presented. A fixed inertial frame fixed with the rotational axis of the rotor was considered for developing the dynamic model presented in [49, 50] to explore the effect of regenerative braking on the steady-state behavior of such autogyro. McConnell and Das [9] investigated the equilibrium behavior of a tethered autogyro for both cases of high-altitude power generation and low-altitude surveillance with a steady steady model. Expanding the work of [4, 9], authors of [52] developed a dynamic model of quad-copter-based tethered autogyro by taking a causal approach to reformulating the aerodynamic equations from the steady-state model of [4, 9] that is suitable for lower altitude.

2.3 Autogyro Control

A tethered multi-rotor autogyros has the potential to replace drones and aerostats as energy-efficient unmanned aerial vehicles (UAVs). However, it requires control analysis and stability investigation of autogyro on a flight. Rye [53] conducted longitudinal stability analysis of such a system assuming straight massless tether. Houston [54] identified the longitudinal stability of an autogyro based on the analysis test data recorded during flight trials of VPM M16 autogyro with teetering rotor blades. Dynamic stability analysis to small disturbances is performed in [55] for a hybrid autorotating rotor. Among recent studies, Ma et al. [56] proposed an altitude and pitch control technique using a PID controller for vehicular towed autogyro where the tether is modeled as a massless rod. Rezgui and Lowenberg [57] investigated the nonlinear periodic behaviour of a teetering rotor operating in autorotation using numerical continuation and bifurcation techniques to address instabilities in such systems. They [58] also explored the factors that lead to rotation-flap blade instability at high advance ratios through wind tunnel tests of a scaled teetering autogyro. A predictor-based model reference adaptive control (PMRAC) for a small hybrid autogyro was designed by Hau et al. [59] which can compensate for the system uncertainties in longitudinal

Motion.

To sum up, the research focusing on the control and stability study of a quadcopter-based tethered autogyro at a lower altitude for surveillance purposes is still in its nascent phase. Most of these existing works are heavily dependent on experimental data. Therefore, this highly technology-dependent time demands an in-depth understanding of the behaviour of such systems via rigorous experiments, modeling and control studies to bring this technology into practical application. Therefore, the contributions of this thesis lie in pushing the development of this technology forward by doing a pitch modulation and altitude control study by adopting a model-based approach.

CHAPTER 3: DYNAMIC MODEL OF THE TETHERED AUTOGYRO SYSTEM

This chapter explains the steps taken to develop a complete dynamic model of a tethered autogyro by expanding the steady-state model from [9]. The developed steady-state model of the tethered autogyro with one rotor in [9] employed the Blade Element Momentum theory (BEM). In this thesis, the equations from [4, 9] are adapted according to the dynamic multi-rotor setup considered in this study.

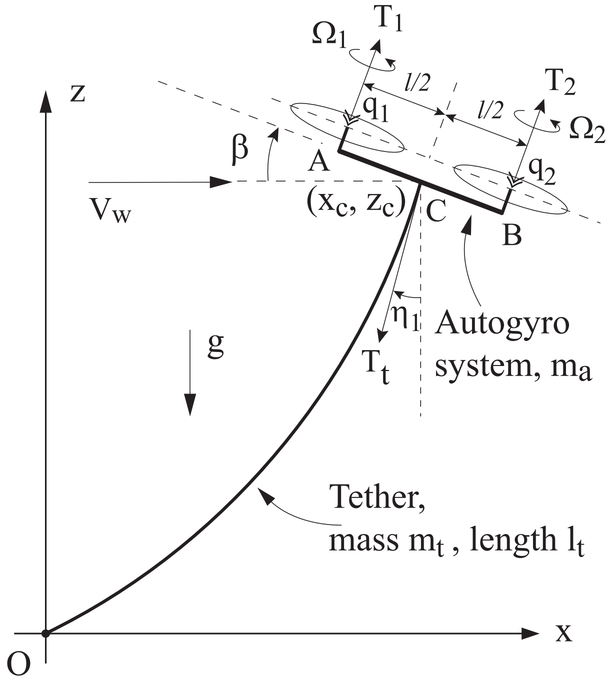

Figure 3.1: Two-dimensional tethered autogyro with two rotors connected by a frame of length *l*.

The autogyro studied in this thesis has a multi-rotor mechanism and is connected to the ground by an inextensible tether as shown in Fig.3.1. The rotors are connected by a frame having the length *l*. The ground has been considered as the inertial frame with the origin being the connection point of the tether. The blades of the rotors are allowed to flap about their respective roots. This flapping motion relieves a significant amount of the rolling and pitching motions of each rotor which is caused by uneven force distributions. This chapter is categorized into three sections which describe the development of equations of motion, aerodynamic forces and torques, and catenary equations to capture the transient behaviour of the system.

3.1 Equations of Motion

The development of the equations of motion (EOM) is done under the assumption that the thrust force in each rotor is always along the rotor axis. The roll and yaw motions of the whole system are assumed to be already controlled by the other two rotors in the lateral direction. This assumption allows the system to be studied in the X-Z plane leaving only two rotors to model. It is also assumed that the system experiences wind in the horizontal direction and no wind is available in the lateral direction. Tether is considered to be unaffected by the wind. From the geometric setup shown in Fig.3.1, the equations of motion (3.1)-(3.3) are associated with the horizontal position x_c, vertical position z_c of the point C in Fig.3.1 and pitch angle β of the autogyro respectively.

$$m_a\ddot{x}_c = T_1\sin\beta + T_2\sin\beta + d_c(V_w - \dot{x}_c) - T_t\sin\eta_1 \tag{3.1}$$

$$m_a\ddot{z}_c = T_1\cos\beta + T_2\cos\beta - d_c\dot{z}_c - T_t\cos\eta_1 - m_a g \tag{3.2}$$

where, d_c, the damping coefficient, is introduced in the equations to add damping to the system. Rotor thrust forces T_1, T_2 and tether tension T_t comes from the aerodynamic model explained in 3.2 and catenary model described in 3.3 respectively.

$$I_c\ddot{\beta} = \frac{l}{2}(T_1 - T_2) \tag{3.3}$$

where, I_c is the moment of inertia of the frame about its center point C in Fig.3.1. The arrangement of the system yields the difference in two thrust forces T_1, T_2 in rotors A and B that causes the system's pitch angle β to change when braking torque q_1 in Eq.(3.4) or q_2 in Eq.(3.5) is applied.

$$I_r\dot{\Omega}_1 = Q_1 + q_1 \tag{3.4}$$

$$I_r\dot{\Omega}_2 = Q_2 + q_2 \tag{3.5}$$

where, I_r is the moment of inertia of each rotor about its rotational axis, R is the radius of the blade, Q_1, Q_2 are the aerodynamic torque of rotor A and B respectively. The braking torques, q_1 and q_2, alter rotational speeds Ω_1 and Ω_2 of each rotor about its respective shaft which is a crucial element in the aerodynamic properties of the system described in 3.2. It causes a difference between the thrust forces of the system that subsequently leads to the change in position of the system.

3.2 Aerodynamic Model of the System

The aerodynamic model of the tethered autogyro considered in this thesis is largely adopted from [9] where the steady-state model from [4] is considered as the basis to study steady autorotation of a tethered autogyro with a single rotor. In the Blade Element Momentum theory (BEM), a rotor blade is discretized into thin strips at where forces are analyzed separately [31]. Then forces are integrated over the blade span to get averaged over one full rotation. Wheatley in [4] derived the average thrust and average rotor torque expressions using the BEM approach that is used in [9] to study equilibrium space. As one of the main objectives of this study is to investigate dynamic behavior, the aerodynamic equations of [4] are rearranged causally and solved in such a way so that they can apprehend the transient behavior of the system.

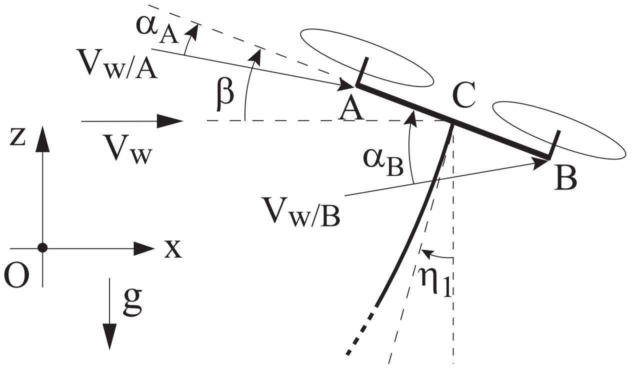

Figure 3.2: Geometric setup to demonstrate relative velocity and angles of incidence.

Figure.3.2 illustrates the rotors A and B experiencing relative wind velocity at angle α_A and α_B respectively from the oncoming horizontal wind with the speed of V_w.

$$\begin{aligned}\vec{V}_{w/A} &= \left(V_w - \dot{x}_c - \frac{l}{2}\dot{\beta}\sin\beta\right)\hat{\imath} - \left(\dot{z}_c + \frac{l}{2}\dot{\beta}\cos\beta\right)\hat{k}\\ \vec{V}_{w/B} &= \left(V_w - \dot{x}_c + \frac{l}{2}\dot{\beta}\sin\beta\right)\hat{\imath} - \left(\dot{z}_c - \frac{l}{2}\dot{\beta}\cos\beta\right)\hat{k}\end{aligned} \tag{3.6}$$

V_w and initial states are provided to Eq.(3.6) to calculate $\vec{V}_{w/A}$ and $\vec{V}_{w/B}$. Relative wind speeds experienced by both the rotors are the resultant of Eq.(3.6) shown in Eq.(3.7).

$$\begin{aligned}|V_{w/A}| &= \sqrt{\left(V_w - \dot{x}_c - \frac{l}{2}\dot{\beta}\sin\beta\right)^2 - \left(\dot{z}_c + \frac{l}{2}\dot{\beta}\cos\beta\right)^2}\\ |V_{w/B}| &= \sqrt{\left(V_w - \dot{x}_c + \frac{l}{2}\dot{\beta}\sin\beta\right)^2 - \left(\dot{z}_c - \frac{l}{2}\dot{\beta}\cos\beta\right)^2}\end{aligned} \tag{3.7}$$

Angle of incidence α_A and α_B are calculated using Eq.(3.8).

$$\begin{aligned}\alpha_A &= \beta - \tan^{-1}\frac{\dot{z}_c + \frac{l}{2}\dot{\beta}\cos\beta}{V_w - \dot{x}_c - \frac{l}{2}\dot{\beta}\sin\beta}\\ \alpha_B &= \beta - \tan^{-1}\frac{\dot{z}_c - \frac{l}{2}\dot{\beta}\cos\beta}{V_w - \dot{x}_c + \frac{l}{2}\dot{\beta}\sin\beta}\end{aligned} \tag{3.8}$$

Equations (3.6)-(3.8) have been derived using kinematic analysis of the system. Two dimensionless ratios are very important for the aerodynamic modeling of an autogyro according to [4]. They are tip speed ratio μ and inflow ratio λ. Tip speed ratio, μ, shown in Eq.(3.9), is the ratio of the wind speed parallel to the rotor disc to the tip speed of the rotor blade.

$$\begin{aligned} \mu_A &= \frac{|V_{w/A}|\cos\alpha_A}{\Omega_1 R} \\ \mu_B &= \frac{|V_{w/B}|\cos\alpha_B}{\Omega_2 R} \end{aligned} \tag{3.9}$$

The inflow ratio, λ, is the ratio of total wind speed perpendicular to the rotor disc to the tip speed of the rotor blade. Calculation of λ is not as straightforward as μ. It requires a simultaneous numerical approach entangled with the flapping angle of the blade.

Blade element setup in Fig. 3.3 demonstrates that the relative wind speeds derived in Eq.(3.7) can be resolved into three directions U_T, U_P and U_R. U_T is defined to be perpendicular to the center of rotation and blade span and parallel to the rotor disk. U_P is the parallel flow to the center of rotation i.e z-axis and perpendicular to U_T. U_R is parallel to the blade span and perpendicular to U_T which can be neglected due to the long blade assumption. U_T and U_P can be expressed as EQs.(3.10) according to [4].

$$\begin{aligned} U_T &= \Omega r + \mu\Omega R \sin\psi \\ U_P &= \lambda\Omega R - r\frac{d\theta_f}{dt} - \mu\Omega R \sin\theta_f \cos\psi \end{aligned} \tag{3.10}$$

The flapping motions of the hinged rotor blades at the base balance rolling torque of the rotor. A periodic function dependent on the blade's angular position ψ, approximates the flapping angle of the blade where $\dot{\psi} = \Omega$. The periodic function given in Eq.(3.11) is assumed as a truncated Fourier

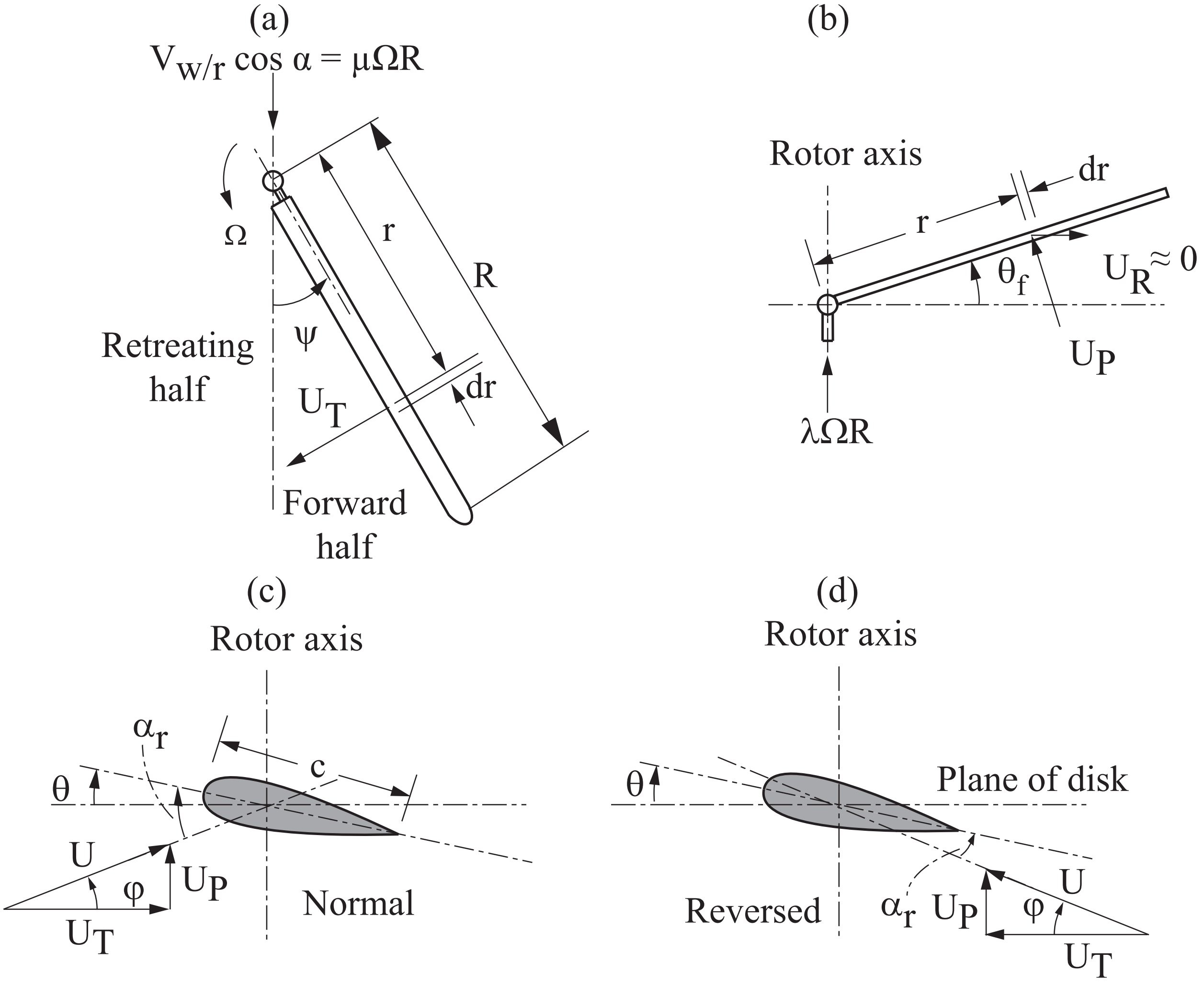

Figure 3.3: Blade element views of one rotor adopted from [4]: (a) Top view of the rotor with angular position ψ of the blade; (b) Side view showing flapping motion with flapping angle θ_f; (c) Cross-sectional view of blade element; (d) Reversed Velocity Region

series containing five coefficients-a_0, a_1, b_1, a_2 and b_2 in [4].

$$\theta_f = a_0 - a_1 \cos\psi - b_1 \sin\psi - a_2 \cos 2\psi - b_2 \sin 2\psi + \dots \tag{3.11}$$

The flapping angle of each blade needs to be phase-shifted in ψ by 90° from the adjacent blade in the 4-blade rotor assumed in this model. These Fourier coefficients are expressed as functions of λ and μ in [4] and can be reformulated as a matrix equation expressed by Eq.(3.12).

$$\begin{bmatrix} 1 & 0 & 0 & 0 & v_{15} \\ 0 & 1 & 0 & 0 & v_{25} \\ v_{31} & 0 & 1 & v_{34} & 0 \\ 0 & v_{42} & 0 & 3 & v_{45} \\ v_{51} & 0 & v_{53} & v_{54} & 3 \end{bmatrix} \begin{bmatrix} a_0 \\ a_1 \\ b_1 \\ a_2 \\ b_2 \end{bmatrix} = \begin{bmatrix} A_0 \\ A_1 \\ 0 \\ A_3 \\ 0 \end{bmatrix} \lambda + \begin{bmatrix} C_0 \\ C_1 \\ 0 \\ C_3 \\ 0 \end{bmatrix} \tag{3.12}$$

where, elements of the 5x5 matrix, v_{ij}, are functions of a non-dimensional mass constant γ, tip-speed ratio μ, blade radius tip loss factor B which accounts for the tip losses of the blade, making the effective radius of the blade BR. In the reversed flow region shown in Fig. 3.3(d), the blade creates lift in a small part and the remaining section is in stall condition. The region that creates lift in the blade is from $-\mu R \sin\psi$ to BR. Equation.(3.13) refers to the expression of v_{ij}.

$$\begin{gathered} v_{15} = -\frac{1}{16}\gamma\mu^2 B^2 \\ v_{25} = \frac{2\mu B^3}{3(B^4 - \frac{1}{2}\mu^2 B^2)} \\ v_{31} = \frac{-4\mu B}{B^2 + \frac{1}{2}\mu^2}\left(\frac{1}{3} + \frac{0.035\mu^3}{B^3}\right), v_{34} = \frac{-4\mu B}{6(B^2 + \frac{1}{2}\mu^2)} \\ v_{42} = -\frac{1}{6}\gamma\mu B^3, v_{45} = -\frac{1}{4}\gamma B^4 \\ v_{51} = \frac{1}{8}\gamma\mu^2\left(B^2 - \frac{\mu^2}{6}\right), v_{53} = -\frac{1}{6}\gamma\mu B^3, v_{54} = \frac{1}{4}\gamma B^4 \end{gathered} \tag{3.13}$$

A_0, A_1 and A_3, the coefficients associated with λ, are also functions of γ, μ and B as given in Eq.(3.14).

$$
\begin{aligned}
A_0 &= \frac{1}{2}\gamma\Big(\frac{1}{3}B^3 + 0.080\mu^3\Big) \\
A_1 &= \frac{\mu(4B^2 - \mu^2)}{2(B^4 - \frac{1}{2}\mu^2 B^2)} \\
A_3 &= \frac{-0.053}{2}\gamma\mu^3
\end{aligned}
\tag{3.14}
$$

C_0, C_1 and C_3 in the right-hand side of Eq.(3.12) considers blade pitch angle θ which is considered to vary along the radial distance r of the blade maintaining the relation $\theta = \theta_0 + (r/R)\theta_1$. θ_0, θ_1 are defined in the nomenclature. Blade weight moment term of C_0 in Eq.(3.15) $\frac{M_w}{I\Omega^2}$ is neglected in [4] but considered in [9]. It is also considered in the dynamic model of autogyro because in autorotation of autogyro, rotor speed Ω is much lower than the autorotation of a powered rotor used in a helicopter that is mainly considered in [4].

$$
\begin{aligned}
C_0 &= \frac{1}{2}\gamma\Big\{\frac{\theta_0}{4}\Big(B^4 + \mu^2 B^2 - \frac{1}{8}\mu^4\Big) + \frac{\theta_1}{5}\Big(B^5 + \frac{5}{6}\mu^2 B^3\Big)\Big\} - \frac{M_w}{I\Omega^2} \\
C_1 &= \frac{2\mu}{B^4 - \frac{1}{2}\mu^2 B^2}\Big(\frac{4}{3}\theta_0 B^3 + 0.106\theta_0\mu^3 + \theta_1 B^4\Big) \\
C_3 &= -\frac{1}{2}\gamma\mu^2\Big\{\frac{\theta_0}{4}\Big(B^2 - \frac{1}{8}\mu^2\Big) + \frac{1}{6}\theta_1 B^3\Big\}
\end{aligned}
\tag{3.15}
$$

The non-dimensional mass constant γ is defined as following Eq.(3.16).

$$
\gamma = \frac{c\rho a R^4}{I} \tag{3.16}
$$

where, c is the blade chord, ρ is the density of air, a is the lift-curve slope and I is blade moment of inertia about the flapping hinge. Equation (3.17) can be derived from Eq. (3.12) and solved for 5x1 coefficient matrix ρ_c if λ is known.

$$
\rho_c = v^{-1}A\lambda + v^{-1}C_f \tag{3.17}
$$

where, $\rho_c = [a_0\ a_1\ b_1\ a_2\ b_2]^T$. Then, a_1 and b_2 from Eq. (3.12) are expressed as linear functions of λ shown in Eq. (3.18) and Eq. (3.19) to simplify the calculation of coefficient of rotor thrust C_t.

$$a_1 = m_0\lambda + m_1 \tag{3.18}$$

$$b_2 = s_0\lambda + s_1 \tag{3.19}$$

where, $m_0 = A_1$, $m_1 = -v_{25}b_2 + C_1$, $s_0 = 0$, and $s_1 = \frac{-1}{3}-1(v_{51}a_0 + v_{53}b_1 + v_{54}a_2)$.

The relation of C_t and λ given in [4], can be rearranged as Eq. (3.20).

$$C_t = p_0 + p_1\lambda + p_2 b_2 + p_3 a_1 \tag{3.20}$$

where, p_0, p_1, p_2 and p_3 are defined in Eq.(3.21).

$$\begin{gathered}
p_0 = \frac{1}{2}\sigma a\Big\{\theta_0\Big(\frac{1}{3}B^3 + \frac{1}{2}\mu^2 B - \frac{4}{9\pi}\mu^3\Big) + \theta_1\Big(\frac{1}{4}B^4 + \frac{1}{4}\mu^2 B^2 - \frac{1}{32}\mu^4\Big)\Big\} \\
p_1 = \frac{1}{4}\sigma a\Big(B^2 + \frac{1}{2}\mu^2\Big) \\
p_2 = \frac{1}{8}\sigma a\mu^2 B \\
p_3 = \frac{1}{16}\sigma a\mu^3
\end{gathered} \tag{3.21}$$

where, $\sigma = \frac{bc}{\pi R}$ is called blade disc solidity and b accounts for number of blades. Equation (3.18) and Eq. (3.19) are substituted into Eq. (3.20) to get an expression of thrust coefficient C_t as a linear function of λ shown in Eq. (3.22).

$$\begin{aligned}
C_t &= (p_1 + p_2 s_0 + p_3 m_0)\lambda + (p_0 + p_2 s_1 + p_3 m_1) \\
&= c_0\lambda + c_1
\end{aligned} \tag{3.22}$$

Assuming Fourier coefficients are already known by solving Eq. (3.17), Eq. (3.22) represents a simplified version of Eq. (3.20) which can be considered only a function of variable λ. In [4],

The lift-coefficient of the system C_L depends on the angle of attack α_r of the blade and same as the airfoil dictated by the formula $C_L = a\alpha_r$. Depending on the blade position either in a forward or reversed flow region shown in Fig. 3.3(c)-(d), α_r changes. In the forward region, $\alpha_r = \theta + \phi$ and when the blade is in the reverse region, $\alpha_r = -\phi - \theta$. The relation of rotor lift coefficient C_{L_r} with thrust coefficient C_t is defined in [4] is given in Eq. (3.23).

$$C_{L_r} = \frac{2C_t \cos\beta^3}{\mu^2} \tag{3.23}$$

Equation. (3.23) can be used to analyze the lift force the system will get. A nonlinear equation relating the variables α, C_t and λ is given as depicted in Eq. (3.24).

$$\tan\alpha = \frac{\lambda}{\mu} + \frac{\frac{1}{2}C_t}{\mu(\lambda^2+\mu^2)^{\frac{1}{2}}} \tag{3.24}$$

This equation (3.24) can be reformulated as Eq. (3.25) where C_t is replaced with the expression derived in Eq. (3.22).

$$\tan\alpha = \frac{\lambda}{\mu} + \frac{\frac{1}{2}(c_0\lambda + c_1)}{\mu(\lambda^2+\mu^2)^{\frac{1}{2}}} \tag{3.25}$$

It is evident from Eq. (3.17) and Eq. (3.25) that they are coupled and so a simultaneous numerical approach is rquired to solve them. The following steps are followed to determine λ and a_0, a_1, b_1, a_2, b_2 from Eq. (3.17) and Eq. (3.25):

1. A good initial guess of λ is given to Eq. (3.17) to determine ρ_c which eventually provides c_0 and c_1 by solving Eqs. (3.18)-(3.22) sequentially.

2. λ is approximated using Eq. (3.25).
3. The error between calculated λ and guessed λ is evaluated to check convergence criteria.
4. If convergence criteria is not met, guess for λ is adjusted towards the calculated value of λ.
5. Steps 1-4 are repeated until desired convergence is achieved for λ. The threshold value for absolute change in λ is chosen to be 10^{-6}.
6. With the converged value of λ, Fourier coefficients are calculated finally using Eq. (3.17) at that instant.

Equations (3.12)-(3.25) are same for both the rotors. However, μ in these equations got replaced by μ_A and μ_B and Ω got replaced by Ω_1 and Ω_2. Thus the above numerical process is implemented for both rotors separately to evaluate λ_a, λ_b, ρ_{cA}, ρ_{cB}.

Wheatley in [4] suggested the average thrust force shown in Eq. (3.26) over one full rotation of the rotor to be broken down into the blade-retreating and blade-advancing flow regions.

$$\begin{aligned} T &= \frac{b}{2\pi}\int_0^{2\pi} d\psi \int_0^{BR} \frac{1}{2}\rho c U^2 C_L dr \\ &= \frac{b}{2\pi}\int_0^{\pi} d\psi \int_0^{BR} \frac{1}{2}\rho c a U^2 (\theta+\phi)\, dr + \\ &\frac{b}{2\pi}\int_\pi^{2\pi} \left[\int_0^{-\mu R\sin\psi} \frac{1}{2}\rho c a U^2 (-\theta-\phi)\, dr + \int_{-\mu R\sin\psi}^{BR} \frac{1}{2}\rho c a U^2 (\theta+\phi)\, dr\right] d\psi \end{aligned} \tag{3.26}$$

However, in this dynamic model, thrust coefficient, C_{t_1} and C_{t_2}, are calculated with Eq. (3.24) to calculate the thrust force in each rotor using Eq. (3.27).

$$\begin{aligned} T_1 &= \rho\Omega_1^2\pi R^4 C_{t_1} \\ T_2 &= \rho\Omega_2^2\pi R^4 C_{t_2} \end{aligned} \tag{3.27}$$

Equation. (3.28) gives the average aerodynamic torque Q about the rotor expression suggested by Wheatley in [4].

$$Q = \frac{b}{2\pi}\int_0^{2\pi} d\psi \int_0^{BR} \frac{1}{2}\rho c U^2 \phi C_L r dr - \frac{b}{2\pi}\int_0^{2\pi} d\psi \int_0^{R} \frac{1}{2}\rho c U^2 \delta r dr \tag{3.28}$$

where, δ is the average drag coefficient. Q is zero for steady-state autorotation. So, regenerative braking torque must be equal to the aerodynamic torque in steady-state case [9]. But for dynamic modeling, Q must be calculated separately with Eq. (3.29) reformulated from Eq. (3.28).

$$\begin{aligned}
Q = \frac{1}{2}b\rho c\Omega^2 R^4 a\Big\{&\lambda^2\Big(\frac{1}{2}B^2 - \frac{1}{4}\mu^2\Big) + \lambda\Big(\frac{1}{3}\theta_0 B^3 + \frac{2}{9\pi} \\
&\mu^3\theta_0 + \frac{1}{4}\theta_1 B^4 + \frac{1}{32}\mu^4\theta_1\Big) + \mu\lambda a_1\Big(\frac{1}{2}B^2 - \frac{3}{8}\mu^2\Big) \\
&+a_0^2\Big(\frac{1}{4}\mu^2 B^2 - \frac{1}{16}\mu^4\Big) - \frac{1}{3}\mu a_0 b_1 B^3 + a_1^2\Big(\frac{1}{8}B^4 \\
&+\frac{3}{16}\mu^2 B^2\Big) + b_1^2\Big(\frac{1}{8}B^4 + \frac{1}{16}\mu^2 B^2\Big) - a_2\Big(\frac{1}{4}\mu^2 a_0 B^2 \\
&+\frac{1}{6}\mu b_1 B^3\Big) + \frac{1}{2}a_2^2 B^4 + b_2\Big(\frac{1}{8}\mu^2\theta_0 B^2 + \frac{1}{12}\mu^2\theta_1 B^3 \\
&+\frac{1}{6}\mu a_1 B^3\Big) + \frac{1}{2}b_2^2 B^4 - \frac{\delta}{4a}\Big(1 + \mu^2 - \frac{1}{8}\mu^4\Big)\Big\}
\end{aligned} \tag{3.29}$$

Aerodynamic torque Q is calculated for each rotor using Eq.(3.29) with rotors' respective Fourier coefficients to get Q_1 and Q_2. The aerodynamic thrust force and torque evaluated in this dynamic model are an average expression of the thrust force and torque of the rotors. Once T_1, T_2, Q_1, Q_2 are evaluated from Eq.(3.27) and Eq.(3.29) respectively , Eqs. (3.1)-(3.5) are solved to get the attitude of the auotgyro system.

3.3 Inextensible Tether Model

The tether tension T_t provides the restoring effect on the multi-rotor autogyro system. T_t is evaluated by adopting the static catenary model from [60]. Figure. 3.4 shows the static forces acting on the two end points of the tether at any instant.

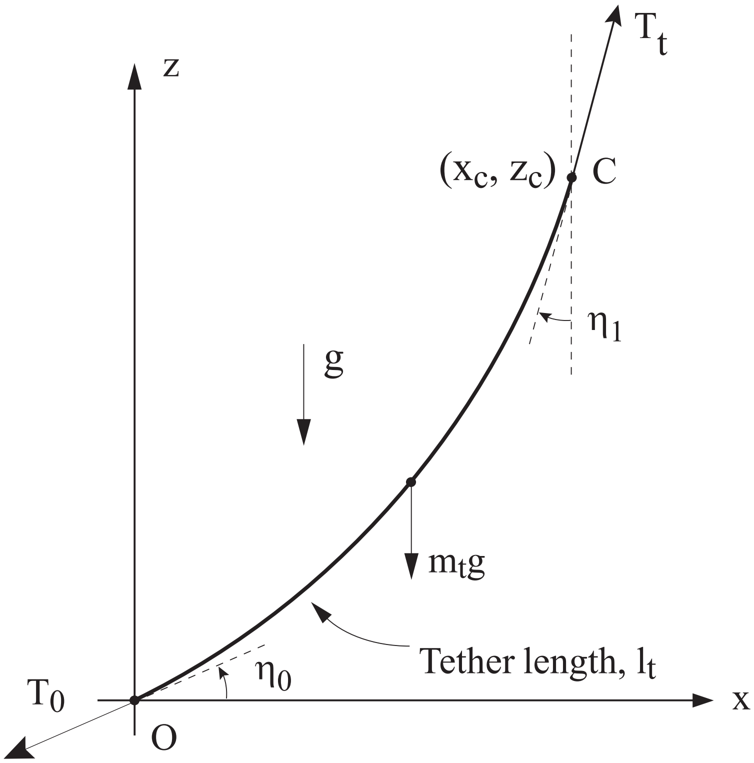

Figure 3.4: Static forces on the tether

The tether shape is defined by two hyperbolic equations shown in Eqs. (3.30)-(3.31).

$$\frac{z_c}{\zeta} = \left[\cosh\left(\frac{x_c - q}{\zeta}\right) - \cosh\left(\frac{q}{\zeta}\right)\right] \tag{3.30}$$

$$\frac{l_t}{\zeta} = \left[\sinh\left(\frac{x_c - q}{\zeta}\right) + \sinh\left(\frac{q}{\zeta}\right)\right] \tag{3.31}$$

where, l_t is the length of the tether, q and ζ are tether parameters which are functions of position and tether length. After taking the square of the equations (3.30) and (3.31) and then subtracting the squared equations yield Eq. (3.32).

$$\cosh\left(\frac{x_c}{\zeta}\right) = 1 + \frac{1}{2\,\zeta^2}\left(l_t^2 - z_c^2\right) \tag{3.32}$$

Equation (3.32) is numerically solved to determine ζ. Division of Eq.(3.30) by Eq.(3.30) leads to Eq.(3.33).

$$q = \frac{x_c}{2} - \left\{\zeta \tanh^{-1}\left(\frac{z_c}{l_t}\right)\right\} \tag{3.33}$$

With a known ζ from the prior numerical calculation, q can be easily calculated with Eq. (3.33) for a certain tether length l_t and known endpoint (x,z) of the tether which in this case is the center point C of the frame as shown in Fig. 3.4. Equations. (3.34)-(3.35) adopted from [60] are used to calculate tether angle at base,η_0 and angle η_1 that end point C of the tether makes with the vertical z-axis using the tether parameters ζ and q.

$$\eta_0 = \arctan\left\{-\sinh\left(\frac{q}{\zeta}\right)\right\} \tag{3.34}$$

$$\eta_1 = \frac{\pi}{2} - \arctan\left(\frac{l_t}{\zeta} + \tan\eta_0\right) \tag{3.35}$$

However, η_0 and η_1 possess two constraints that need to be maintained carefully while simulating the model for the system to be valid and they are- (i) summation of the tether angles should always be below 90° i.e $\eta_0 + \eta_1 < 90^\circ$ and (ii) The angle η_0 should remain above 0° which means $\eta_0 > 0^\circ$. After that, static force balance is done assuming a slender tether profile. This assumption helps ignore the drag force acting on the tether. Equations (3.36) and (3.37) show static force balance of the catenary system.

$$T_t \sin\eta_1 - T_0 \cos\eta_0 = 0 \tag{3.36}$$

$$T_t \cos\eta_1 - T_0 \sin\eta_0 - m_t g = 0 \tag{3.37}$$

where, m_t is the mass of the tether. An expression of T_0 from Eq. (3.36) is evaluated and substituted in Eq. (3.37) to determine T_t knowing η_0 and η_1 from Eqs. (3.34) and (3.35) respectively. This results in the expression for T_t shown in Eq. (3.38).

$$T_t = \frac{\sigma_t l_t g \cos\eta_0}{\cos(\eta_0 + \eta_1)}, \tag{3.38}$$

where, σ_t is the mass per unit length of the tether. As an inextensible tether is considered in this model, this restricts the tether from being taught during the simulation and contributes to the characterization of the equilibria of the tethered autogyro system.

CHAPTER 4: EXPLORING THE EQUILIBRIUM SPACE THROUGH SIMULATION

In this chapter, the equilibrium space of the tethered autogyro has been investigated and the ideal operating region has been identified via simulating the developed dynamic model of the system by solving the equations of motion presented in Eqs.(3.1)-(3.5) in Simulink. The parameter values used in the simulation are taken from [9] for small, light autogyro at low altitudes suitable for hovering without power generation where the masses of the autogyro and tether are adjusted for two rotors. Parameter values are given in Table 4.1:

Table 4.1: Parameters of Tethered Autogyro

Parameters	Values	Parameters	Values
a	5.85	m_a	$35.94\ kg$
b	4	M_W	$37.9625\ Nm$
B	0.96	R	$3.048\ m$
c	$0.24384\ m$	δ	0.012
d_c	$10\ Ns/m$	ρ	$1.225\ kgm^{-3}$
I	$7.884\ kgm^2$	θ_0	$0.0384\ rad$
I_c	$547.61\ kgm^2$	θ_1	$4.9448^{-03}\ rad/m$
I_r	$73.72\ kgm^2$	σ	0.1019
l	$8.13\ m$	σ_t	$0.0148\ kg/m$

The variables in Table 4.1 are defined in the nomenclature. While initial values of the states and parameter values are provided in the simulation, the solution of the equations of motion converges to equilibrium without any external control input. This yields an equilibrium space having a similar trend found in the steady-state model [9] corroborating the validity of the model. The stability of the equilibria is indicated by this convergence.

Figure 4.1 illustrates the equilibrium and tether profile of the system in a 10 m/s wind field with l_t

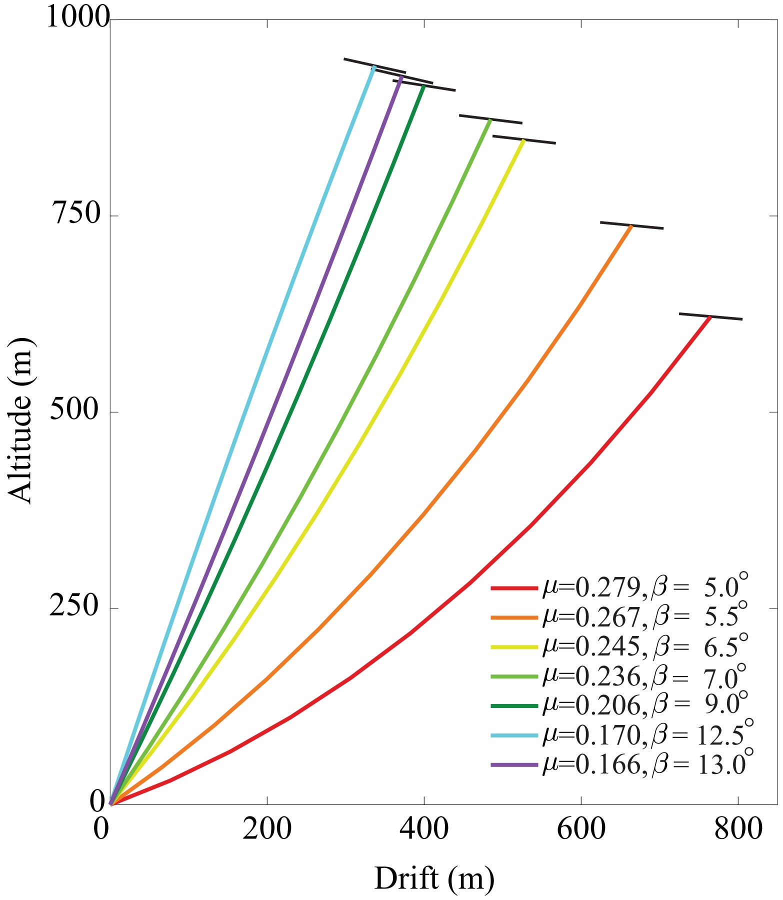

Figure 4.1: Tether profile for autogyro with l_t=1000 m in uniform 10 m/s wind field with corresponding μ and β

of 1000 m at different pitch angles and tip-speed ratio. For low pitch angle β and higher tip speed ratio μ the system is practically in the region where drift surpasses altitude marked by the red tether in Fig.4.1. In this region, the tether is slack and provides low tension. As β keeps increasing, the system gains altitude and the tether becomes taught. For this particular wind speed and l_t, the highest altitude is achieved at β=12.5°. When β exceeds 12.5° the altitude again decreases. This phenomenon is indicated in Fig. 4.1 where β=13°. The equilibrium space of the dynamic model differs from the one of the steady-state model in the sense that the dynamic model becomes

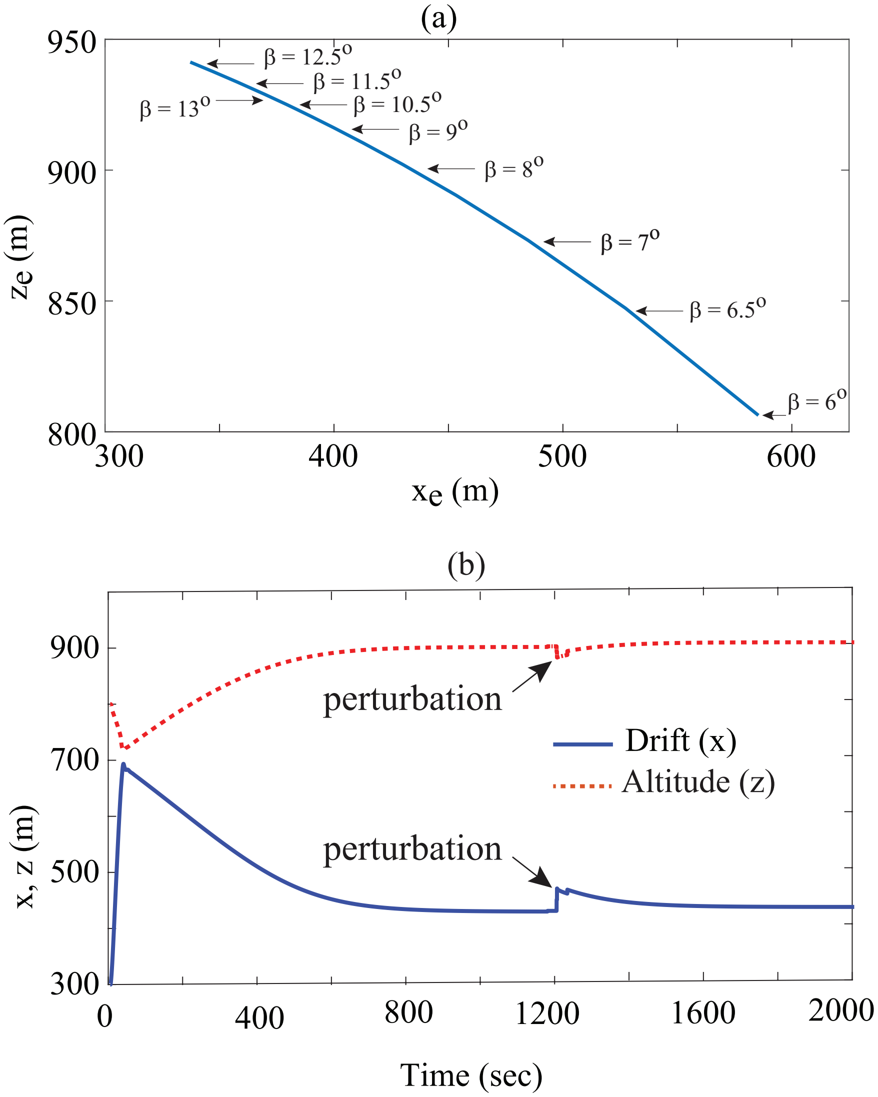

Figure 4.2: Equilibrium characteristics at V_w=10 m/s and l_t= 1000 m : (a) Equilibria at different β; (b) Transient behavior of the system under perturbation at equilibrium

unstable at a very high pitch angle and lower μ. Thereby, it cannot generate stable equilibrium points at β larger than 13° for this specific scenario. At pitch angle β greater than β=12.5°, the system enters drag driven region with a very taught tether and dynamic analysis has been done by avoiding this region.

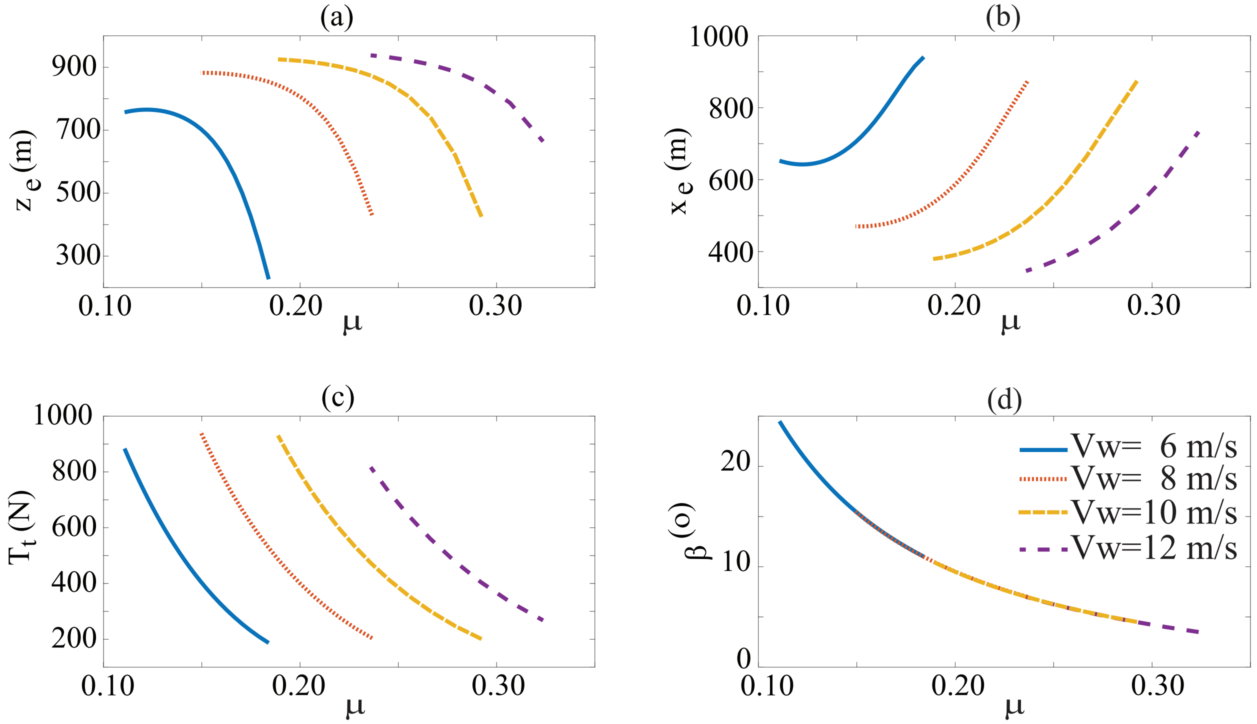

Figure 4.3: Equilibrium properties variation with μ for fixed l_t=1000 m in varying wind speeds: (a) Equilibrium altitude; (b) Equilibrium drift; (c) Tether tension at corresponding equilibria; (d) Equilibrium pitch angle

The optimal operating region associated with V_w= 10 m/s and l_t= 1000 m is plotted in Fig. 4.2(a). Figure 4.2(b) shows that without any external control, the system attains equilibrium in uniform wind speed, for a fixed tether length and a fixed pitch angle of the system. In Fig. 4.2(b), at t = 1200 s the system is perturbed from its equilibrium position, (x_e, z_e). The equilibrium position is restored subsequently indicating an internally stable equilibrium of the 2D autogyro system, especially for small perturbations. The stability analysis regarding this behavior is presented in Chapter 5.

The equilibrium characteristics with respect to tip-speed ratio μ are presented in Figs. 4.3 and 4.4. At equilibrium, the tip-speed ratios of both rotors converge to the same value, therefore μ values in Fig. 4.3 and 4.4 represent the tip-speed ratio of the overall system.

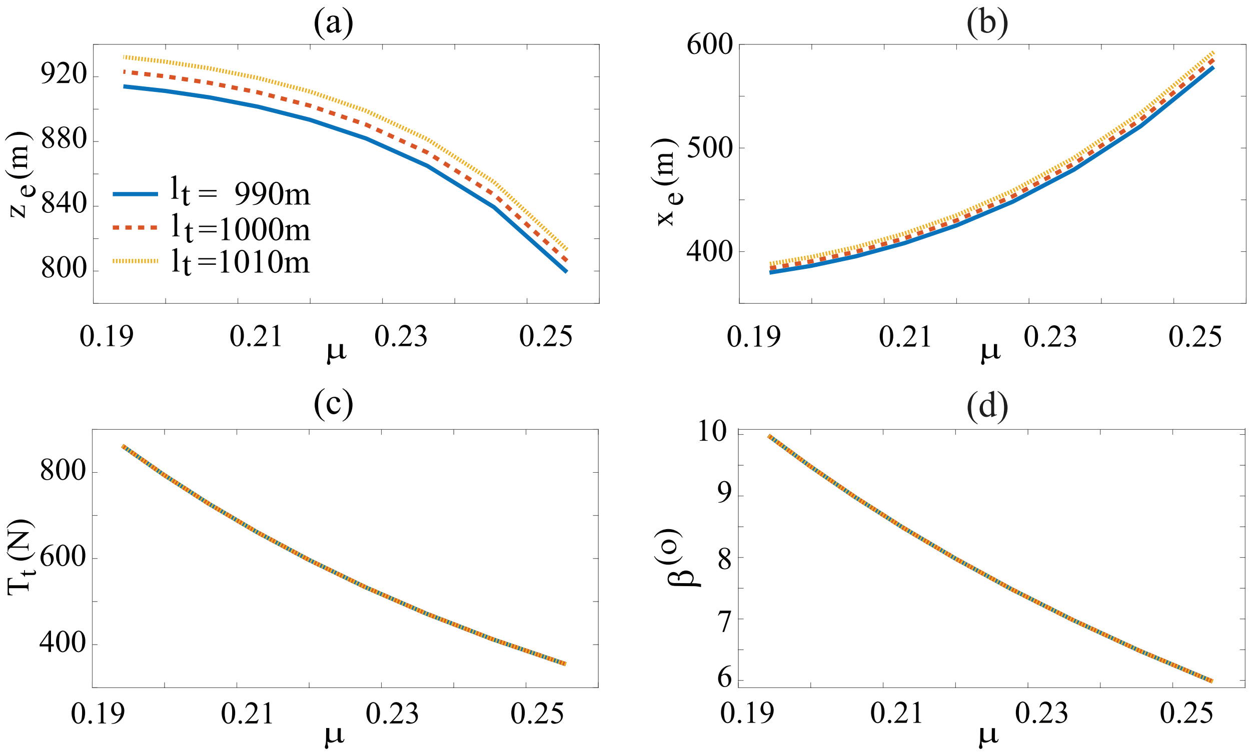

Figure 4.4: Equilibrium properties variation with μ in fixed V_w=10 m/s for varying l_t: (a) Equilibrium altitude; (b) Equilibrium drift; (c) Tether tension at corresponding equilibria; (d) Equilibrium pitch angle

Figure 4.3(a)-(b) illustrates the variation of altitude and drift with μ for different wind speeds. Optimal μ is defined where the lift achieved by the autogyro is higher and horizontal drift is lower with a reasonable tether tension. For lower V_w like 6 m/s optimal μ is between 0.11-0.15. μ greater than 0.15 indicates that the system is in the low-lift region where tether tension is significantly low. The optimal μ range shifts to higher values as V_w increases. For V_w= 8 m/s, 10 m/s and 12 m/s, optimal μ's are approximately between 0.15-0.21, 0.17-0.26 and 0.24-0.30 respectively. However, the maximum altitude gain is restricted by tether tension as depicted in Fig. 4.3(c). It also shows that at a fixed μ, tether tension increases with increasing wind speed. Figure 4.3(d) shows that the system's pitch angle β has an inverse relationship with μ. Though the range of optimum μ is different for different V_w, the overlapping plots in Fig. 4.3(d) exhibit that for any particular μ, there is a fixed β indifferent to wind speed. From Fig. 4.4, it can be seen that the optimum μ range

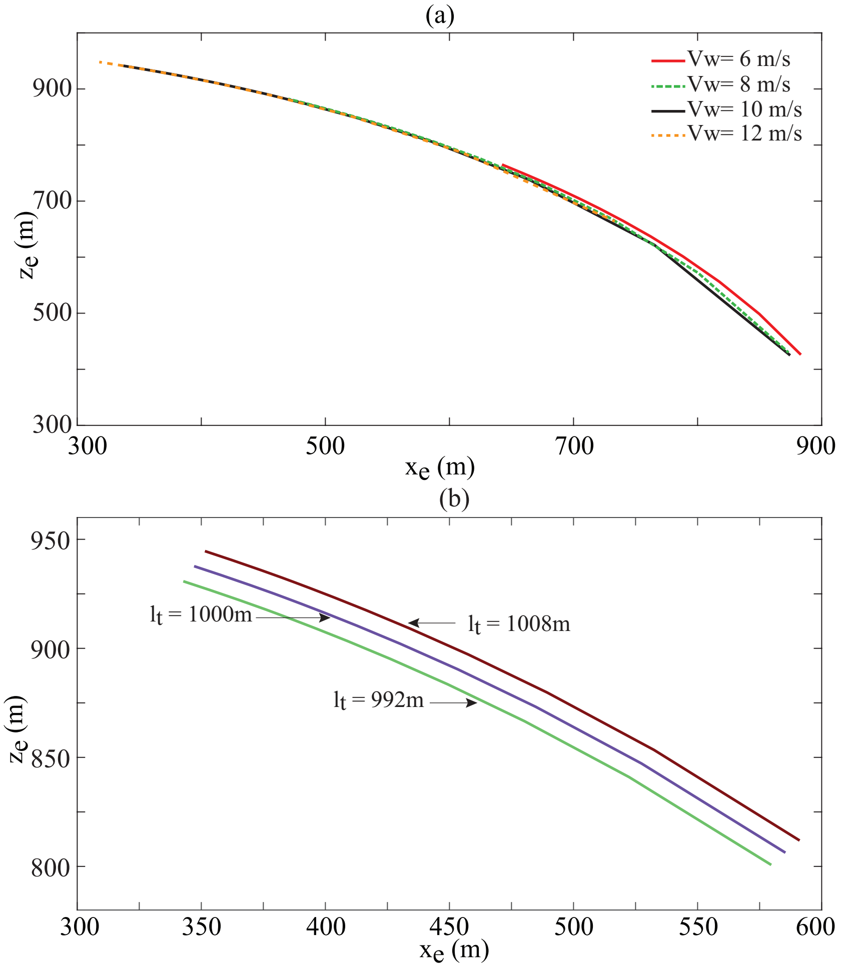

Figure 4.5: Characteristics of equilibria: (a) Equilibria for varying V_w for fixed l_t=1000 m; (b) Equilibria for varying l_t at V_w=10 m/s for $\beta = 6° - 12°$

does not change with a change in tether length l_t for fixed V_w. A higher altitude can be achieved with the same μ if l_t is increased and this also causes drifts to slightly increase as can be seen from Fig. 4.4(a)-(b). Figure 4.4(c) demonstrates the indifference of tether tension to the change in tether length. Therefore, if the system requires a higher altitude, the l_t can be increased without worrying much about tether tension. Finally, Fig. 4.4(d) shows the one-to-one relationship of μ with β that has been already found in 4.3(d).

Another analysis is conducted for equilibrium space to demonstrate the variation of equilibria with varying wind speed V_w in Fig.4.5(a) and also with varying tether length l_t in Fig.4.5(b). Referring to Fig.4.5(a), it is apparent that the dependency of equilibrium points on V_w at a fixed $l_t = 1000$ m is not much but the operating range of pitch angle β is narrower at lower V_w, which gets wider with increasing V_w. On the contrary, equilibrium points depend on l_t as Fig.4.5(b) suggests that the system can achieve higher altitudes by increasing the tether length and can lower the elevation by decreasing the tether length from the same horizontal position. It also suggests that the autogyro can achieve a fixed altitude at different horizontal positions by changing tether length. This behavior indicates the system's ability to hover at the same altitude.

CHAPTER 5: CONTROLLER FOR ALTITUDE TRACKING AND CORRESPONDING STABILITY INVESTIGATION

5.1 Control Algorithm

The unpowered autorotating rotors of the autogyro generate the required thrust forces to lift the rotorcraft using ambient wind energy. The braking of the individual autorotating rotors can be utilized for altering the pitch of the system which will lead to tracking of a desired altitude. It is apparent from Eqs.(3.4) and (3.5) that braking torques q_1 and q_2 which are negative, will reduce the corresponding angular velocities Ω_1 and Ω_2. Equations (3.27) and (3.3) show that braking of the rotors will make the thrust forces T_1 and T_2 to differ and thereby modify systems pitch angle β. Figure 4.2(a) shows that the change in β, produced by the braking torque, will lead to altitude change.

To achieve this objective a proportional feedback control algorithm is designed at first in this study to enable the autogyro to reach a desired altitude, z_d in the presence of both uniform and variable wind fields shown in Fig. 5.1.

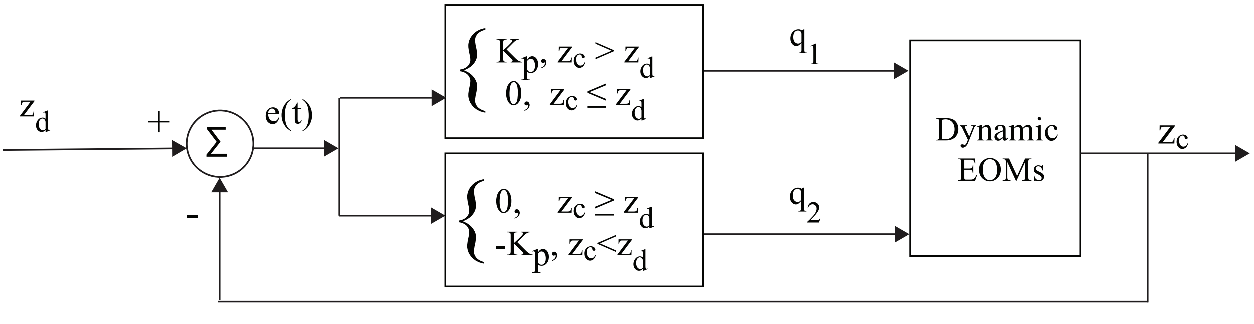

Figure 5.1: Block diagram of designed proportional (P) controller

The preliminary stability analysis in Section 5.2, shows that the proportional control leads to an integral effect in the dynamics of $(z_c - z_d)$. This allows the error $e(t) = (z_d - z_c)$ to go to zero. The algorithm opts for one control input which is either braking torque q_1 or q_2 applied on the respective rotor A or B at a time depending on the sign of the error. The control law is shown in Eq. (5.1):

$$
\begin{aligned}
q_1 &= \begin{cases} K_p(z_d - z_c) & \text{for} \quad z_c > z_d \\ 0 & \text{for} \quad z_c \le z_d \end{cases} \\
q_2 &= \begin{cases} 0 & \text{for} \quad z_c \ge z_d \\ -K_p(z_d - z_c) & \text{for} \quad z_c < z_d \end{cases}
\end{aligned}
\tag{5.1}
$$

where, K_p is the proportional gain and z_d is the desired altitude.

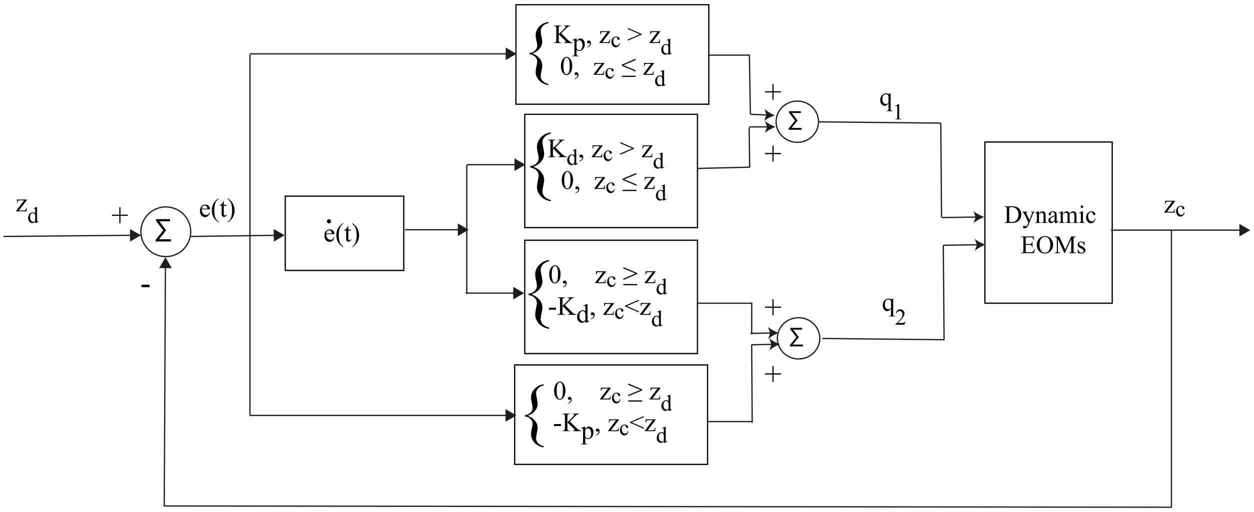

Figure 5.2: Block diagram of designed PD controller

The braking torque q_1 brakes rotor A, momentarily decreasing the thrust force T_1 and leading to a decrease in β. Eventually, altitude is decreased. In the same way, The braking torque q_2 in rotor B works in a similar manner except it increases β and thereby altitude is increased. The control input, q_1, q_2 is allowed to take a value between 0 and an upper limit depending on the error signal and wind speed V_w. This is done to avoid a drastic change in β which may cause problems by inducing instabilities in the system while small braking torques are sufficient to cause gradual changes in β.

Although the designed proportional (P) controller is effective in controlling higher altitude which is the best scenario for the maximum use of tether length, simulation results from Chapter 6 show that it is not so effective where tether tension is low associated with the maximum value of optimum μ range and also when wind speed reduces by a significant amount. This brings on the need to design a proportional-derivative (PD) feedback controller. The algorithm of the PD controller is demonstrated in Fig. 5.2. The following Equation (5.2) shows the control algorithm employed to control altitude at high μ:

$$\begin{aligned} q_1 &= \begin{cases} K_p(z_d - z_c) + K_d \dfrac{\mathrm{d}(z_d - z_c)}{\mathrm{d}t} & \text{for} \quad z_c > z_d \\ 0 & \text{for} \quad z_c \leq z_d \end{cases} \\ q_2 &= \begin{cases} 0 & \text{for} \quad z_c \geq z_d \\ -K_p(z_d - z_c) - K_d \dfrac{\mathrm{d}(z_d - z_c)}{\mathrm{d}t} & \text{for} \quad z_c < z_d \end{cases} \end{aligned} \tag{5.2}$$

where, K_d is the derivative gain. In Chapter 6, both the controller performances shown in Eqs. (5.1) and (5.2).

5.2 Preliminary Stability Analysis

In this section, an approximate closed-loop dynamics is developed to explain the effectiveness of the control law of Eqs. (5.1) and (5.2) in altitude control. Considering the dynamics of the variable $\tilde{z} = (z_c - z_d)$ and referring to Eq. (3.2) following equation can be written:

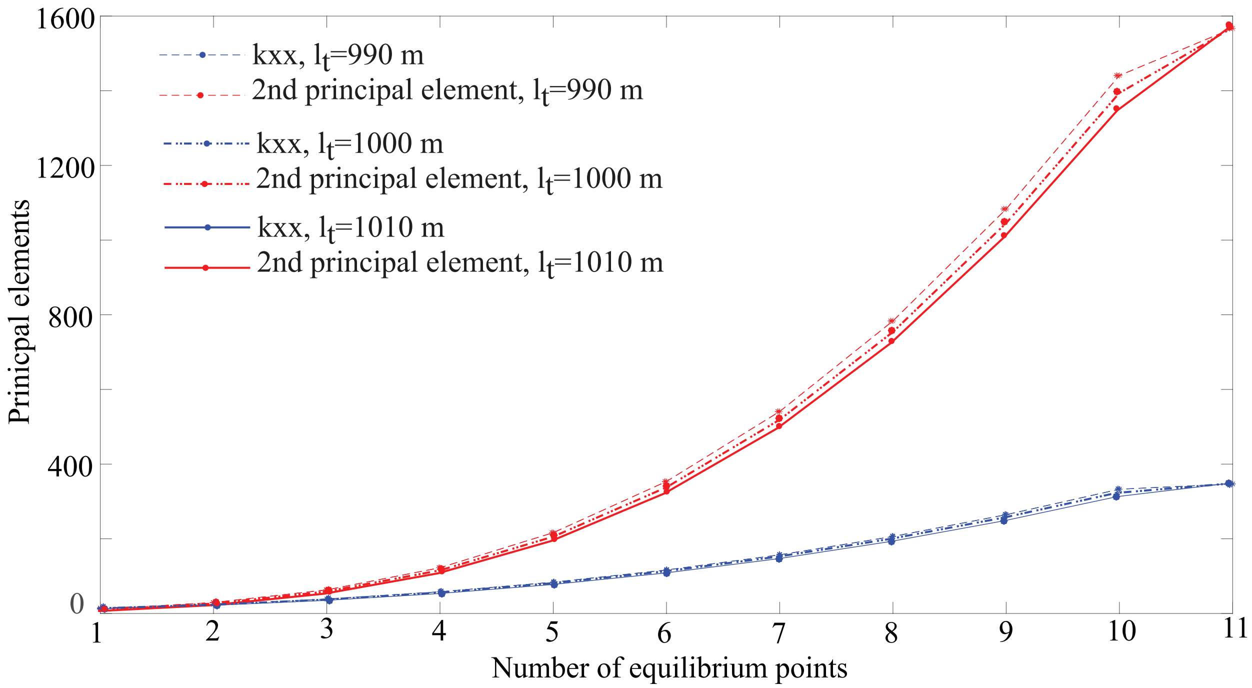

Figure 5.3: Principal elements of K matrix

$$\begin{aligned}(T_1+T_2)\cos\beta &= (T_1-T_2)\cos\beta + 2T_2\cos\beta \\ &= 2\frac{I_c}{l}\ddot{\beta} + 2T_2\cos\beta\end{aligned} \tag{5.3}$$

Simulation results from Chapter 6 suggests that β has slow dynamics which can be approximated by,

$$\dot{\beta} = k_1(q_1 - q_2), \tag{5.4}$$

Referring to Eq. (5.1), the difference in control input can be written as follows,

$$(q_1 - q_2) = K_p(z_d - z_c) = -K_p\tilde{z}. \tag{5.5}$$

Therefore, for small perturbations around an equilibrium $z = z_d$, Eq. (5.3) can be expanded with

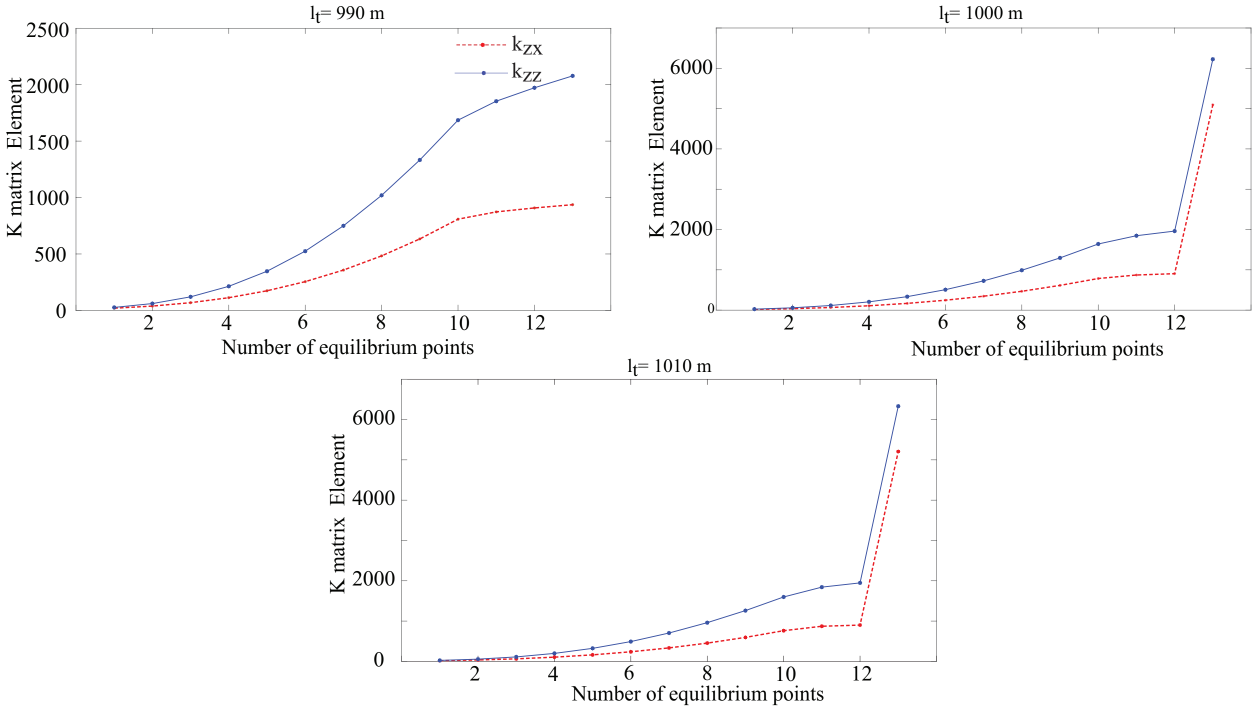

Figure 5.4: Elements of K matrix

Taylor series as following:

$$(T_1+T_2)\cos\beta = (2T_2\cos\beta)|_{eq} - 2\frac{I_c}{l}k_1K_p\dot{\tilde{z}} - \left[\frac{d}{d\beta}(2T_2\cos\beta)\right]_{eq} k_1K_p\int_0^t \tilde{z}dt \tag{5.6}$$

The time integral appears in Eq. (5.6) because from Eqs. (5.4) and (5.10), $d\beta = -k_1K_p\int_0^t \tilde{z}dt$. The catenary tension force described in Section 3.3 shows that it is only a position-dependent force and not velocity-dependent. So, from Eq. (3.2), the tether tension force can be expressed about the equilibrium as,

$$T\cos\eta_1 = (T\cos\eta_1)|_{eq} - k_{zz}\tilde{z} - k_{zx}\tilde{x} \tag{5.7}$$

where, $\tilde{x}$ is the small deviation of the horizontal x-coordinate of the autogyro from its equilibrium,

k_{zz} and k_{zx} are elements of the positive definite K matrix, where K is the 2x2 stiffness matrix shown in Eq.(5.8). Positive definiteness of the K matrix is proved by the simulations and is shown in Fig.5.3 for different tether lengths where the first principal element, (k_{xx}), and the second principal element of K matrix have positive values.

$$\begin{bmatrix} k_{xx} & k_{xz} \\ k_{zx} & k_{zz} \end{bmatrix} = \begin{bmatrix} \frac{\partial(T\sin\eta_1)}{\partial x} & \frac{\partial(T\sin\eta_1)}{\partial z} \\ \frac{\partial(T\cos\eta_1)}{\partial x} & \frac{\partial(T\cos\eta_1)}{\partial z} \end{bmatrix} \tag{5.8}$$

Figure 5.4 also shows that k_{zz} and k_{zx} are also positive. Together, an approximate dynamic equation of the system in the $\tilde{z}$ coordinate can be written as follows:

$$m_a\ddot{\tilde{z}} = -\left(d_c + 2\frac{I_c}{l}k_1K_p\right)\dot{\tilde{z}} - k_{zz}\tilde{z} - k_{zx}\tilde{x} - \left[\frac{d}{d\beta}\left(2T_2\cos\beta\right)\right]_{eq} k_1K_p\int_0^t \tilde{z}dt \tag{5.9}$$

Though the dynamic equation derived above is incomplete as other terms such as the aerodynamic drag forces must be included and Eq. (5.9) must be considered together with the corresponding dynamic equation of $\tilde{x}$, the structure of stability equation can be anticipated. The damping and restoring forces and their sources are also shown in Equation (5.9). Effective integral action provided by the controller may yield the robust convergence to z_d found in the simulation results. The ongoing stability analysis will investigate the stability characteristics of the equilibrium under the closed-loop control of Eq. (5.1).

Now, to find out PD controller closed-loop dynamics, the same procedure can be employed. Referring to Eq. (5.2), it can be written as:

$$(q_1 - q_2) = K_p(z_d - z_c) + K_d\frac{\mathrm{d}(z_d - z_c)}{\mathrm{d}t} = -K_p\tilde{z} - K_d\dot{\tilde{z}}. \tag{5.10}$$

Equation (5.10) will alter Eq.(5.6) into following:

$$\begin{aligned}
(T_1+T_2)\cos\beta &= (2T_2\cos\beta)\,|_{eq} - 2\frac{I_c}{l}k_1(K_p\dot{\tilde{z}}+K_d\ddot{\tilde{z}}) - \\
&\left[\frac{d}{d\beta}\left(2T_2\cos\beta\right)\right]_{eq} k_1\left(K_p\int_0^t \tilde{z}dt + K_d\int_0^t \dot{\tilde{z}}dt\right) \\
&= (2T_2\cos\beta)\,|_{eq} - 2\frac{I_c}{l}k_1(K_p\dot{\tilde{z}}+K_d\ddot{\tilde{z}}) - \\
&\left[\frac{d}{d\beta}\left(2T_2\cos\beta\right)\right]_{eq} k_1\left(K_p\int_0^t \tilde{z}dt + K_d\tilde{z}\right)
\end{aligned} \tag{5.11}$$

Combining Eqs.(5.7) and (5.11), an approximate dynamic equation of the system in the $\tilde{z}$ coordinate results in:

$$\begin{aligned}
(m_a + 2\frac{I_c}{l}k_1K_d)\ddot{\tilde{z}} = -\left(d_c + 2\frac{I_c}{l}k_1K_p\right)\dot{\tilde{z}} - (k_{zz} + \left[\frac{d}{d\beta}\left(2T_2\cos\beta\right)\right]_{eq} k_1K_d)\tilde{z} \\
- k_{zx}\tilde{x} - \left[\frac{d}{d\beta}\left(2T_2\cos\beta\right)\right]_{eq} k_1K_p\int_0^t \tilde{z}dt
\end{aligned} \tag{5.12}$$

Equation (5.12) shows that besides adding integral effect due to $K_p\int_0^t, \tilde{z}dt$, a positive term gets added to k_{zz} as $d\beta > 0$ when $\tilde{z} < 0$ which activates $K_d > 0$ and $d\beta < 0$ when $\tilde{z} > 0$, activating $K_d < 0$ therefore adds more positiveness to K matrices. Therefore, it provides more robustness in controlling the pitch and the altitude of the system than the proportional controller even at lower wind speed and at lower tension force provided by tether.

CHAPTER 6: SIMULATION RESULTS

6.1 Controller Performance in Uniform Wind Field

The designed proportional controller in Chapter 5 is implemented with $K_p = 0.01$ through simulation in the presence of a uniform wind speed of 10m/s and fixed tether length of 1000m, and results are presented in Figures 6.1- 6.4. The braking torque q_1 and q_2 are allowed to take a small value between a selected range to demonstrate the viability of the controller. This range is not fixed and changes depending on the wind speed and controller type. A list of controller gains with the selected limit is given in the following Table 6.1:

Table 6.1: Prescribed Controller Parameters

Controller Type	V_w (m/s)	$\lvert K_p \rvert$	$\lvert K_d \rvert$	Allowable Range (N-m)
P	10	0.01	$--$	$[-0.015, 0]$
P	9	0.01	$--$	$[-0.02, 0]$
P	8	0.01	$--$	$[-0.04, 0]$
P	7	0.01	$--$	$[-0.065, 0]$
PD	10	0.01	1	$[-0.015, 0]$
PD	9	0.01	1	$[-0.03, 0]$
PD	8	0.01	1	$[-0.045, 0]$
PD	7	0.01	1	$[-0.075, 0]$
PD	6	0.01	1	$[-0.1, 0]$

It can be seen from Fig. 6.1(a) that the autogyro effectively tracks the desired altitudes of 870m and 920 m without any steady-state error within the operating region. This zero steady-state error can be attributed to the integral action provided by the proposed P controller explained in Chapter 5. From Fig. 6.1(b)-(c), it is evident that the system's pitch angle β also increases gradually when barking torque q_2 is applied, thereby increasing altitude. The applied braking torques, q_1 and q_2 in each rotor are allowed to take a value between 0 and -0.015N-m. The upper limit is set to

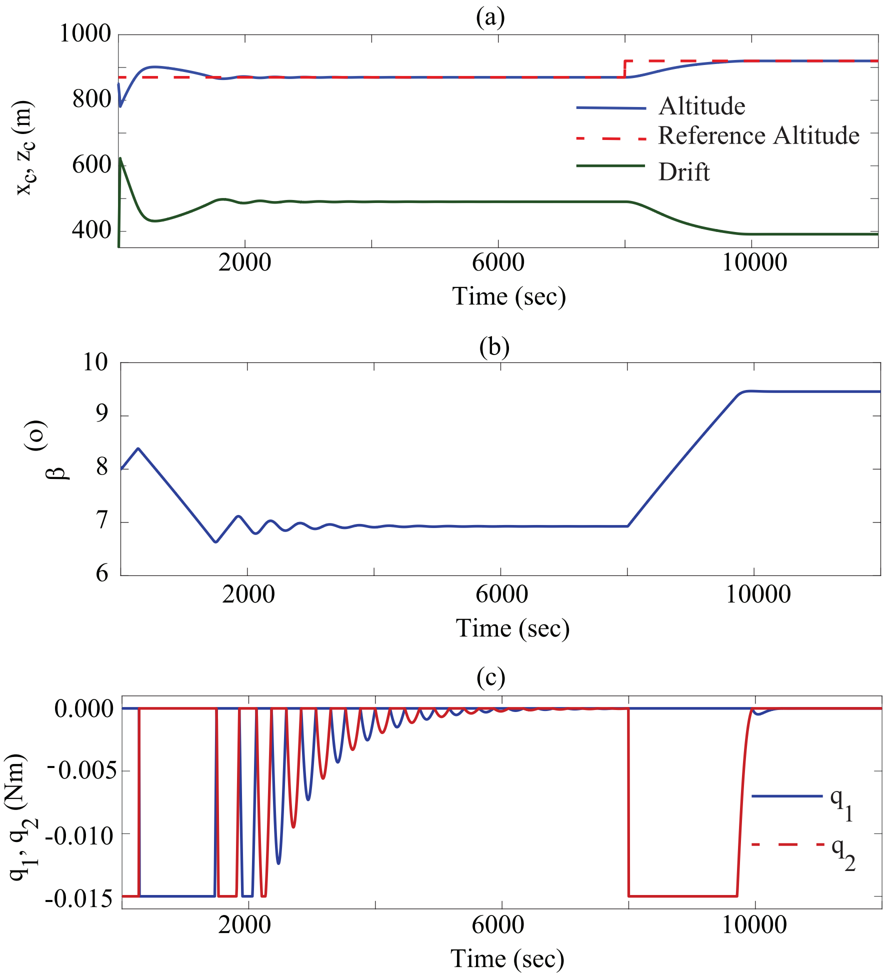

Figure 6.1: Altitude control in uniform wind speed of V_w =10 m/s with Proportional (P) controller: (a) Change in altitude and drift, reference altitude set at 870m and 920m; (c) Pitching angle of the system; (b) Applied braking torques as control input;

0 to ensure braking and the lower limit is set to a small value leading to a slow control action but it avoids abrupt change in pitch. Figure 6.1(c) confirms that the braking torques are mutually exclusive as evident from Eq. (5.1).

The corresponding tether tension, thrust forces, aerodynamic torques and resulting rotor speeds are shown in Fig. 6.2. The tether tension T_t is higher than the thrust forces T_1, T_2. Though T_1 and T_2

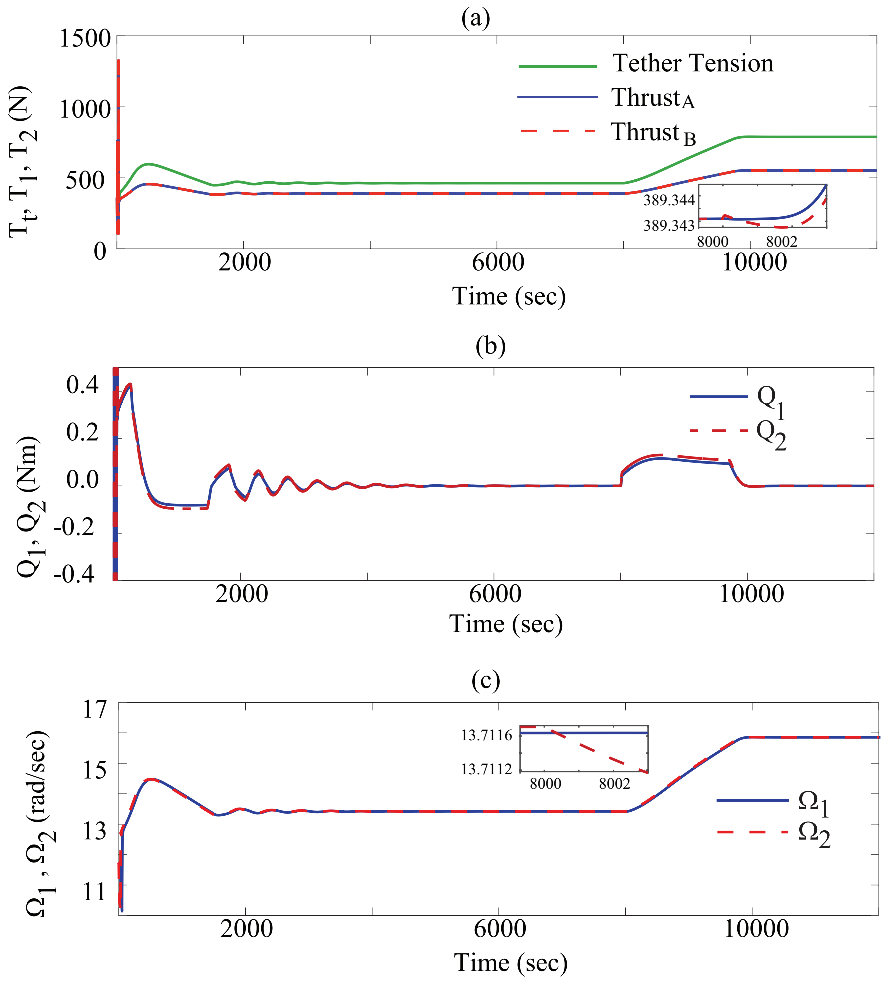

Figure 6.2: Effect of Proportional (P) controller on: (a) Tether tension T_t and thrust forces T_1,T_2; (b) Aerodynamic torques Q_1 and Q_1; (c) Rotational speeds Ω_1, Ω_2;

plots seem to overlap each other, the zoomed view in Fig. 6.2(a) shows that they differ by a very small amount during the transition period which however, is enough to alter β. The aerodynamic torques Q_1, Q_2 are not zero during transitions and reach zero when the error in altitude goes to zero, as can be seen in Fig. 6.2(b). The rotor speeds also increase with the application of q_2 and differ slightly during the transition as a consequence of braking, shown in Fig. 6.2(c).

Figure 6.3(a) suggests that rotors' tip-peed ratios increase with the application of q_1 when altitude

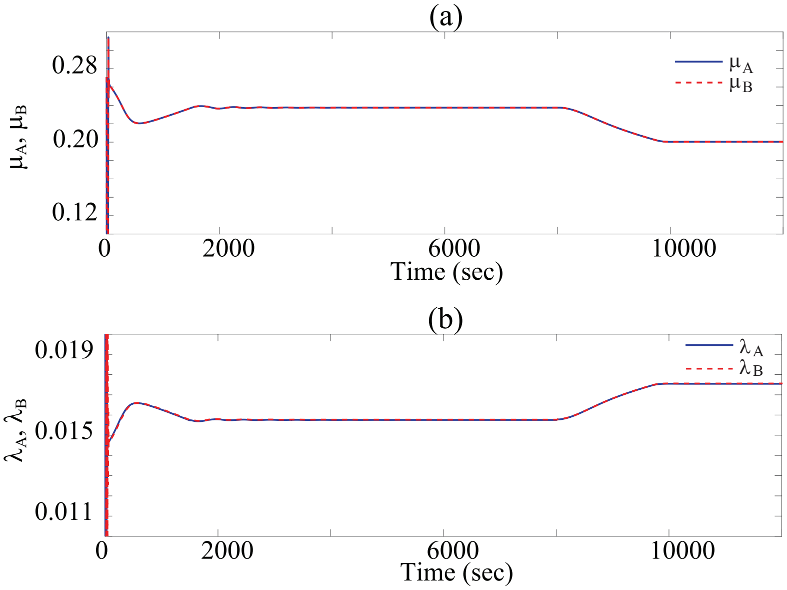

Figure 6.3: Effect of Proportional (P) controller on: (a) Tip-speed ratios μ_A and μ_B; (b) Inflow ratios λ_A and λ_B

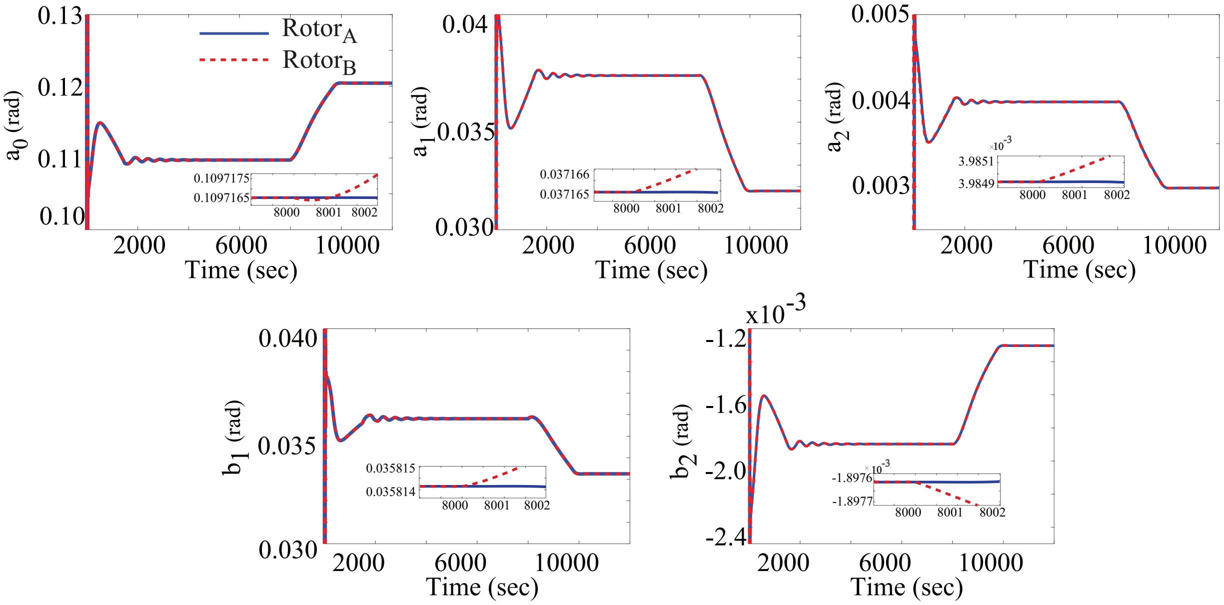

Figure 6.4: Effect of Proportional (P) controller on the Fourier coefficients

needs to be decreased and decrease with the application of q_2 to increase altitude. This corroborates the inverse relationship between μ and β demonstrated in Figs. 4.3(d) and 4.4(d). The increase in the inflow ratio, λ, of both rotors when q_2 is applied, shown in Fig. 6.3(b), proves that an increase in pitch angle β has more influence on the inflow ratio than the increase in rotor speeds.

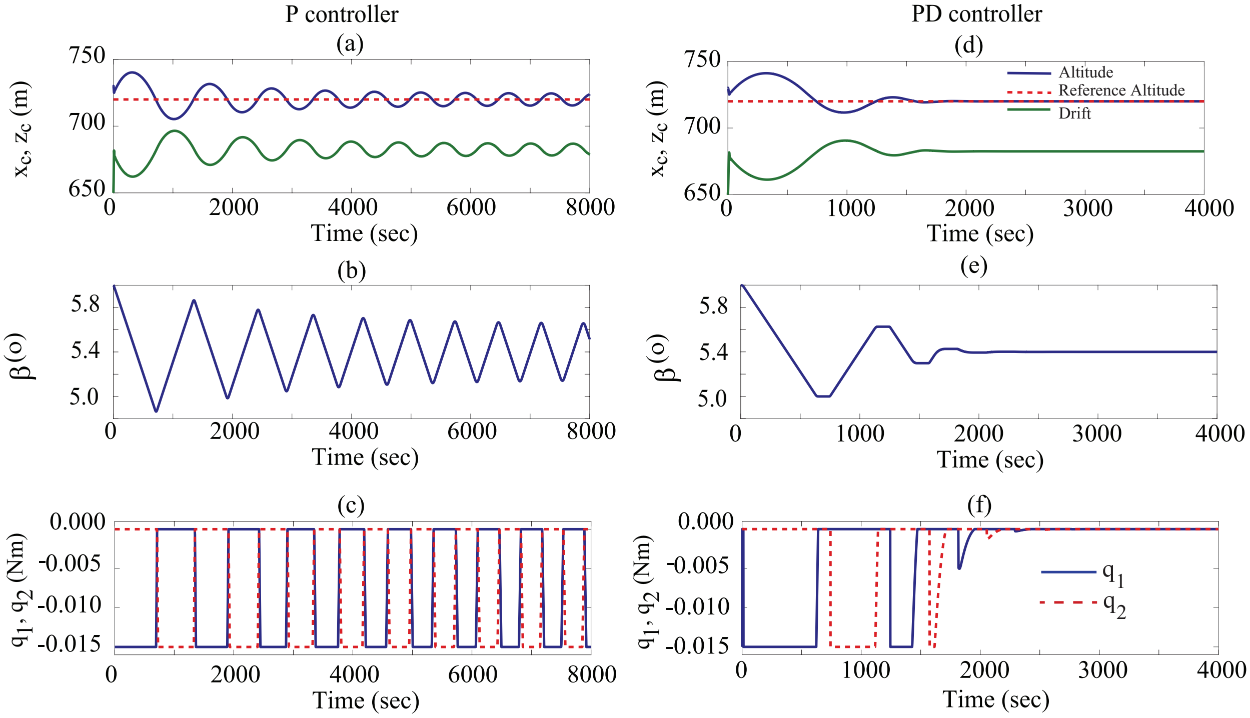

Figure 6.5: Proportional (P) and PD controller performance at z_d=720 m in 10 m/s V_w: (a), (d) Altitude and drift, reference altitude set at 720 m; (b),(e) System's pitch angle β; (c),(f) Applied braking torques as control input

In Figure 6.4, the influence of proportional control action is shown on the Fourier coefficients which approximate the blade flapping. It can be seen that a_0, b_2 increase with the application of q_2 following a similar trend as the system's pitch angle β while a_1, a_2, b_1 decrease with q_2. The zoomed views in Fig. 6.4 suggest that the coefficients of the two rotors also differ during the transition in altitude due to the applied control and converge to the same value when reference altitude is reached, indicating steady flapping.

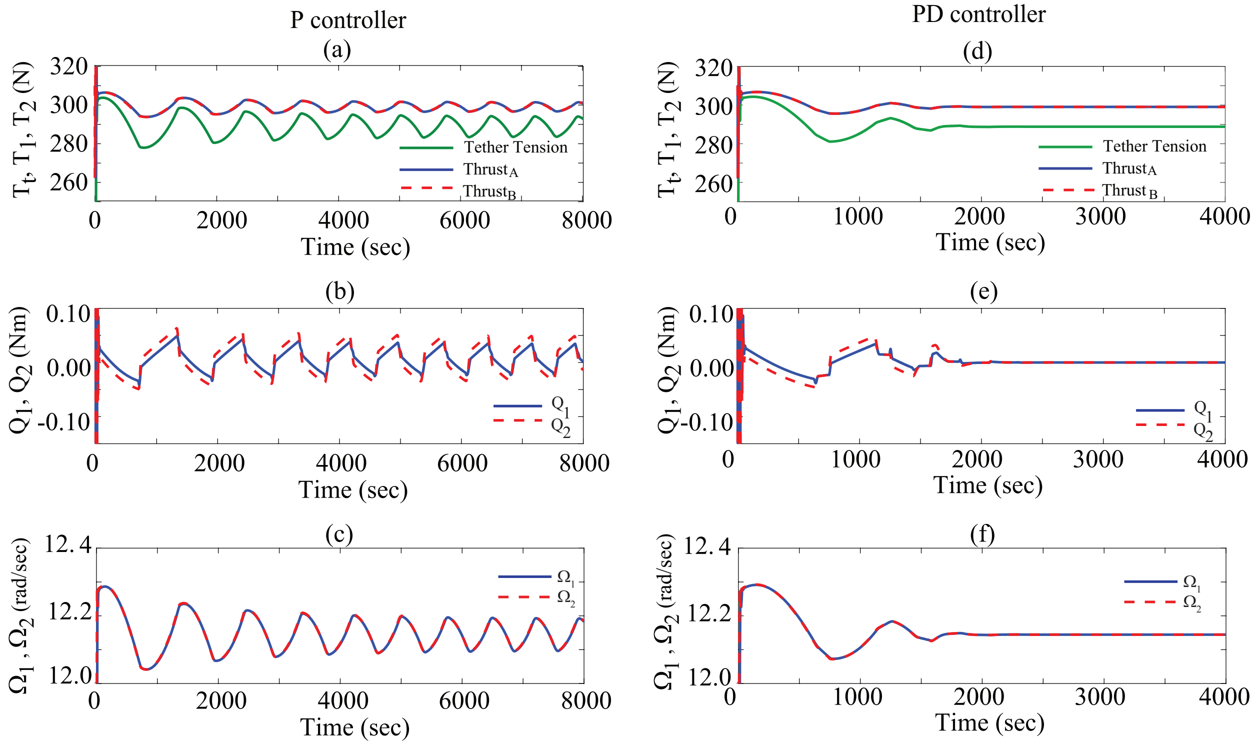

Figure 6.6: Proportional (P) and PD controller performance at z_d=720 m in 10 m/s V_w: (a), (d) Tether tension and thrust forces; (b),(e) Aerodynamic torques Q_A, Q_B; (c),(f) Rotational speeds Ω_1, Ω_2

After the responses of the states and forces with applied proportional control are presented in detail, the study proceeds to evaluate the proportional controller performance in the region where the tip-speed ratio μ is close to maximum value of operating μ range in a uniform wind speed, V_w of 10 m/s and at a fixed tether length of 1000 m. It is evident from Fig. 6.5(a)-(c) that with the same allowable limit of braking torques used for controlling higher altitudes, the autogyro fails to reach the desired altitude when it is set at 72% of tether length, l_t. Instead, the altitude oscillates about the desired altitude. The pitch angle β also shows sustained oscillations and braking torque keeps switching between q_1 and q_2 suggested by Figs.6.5(b) and (c). The oscillatory response of the system is demonstrated in Figs. 6.6(a)-(c). Figure 6.6(a) shows the lack of sufficient tension

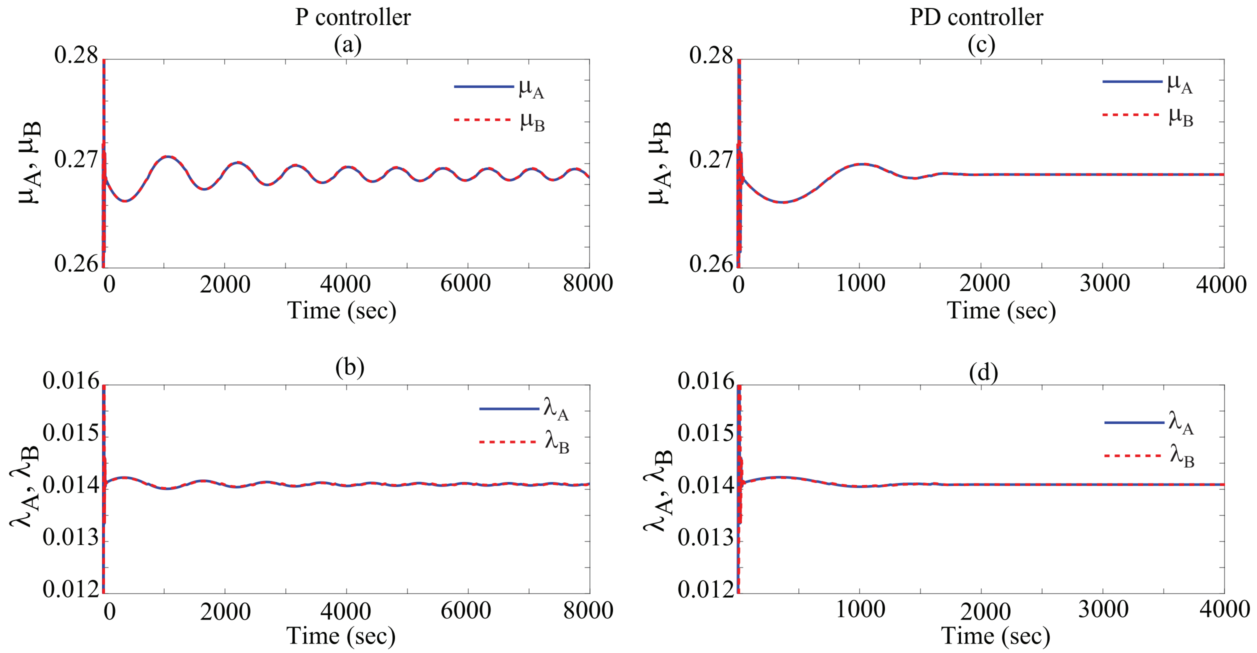

Figure 6.7: Proportional (P) and PD controllers' effect at z_d=720 m in 10 m/s V_w: (a),(c) Tip-speed ratio; (b),(d) Inflow ratio

force provided by the tether in the high μ region which can be attributed to the slack tether in this region. The tip-speed ratio μ and the inflow ratio λ also oscillate, shown in Fig. 6.7(a)-(b).

However, the proposed PD controller in Eq.(5.2), proves to be effective in controlling altitude near maximum μ region with the same limit of q_1, q_2 shown in Fig. 6.5(d)-(f). Here, the magnitude of K_d is set to be 1. From Fig.6.6, it can be seen that PD also stabilizes the system's pitch angle β. The response of the system has been stabilized with the PD controller in case of low restoring force from tether as can be seen from Fig.6.6 (d), (e), (f). The aerodynamic torques of rotors A and B differ during transients before converging to the zero at steady state, shown in Fig.6.6(e). In Fig. 6.7(c)-(d), it can be seen that the corresponding tip-speed ratios and inflow ratios also converge to a steady value due to the action of the PD controller when the desired altitude is reached.

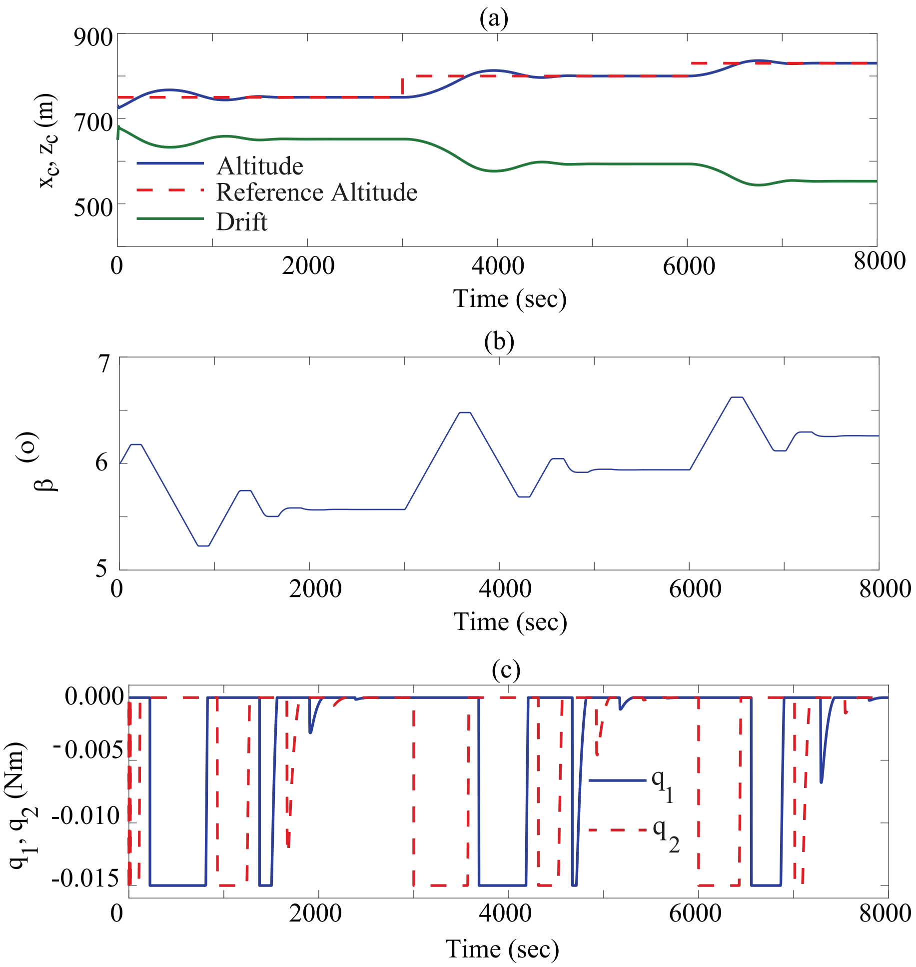

Figure 6.8: Altitude control in uniform wind speed of V_w =10 m/s with PD controller: (a) Change in altitude and drift, reference altitude set at 720 m, 770 m and 800 m; (b) Pitching angle of the system; (c) Applied braking torques as control input;

Next, a thorough analysis of the performance of the PD controller is presented through the simulation results near the region where the tether is slack. Figures 6.8, 6.9 and 6.10 show a similar trend of the responses when PD controller is applied as they are found in the proportional controller case. The PD controller not only enables the system to track the altitude within the whole operating region, but it also makes the simulation faster as exhibited in Fig. 6.8(a).

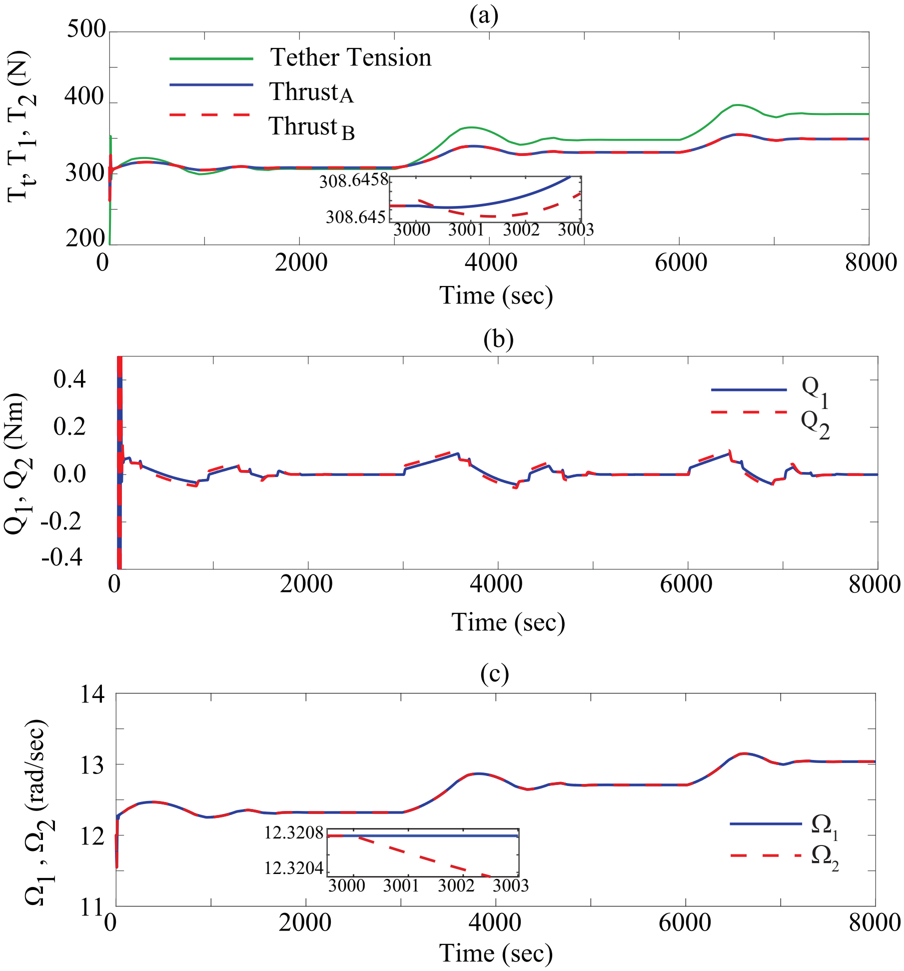

Figure 6.9: Effect of PD controller on: (a) Tether tension T_t and thrust forces T_1,T_2; (b) Aerodynamic torques Q_1 and Q_1; (c) Rotational speeds Ω_1 and Ω_2;

Figure 6.9(a) shows that at higher μ, tether tension force and thrust forces have approximately the same value. The ineffectiveness of the P controller can be attributed to not having enough tether tension at the region associated with high μ, indicating a slack tether. The aerodynamic torques Q_1 and Q_2, shown in Figure 6.9(b), vary when the controller is applied and finally, they converge to 0. The corresponding change in rotor speeds are presented in Figure 6.9(c). It can be seen from Fig. 6.10 that changes in the ratios are not so significant due to control action near low altitudes.

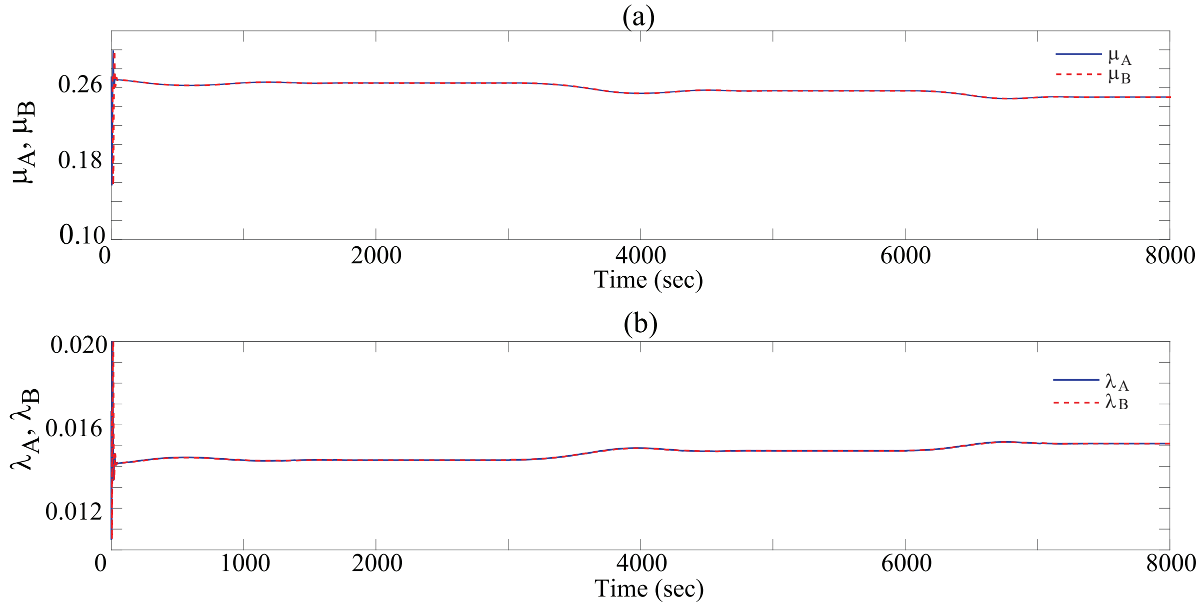

Figure 6.10: Effect of PD controller on: (a) Tip-speed ratios μ_A and μ_B; (b) Inflow ratios λ_A and λ_B;

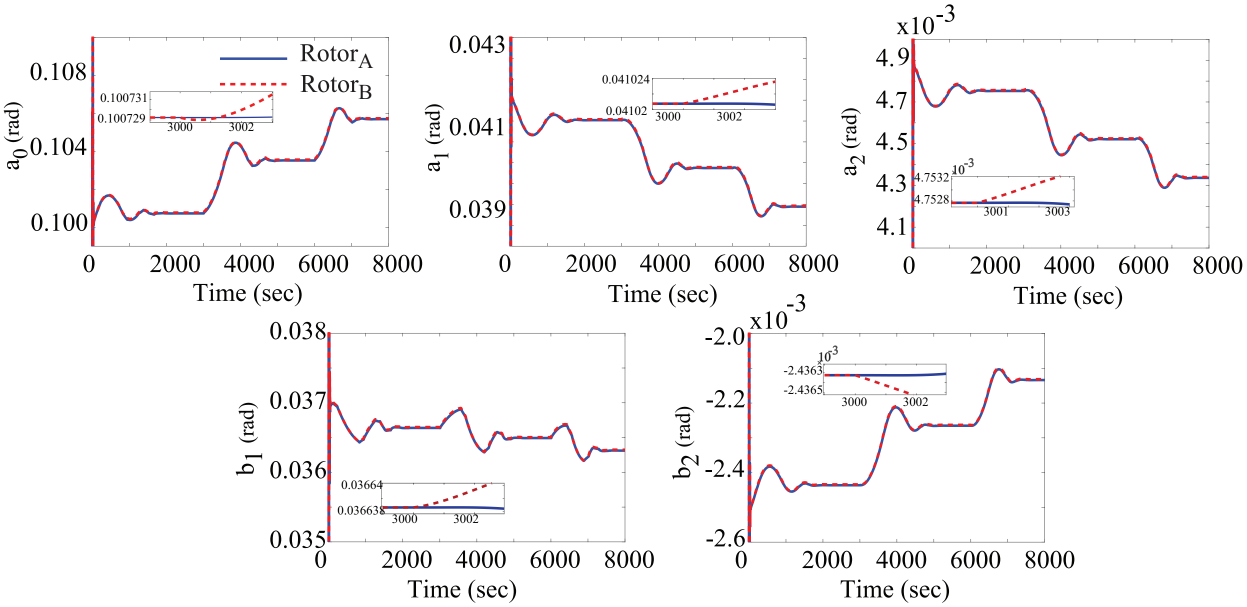

Figure 6.11: Effect of PD controller on the Fourier coefficients;

When reference altitude is set at a low value, for example z_d= 720 m, the associated μ becomes very high shown in Fig. 6.10(a). This corroborates the equilibrium characteristics with respect to μ shown in Fig.4.3.

Figure 6.11 shows that the Fourier coefficients of both rotors differ slightly during the transition of altitude. The convergence of the coefficients of both rotors to the same value suggests that the PD control stabilizes the Fourier coefficients and steady flapping is achieved. Thus, the PD controller creates complete stabilization of the system within the whole operating region.

6.1.1 Hovering at a Certain Altitude with Drops in Wind Speed

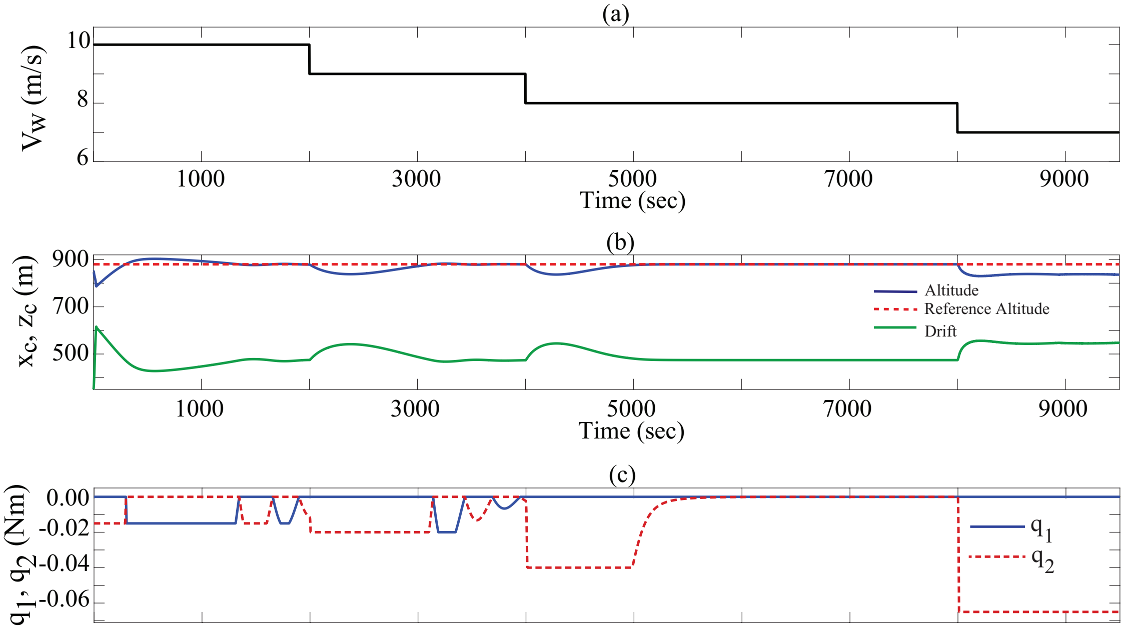

Figure 6.12: Hovering performance with drops in V_w with P controller: (a) Wind speed change; (b) Altitude and drift, reference altitude set at 880m; (c) Applied braking torques

In this section, the results showing the hovering ability of the autogyro during sudden drops in wind speed are presented. As the wind speed decreases, to maintain the fixed reference altitude, the limit of control input needs to be increased. In Table 6.1, the selected limits of q_1, q_2 with changing wind speeds are given. Figure 6.12 shows that the P controller effectively maintains a high altitude when wind speed drops from 10 m/s to 8 m/s. For this case, the reference altitude is set at 880 m. Further decrease in V_w results in the failure of tracking the altitude. This is because maintaining a high altitude at a lower wind speed causes instabilities in the system. From Fig. 4.5, it is seen that as V_w drops, the equilibrium space becomes narrower. The pitch angle and the tether tension associated with 7 m/s wind speed shown in Fig. 6.13(a)-(b) are very high and the tip-speed ratio demonstrated in Fig. 6.14(a) are very low causing autogyro to operate outside the operating region. This leads to instabilities in thrust forces and in aerodynamic torques exhibited in 6.13 (b)-(c) and inflow ratio λ shown in 6.14(b). Figure 6.13(d) suggests that rotor speeds increase significantly when wind speed drops to sustain the set altitude.

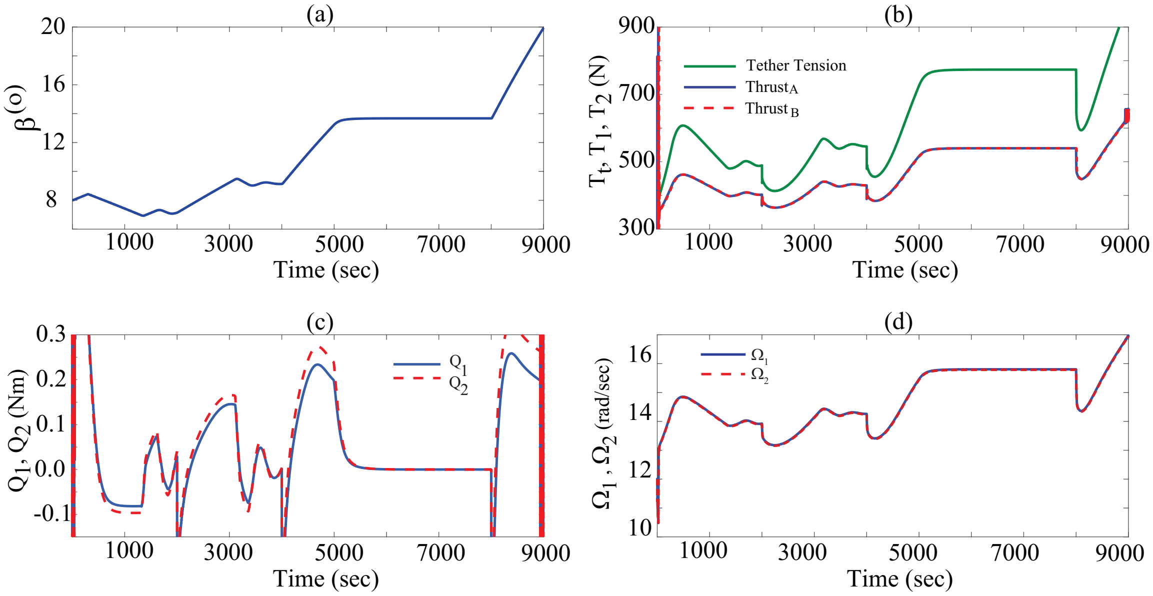

Figure 6.13: Effect of V_w drops with P controller: (a) Pitch angle; (b) Tether Tension and Thrust forces; (c) Aerodynamic torques Q_1, Q_2; (d) Rotational speeds Ω_1, Ω_2

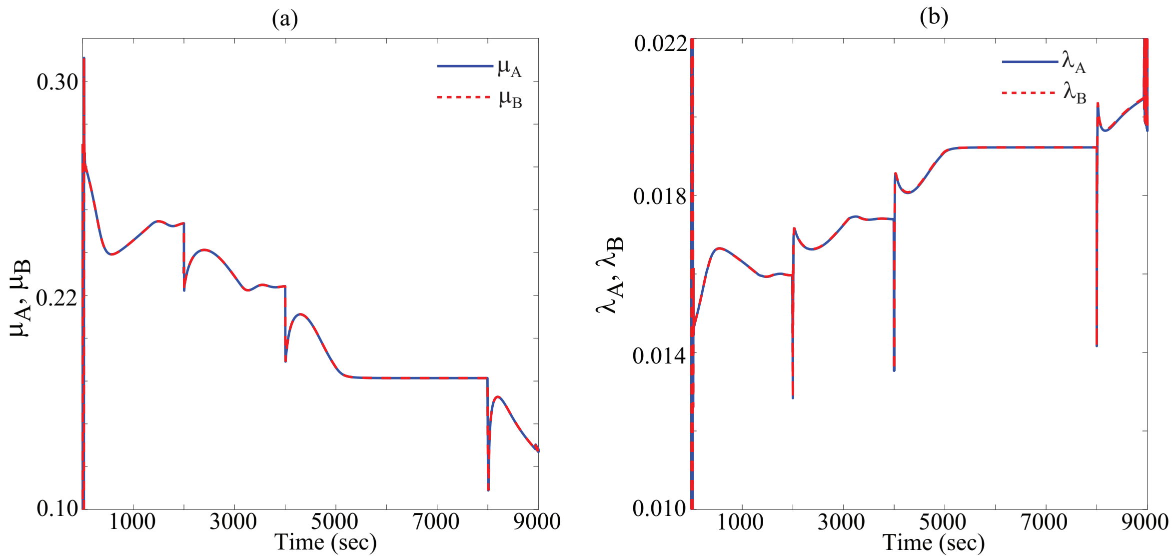

Figure 6.14: Effect of V_w drops with P controller on: (a)Tip-speed ratio; (b)Inflow ratio;

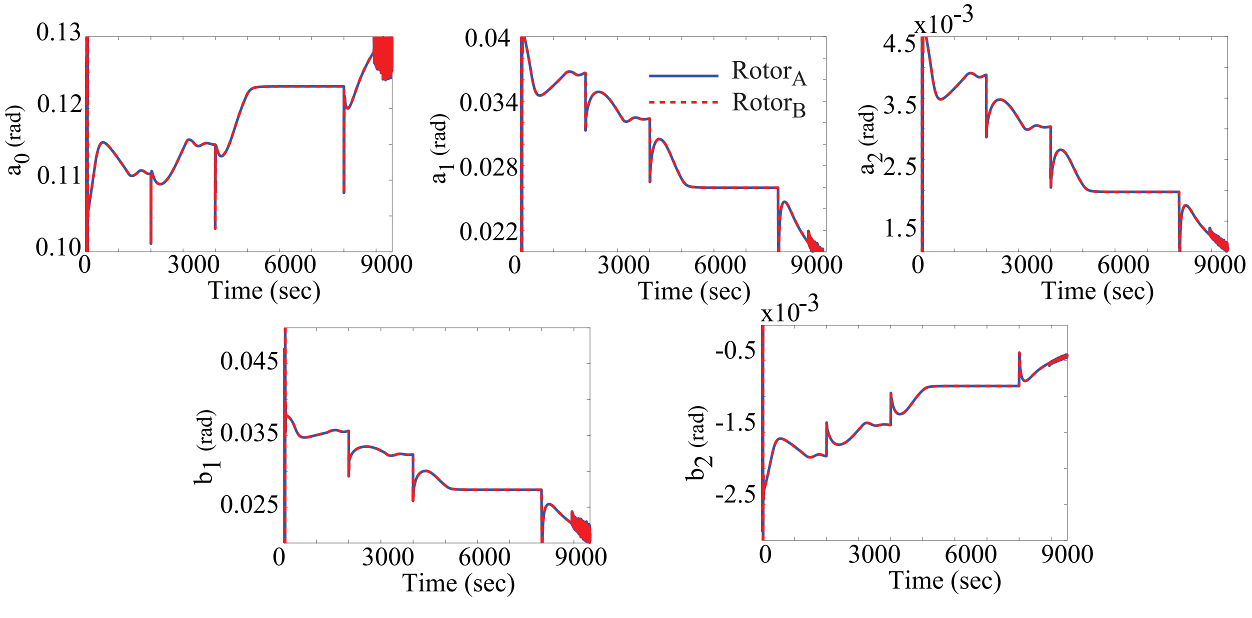

Figure 6.15: Effect of V_w drops with P controller on the Fourier coefficients

The instabilities also appear in the Fourier coefficients at a lower wind speed of 7 m/s, demonstrated in Fig. 6.15. Due to these instabilities in the dynamic system, the proportional controller cannot perform well to maintain a higher altitude at a comparatively lower wind speed.

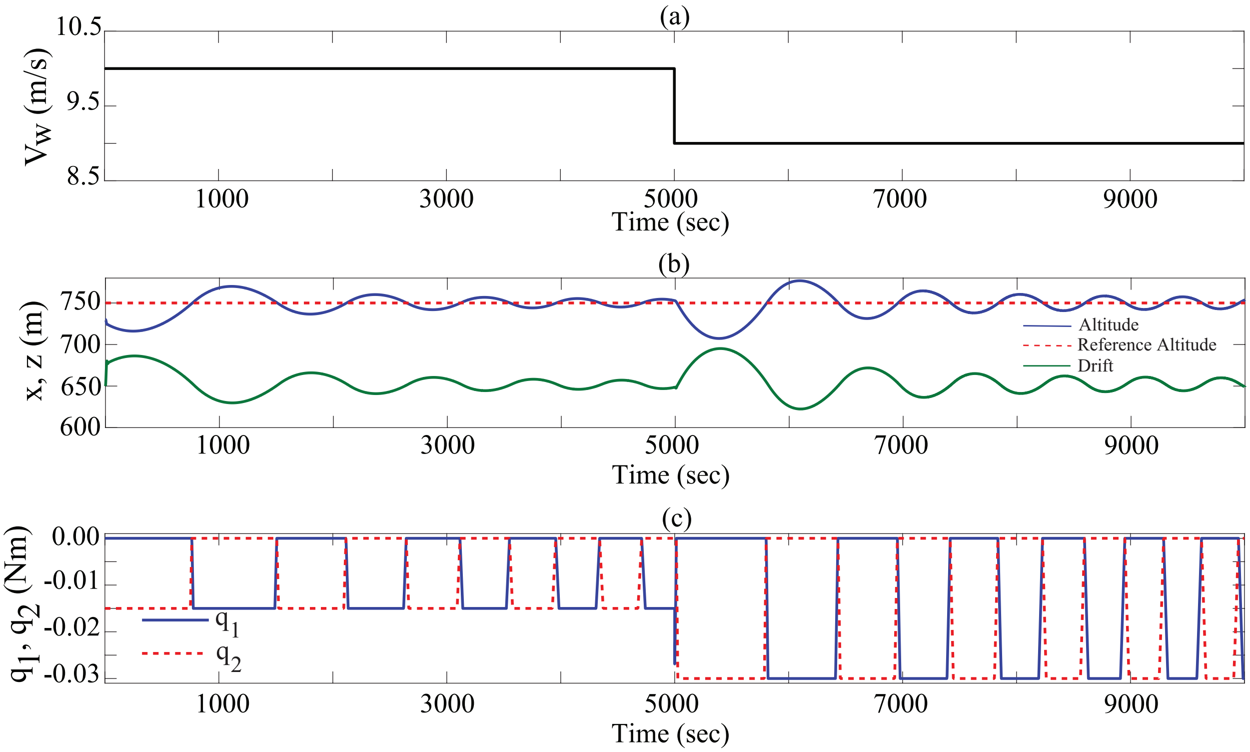

Figure 6.16: Hovering performance with drops in V_w at lower z_d with P controller: (a) Wind speed change; (b) Altitude and drift, reference altitude set at 750 m; (c) Applied braking torques

It is shown in Fig. 6.16 that the proportional controller alone can not enable the system to follow the reference altitude even at 10 m/s wind speed if z_d is set at 75% of tether length, i.e here z_d= 750 m which may be attributed to the unavailability of enough tether tension at high μ values. Figure 6.16(c) shows that despite the allowable braking torque limit is increased from (-0.015,0) to (-0.03,0), the proportional controller is unable to track the desired altitude.

From Fig. 6.17, it can be seen that the proportional controller cannot stabilize the pitch angle

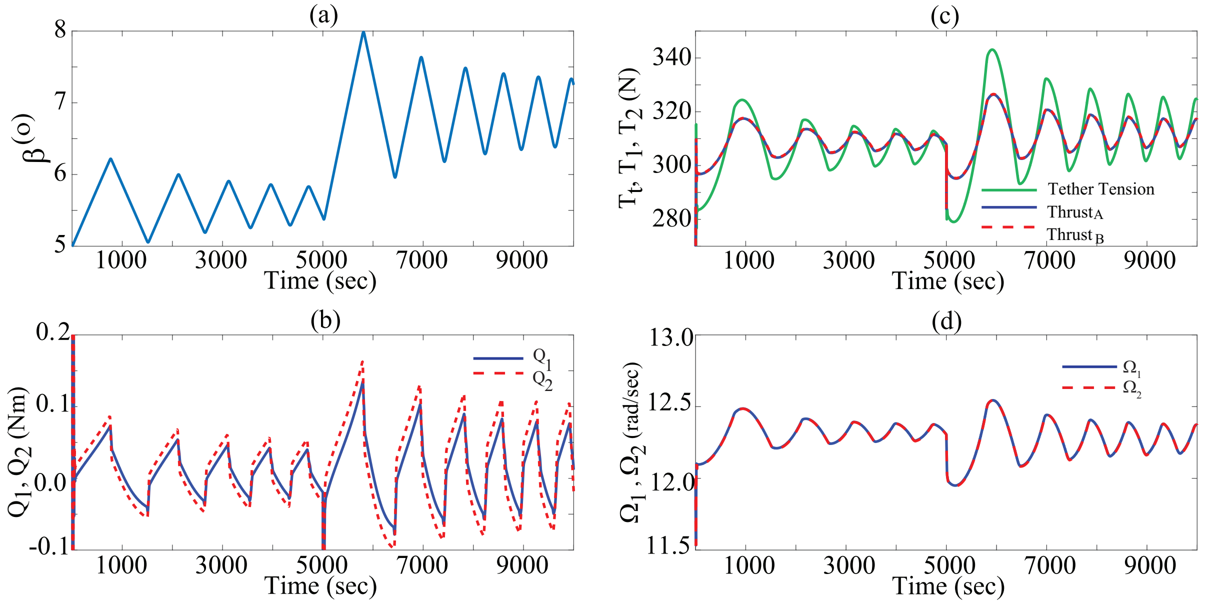

Figure 6.17: Effect of V_w drops at lower z_d with P controller: (a) Pitch angle; (b) Tether Tension and Thrust forces; (c) Aerodynamic torques Q_1, Q_2; (d) Rotational speeds Ω_1, Ω_2

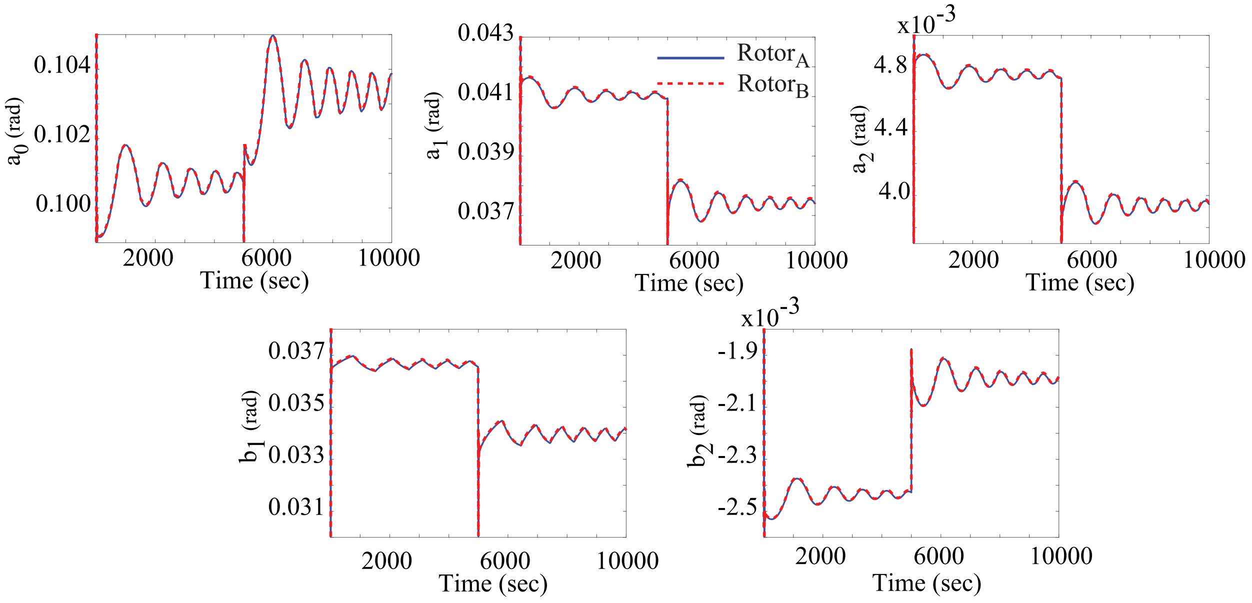

Figure 6.18: Effect of V_w drops at lower z_d with P controller on the Fourier coefficients

β, thrusts, tether tensions, aerodynamic torques and rotor speeds when z_d set at a lower value. Also, Fig. 6.17(c) proves that indeed tether tension is low and sometimes lower than the thrust forces. The oscillatory motions in the Fourier coefficients in Fig. 6.18 indicate, that flapping is not stabilized by the proportional controller due to a lack of restoring force from the tether.

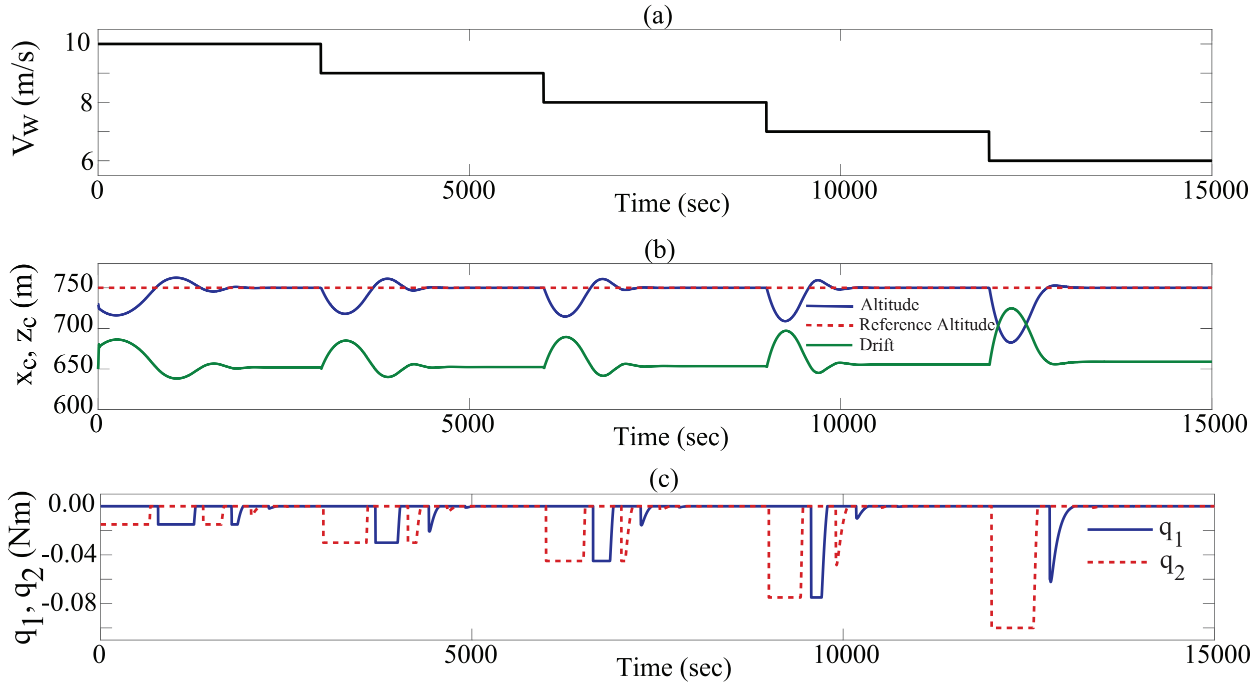

Figure 6.19: Hovering performance with drops in V_w at lower z_d with PD controller: (a) Wind speed change; (b) Altitude and drift; (c) Applied braking torques

The PD controller demonstrates the best performance in maintaining the altitude if a sudden change in V_w occurs when the reference altitude is set at lower values. It enables the system to follow reference altitude even at 6 m/s wind speed, exhibited in Fig.6.19(a)-(b), but the control limit must be increased by a significant amount to achieve this goal as seen in Fig.6.19(c). To maintain the altitude at 750 m when V_w drops to 6 m/s, the allowable limit of braking torques is increased from (-0.015,0) to (-0.1,0). Figure 6.20 (a)-(b) shows PD controller can effectively stabilize the system's pitch angle and thrust forces. It also enables aerodynamic torques to converge to 0, as shown in

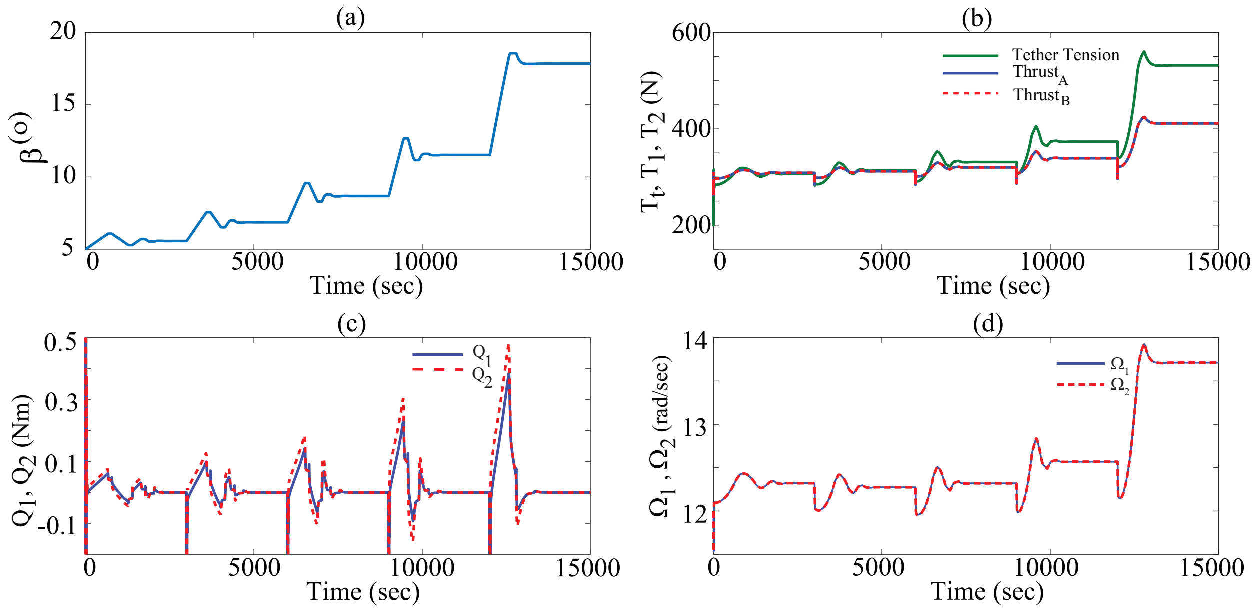

Figure 6.20: Effect of V_w drops at lower z_d with PD controller: (a) Pitch angle; (b) Tether Tension and Thrust forces; (c) Aerodynamic torques Q_1, Q_2; (d) Rotational speeds Ω_1, Ω_2

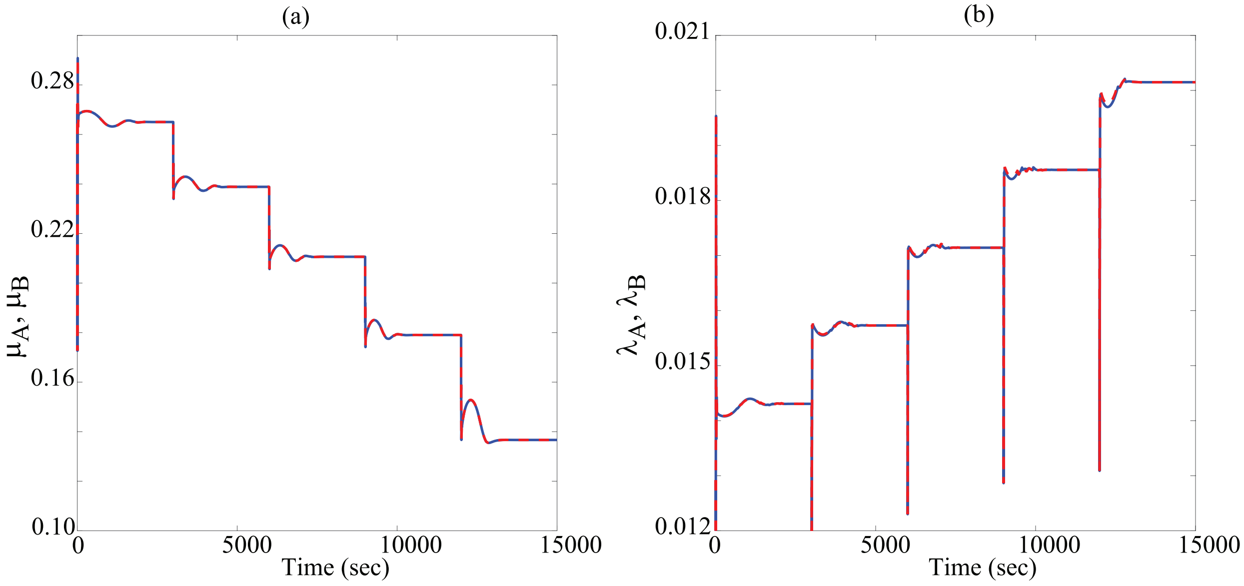

Figure 6.21: Effect of V_w drops with PD controller on: (a)Tip-speed ratio; (b)Inflow ratio;

Fig. 6.20(c). The rotor speeds also converge to steady-state values due to PD control action, as seen in Fig. 6.20(d). This convergence can be attributed to the additional restoring effect provided by the PD controller besides the tether. Figure 6.21(a) shows that the tip-speed ratio drops with the decrease in wind speed to maintain the altitude indicating that PD controller tries to bring the autogyro back in the operating region. The increase in inflow ratios λ with drop in wind speed in Fig. 6.21(a) suggest that they are more influenced by the system's pitch angle β than rotor speeds and wind speed.

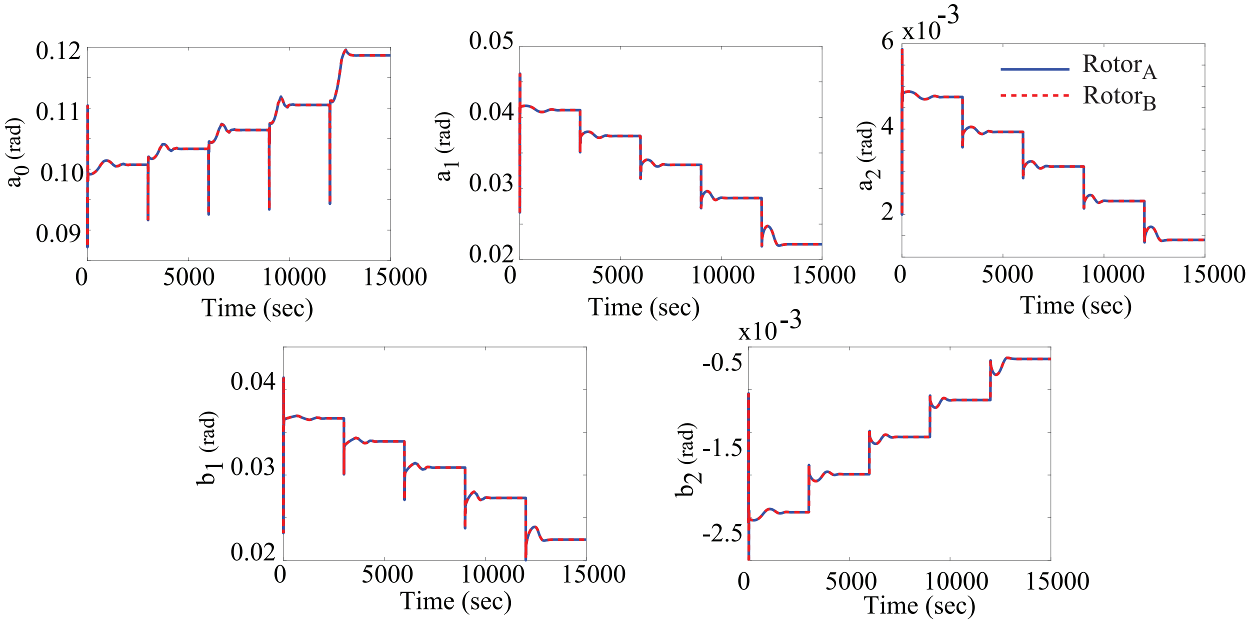

Figure 6.22: Effect of V_w drops at lower z_d with PD controller on the Fourier coefficients

The dependency of the Fourier coefficients on the wind speed can be understood from the Fig. 6.22 where it shows that, a_o, b_2 increase with decreasing wind speed V_w whereas a_1, a_2, b_1 decrease with the wind speed. The convergence of the Fourier coefficients to steady-state values proves the complete stabilization of the system by the PD controller within whole the operating region.

6.1.2 *Horizontal Drifting at a Certain Altitude*

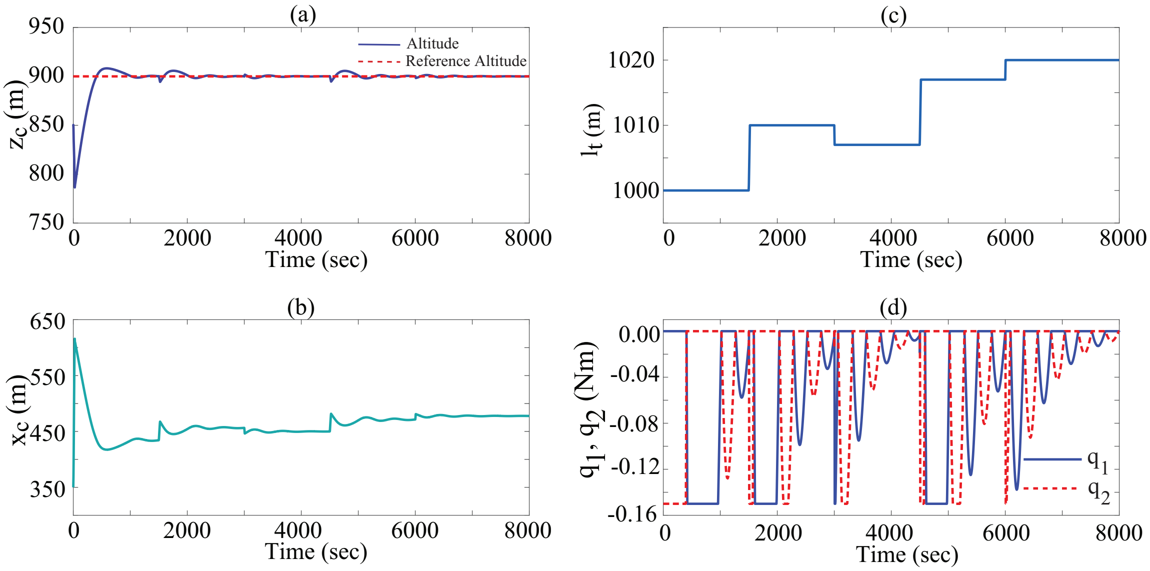

Figure 6.23: Drifting performance at V_w= 10 m/s with P controller: (a) Hovering Altitude fixed at 900 m; (b) Autogyro's Drift; (c) Step change in Tether length, l_t; (d) Applied braking torques

From the results presented in previous sections, it is evident that the PD controller is more effective in controlling the pitch and altitude of the system within the operating limit than the P controller. In this section, Both P and PD controllers are employed to investigate the drifting capabilities in the horizontal direction while maintaining the altitude. The altitude is fixed at 900 m.

From Fig. 6.23(a),(b) and Fig. 6.24(a),(b) it is visible that both the controllers enable the system to hover at a reference altitude set at 900 m while horizontal drift can be induced into the system by changing the tether length l_t. The tether length is varied between 1000 m to 1020 m for both cases, shown in Fig. 6.23(c) and Fig. 6.24(c). When l_t is increased by 10 m, drift is increased approximately by 20m. A decrease in l_t by 3 m causes autogyro to move left by 6 m. It can be concluded that the magnitude of change in tether length, results in twice that magnitude of change in the horizontal position of the system while maintaining the fixed altitude. As expected, the PD

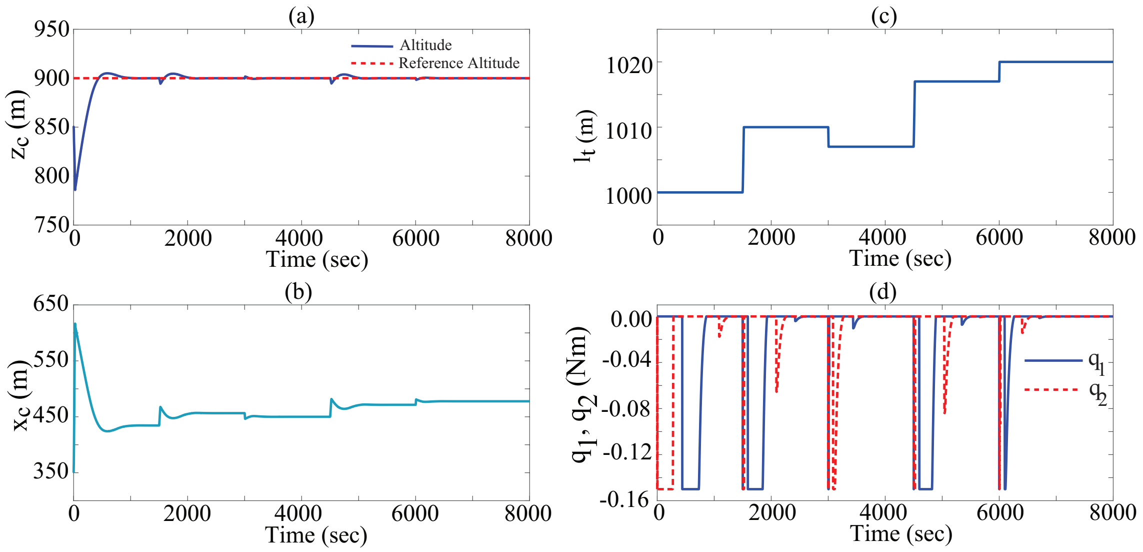

Figure 6.24: Drifting performance at V_w= 10 m/s with PD controller: (a) Hovering Altitude fixed at 900 m ; (b) Autogyro's Drift; (c) Change in Tether length; (d) Applied braking torques

controller requires smaller braking torque and provides more robust control to maintain altitude than the P controller. Figures 6.23(d) and 6.24(d) suggest that switching between q_1 and q_2 is more frequent in the P controller case.

The responses of pitch angle, aerodynamic torques and rotor speeds along with tether tension and thrust forces are presented in Figs. 6.25 and 6.26. Figure 6.25(a) shows that pitch modulation by the P controller is not very efficient as it oscillates while maintaining the altitude. Allowing more simulation time before changing l_t may have stabilized β. However, the PD controller modulates β within the selected time frame, as can be seen in Fig. 6.26(a). Figures 6.25(c) and 6.26(c) illustrate that the tether tension T_t and thrust forces of both rotors decrease with increasing l_t. The decrease in T_t also aids autogyro to move to the right. The aerodynamic torques, presented in Figs. 6.25(b) and 6.26(b), show a very sharp change in values during the transition before converging to 0. The PD controller also removes oscillations from Q_1 and Q_2.

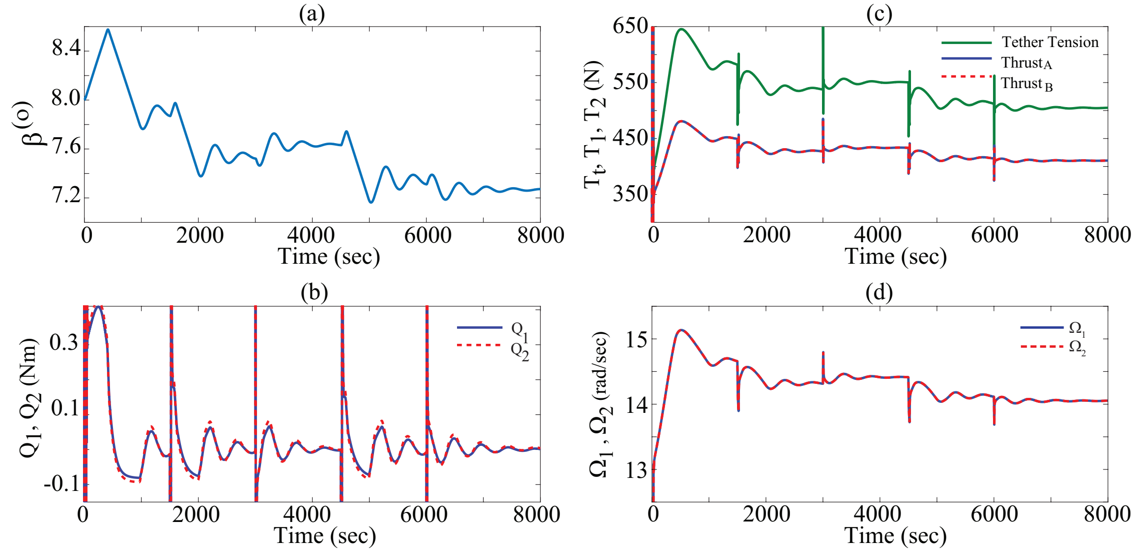

Figure 6.25: Drifting performance at V_w= 10 m/s with P controller: (a) Pitch angle; (b) Aerodynamic torques Q_1, Q_2; (c) Tether Tension and Thrust forces; (d) Rotational speeds Ω_1, Ω_2

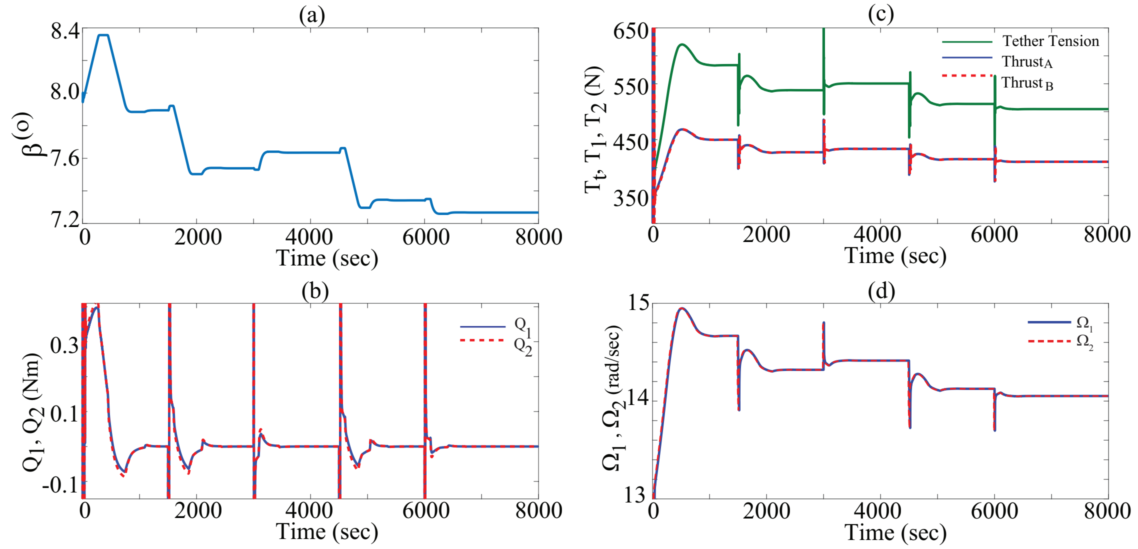

Figure 6.26: Drifting performance at V_w= 10 m/s with PD controller:(a) Pitch angle; (b) Aerodynamic torques Q_1, Q_2; (c) Tether Tension and Thrust forces; (d) Rotational speeds Ω_1, Ω_2

Figures 6.25(d) and 6.26(d) demonstrate that the rotor speeds decrease with increasing l_t at a fixed uniform V_w while altitude is kept fixed.

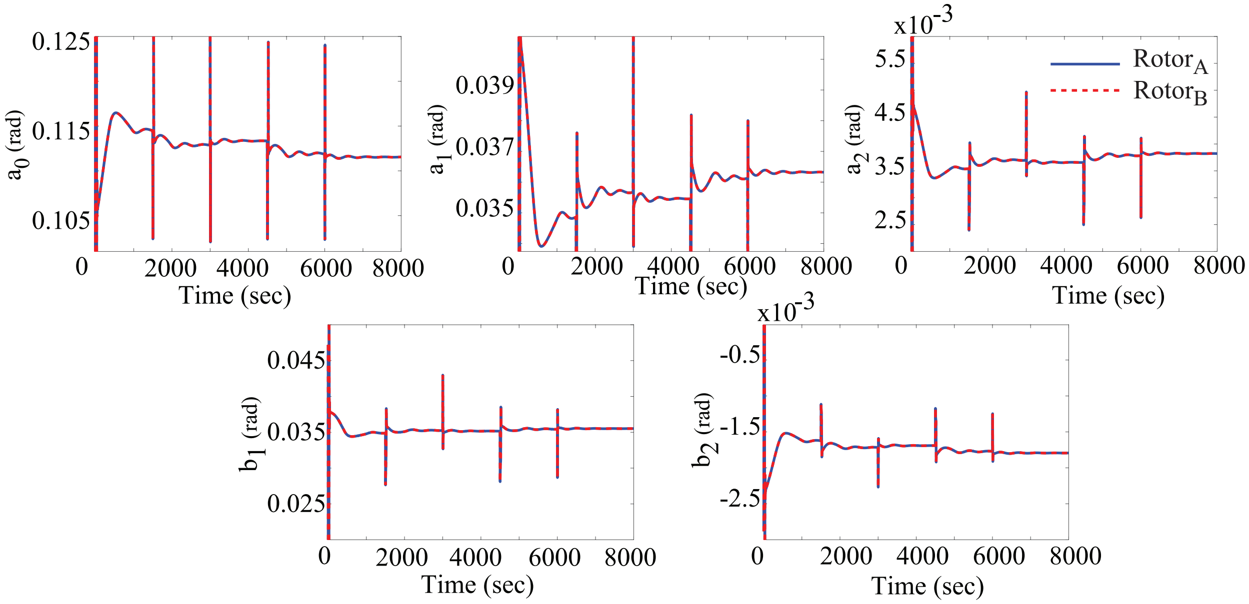

Figure 6.27: Drifting performance at V_w= 10 m/s with P controller: Fourier Coefficients

Next, the blade flapping dynamics associated with drifting at a fixed altitude are presented in Figs. 6.27 and 6.28 via the Fourier coefficients. The PD controller removes even the slight oscillations that are present when the P controller is applied. The coefficients a_0, b_2 decrease with increasing l_t, while a_1, a_2 increases with l_t, However, b_1 is indifferent to l_t change. The blade flapping is more sensitive to V_w change as demonstrated in Fig. 6.22 than the tether length change. The transient responses of the system in the drifting phenomenon show sharp peaks. This may be attributed to the step change in l_t. A more gradual change in tether length may reduce the peaks from the responses.

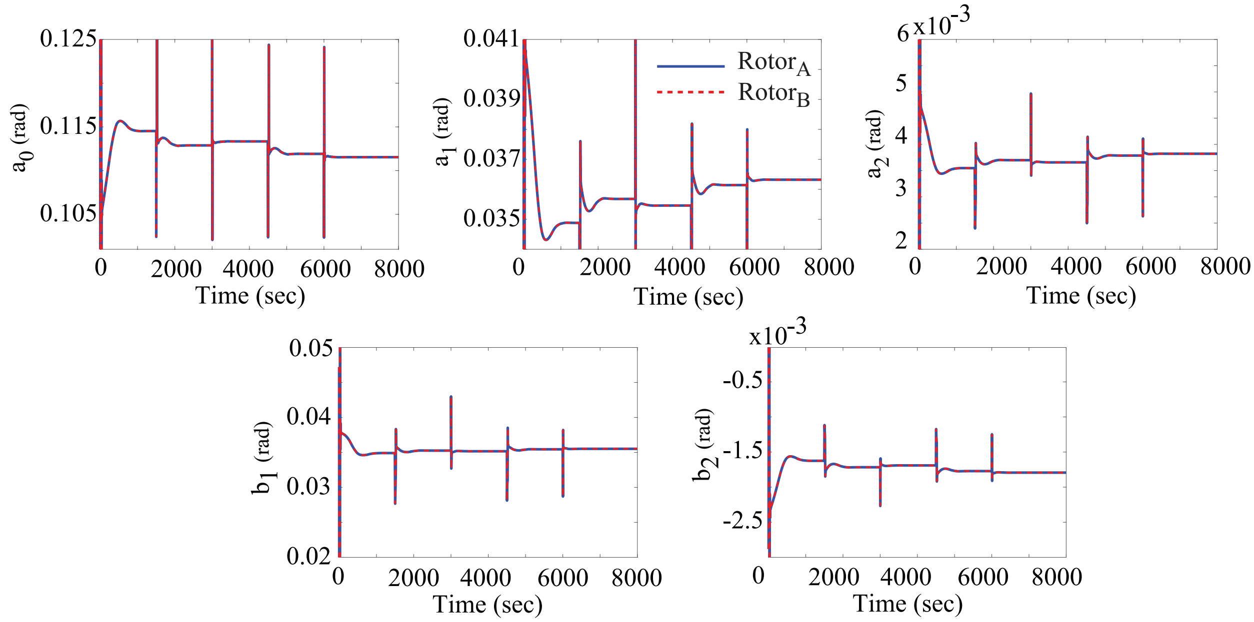

Figure 6.28: Drifting performance at V_w= 10 m/s with PD controller: Fourier Coefficients

6.2 Controller Performance in Variable Wind Field

In a practical scenario, wind speed does not remain constant. In this section, the performances of the controllers in the presence of a variable wind profile are inspected. The variable wind speed, V_w, is generated using TurbSim [61]. Wind speed V_w is varied between 9 m/s and 11.5 m/s.

It is established that in this study the P controller works reasonably in tracking the reference altitudes where enough tension force is available from the tether whereas the PD works well in the uniform wind field within the operating region. So, the P controller is applied in the presence of a variable wind field to track reference altitudes set at 870 m, 920 m and 890 m. The proposed proportional controller enables the autogyro to go the desired altitude z_d within the operating region with an acceptable diversion from the set reference point as can be seen in Fig. 6.29(a). Figure 6.29(b) shows the braking torques required as control input. The proportional control gain, K_p,

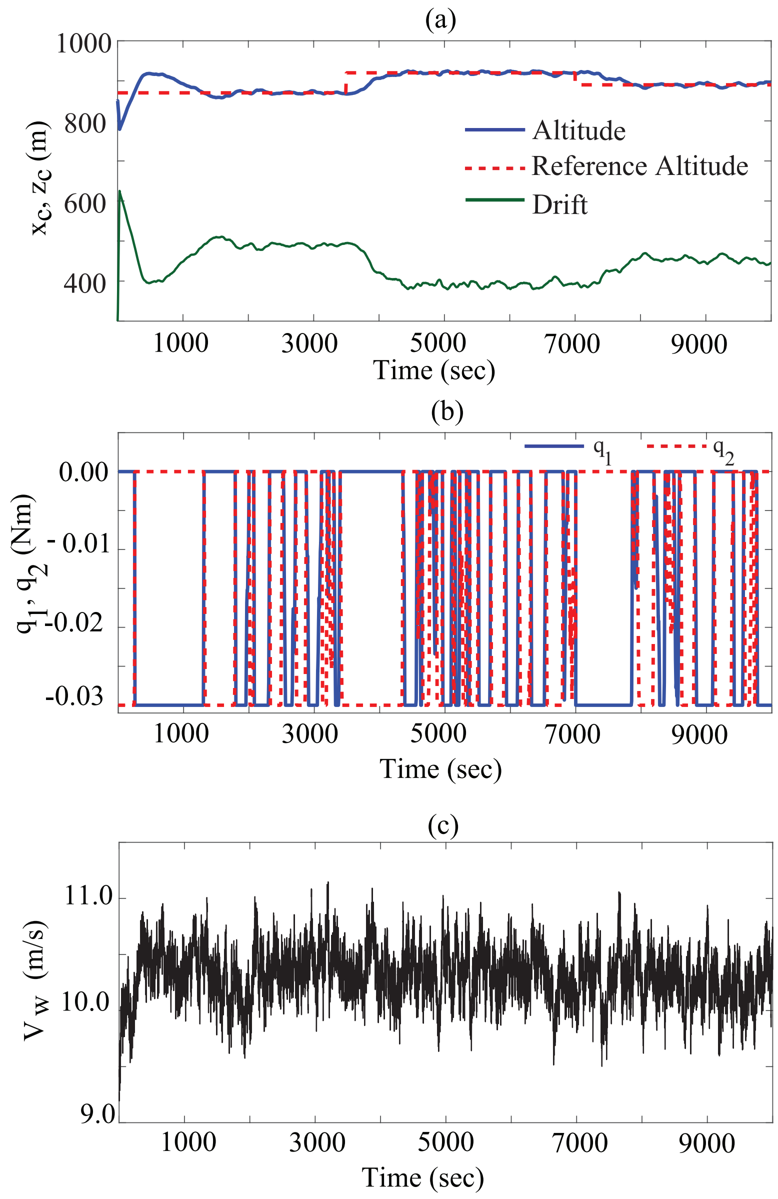

Figure 6.29: Altitude control with P controller in the presence of variable wind speed: (a) reference set at 870 m,920 m and 890 m; (b) Applied braking torques; (c) Variable wind profile generated by TurbSim;

is chosen to be 0.025. The K_p value and allowable limit of control input as braking torque are higher than uniform wind speed cases. It is obvious because controlling altitude at variable wind speeds requires a greater control effort. The corresponding variable wind field is presented in Fig. 6.29(c). Change in altitude is sensitive to changes in pitch angle β. Hence, the K_p value is chosen to be small to regulate gradual change in β caused by q_1 and q_2 and to demonstrate the viability of the controller in the presence of variable wind field. Table 6.2 lists the chosen limit and controller gains used in the simulations for variable wind speed.

Table 6.2: Controller Parameters in Variable V_W

Controller Type	$\|K_p\|$	$\|K_d\|$	Allowable Range (N-m)
P	0.025	$--$	$[-0.03, 0]$
PD	0.025	2	$[-0.03, 0]$

Figure 6.30 illustrates the corresponding pitch angle, thrusts, tether tensions, aerodynamic torques and rotor speeds when braking torques are applied.

In a variable wind field, the response of the system can not be expected to converge to a single steady value like the uniform wind field scenario. Pitch angle β, shown in Fig. 6.30(a), varies in time due to the variabilities in wind speed. The unsteady tether tension, thrust forces and rotor speeds increase with altitude and decrease when autogyro follows the decreased z_d with applied P control, as can be seen in Fig. 6.30(b).

The unsteady aerodynamic torques of both rotors, presented in Fig. 6.30(c), reveal the dynamic characteristics of the system. Unlike the steady-state model where aerodynamic torques is zero, the model calculates Q_1, Q_2 proving its efficacy in capturing the dynamics. The corresponding tip-speed ratios and inflow ratios in variable wind speed are shown in Fig. 6.31. The overlapping plots suggest that even at variable wind speeds, the responses from the rotors are similar and the values differ slightly during control action. Figure 6.31 also exhibits the inverse relationship between tip-speed ratio and inflow ratio which is also found in uniform V_w case. The Fourier

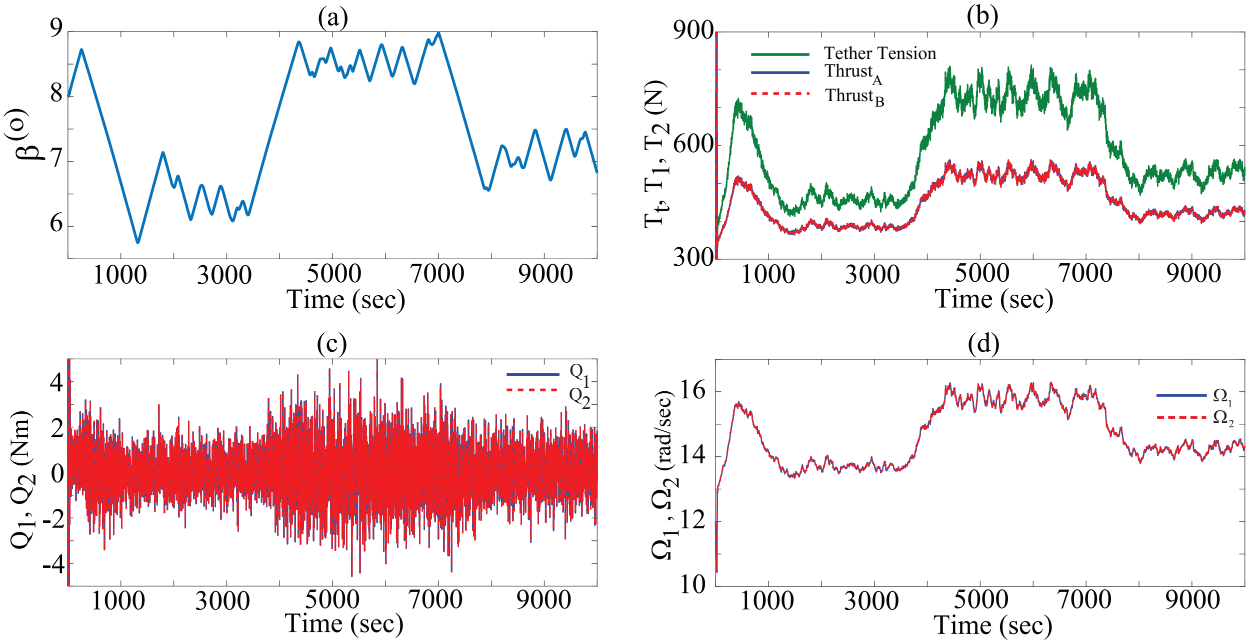

Figure 6.30: P controller performance in the presence of variable wind speed: (a) Pitch angle; (b) Tether Tension and Thrust forces; (c) Aerodynamic torques Q_1, Q_2; (d) Rotational speeds Ω_1, Ω_2

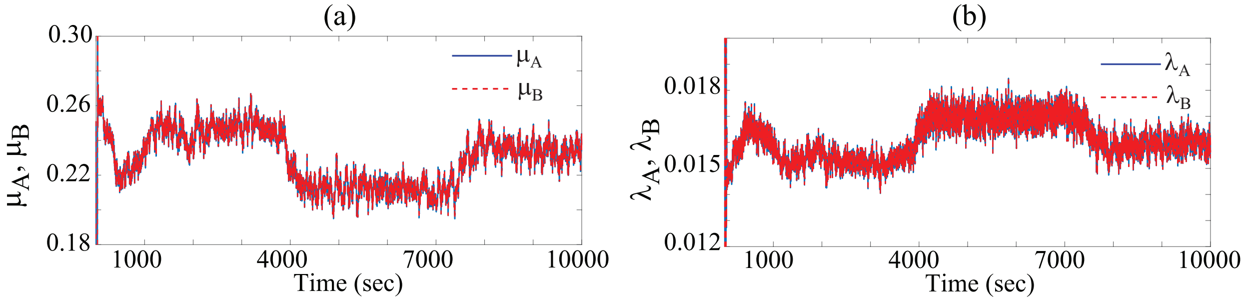

Figure 6.31: P controller performance in the presence of variable wind speed: (a) Tip-speed ratio; (b)Inflow ratio

coefficients, presented in Fig. 6.32, suggest that the blade flapping of the rotors are also similar as the coefficients of both rotors overlap. The unsteady nature of the response of the coefficients proves flapping of the blades is highly influenced by the variabilities in wind speed.

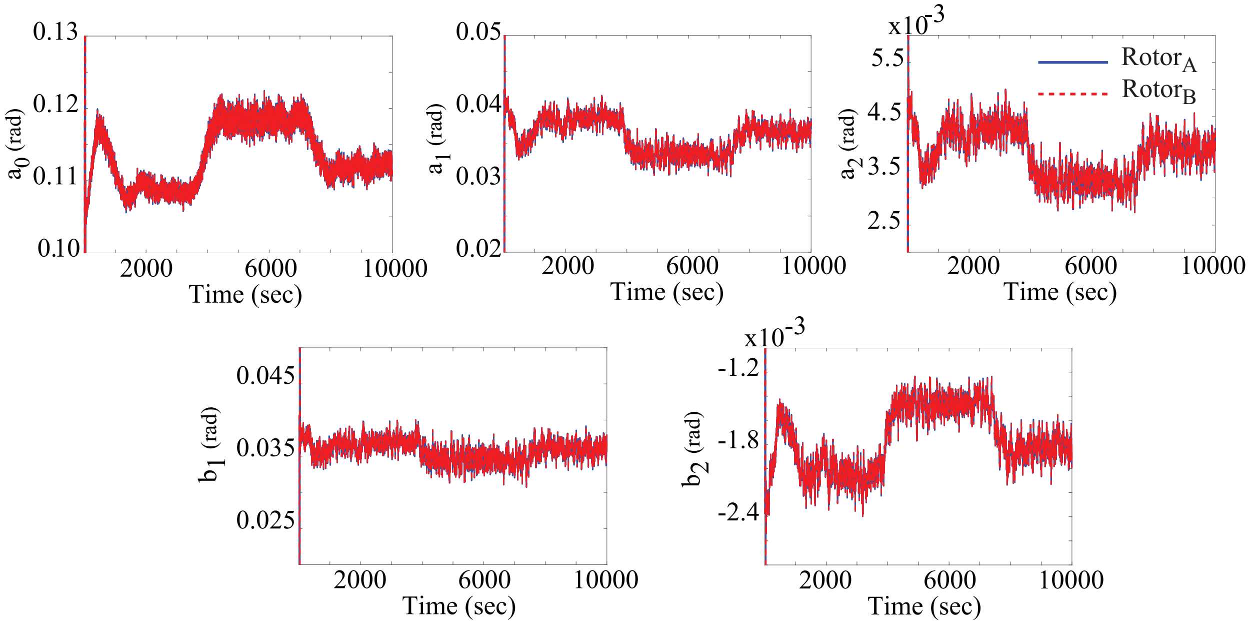

Figure 6.32: P controller performance in the presence of variable wind speed: Fourier coefficients

Next, the PD controller is applied near the region where μ is high and the tether is slack with the same wind field. The simulation results demonstrating the performance of the PD controllers in the variable wind speed are presented in Figures 6.33-6.36. The results in Fig. 6.33 show autogyro can track the reference altitude of 760 m, 810 m and 880 m effectively with slight deviations when the PD control is applied.

Figure 6.33(c) suggests that the switching between q_1 and q_2 is more often in this case than the proportional controller. Even the PD control action can not stabilize pitch angle, β, as seen in Fig. 6.34(a).

The low tether tension provided by the tether at z_d= 760 m and 810 m is depicted in Fig. 6.34(b). However, tether tension is increased at z_d= 880 m indicating both P and PD will work at this altitude. The aerodynamic torques variabilities in Fig. 6.34(c) show the magnitude of fluctuations

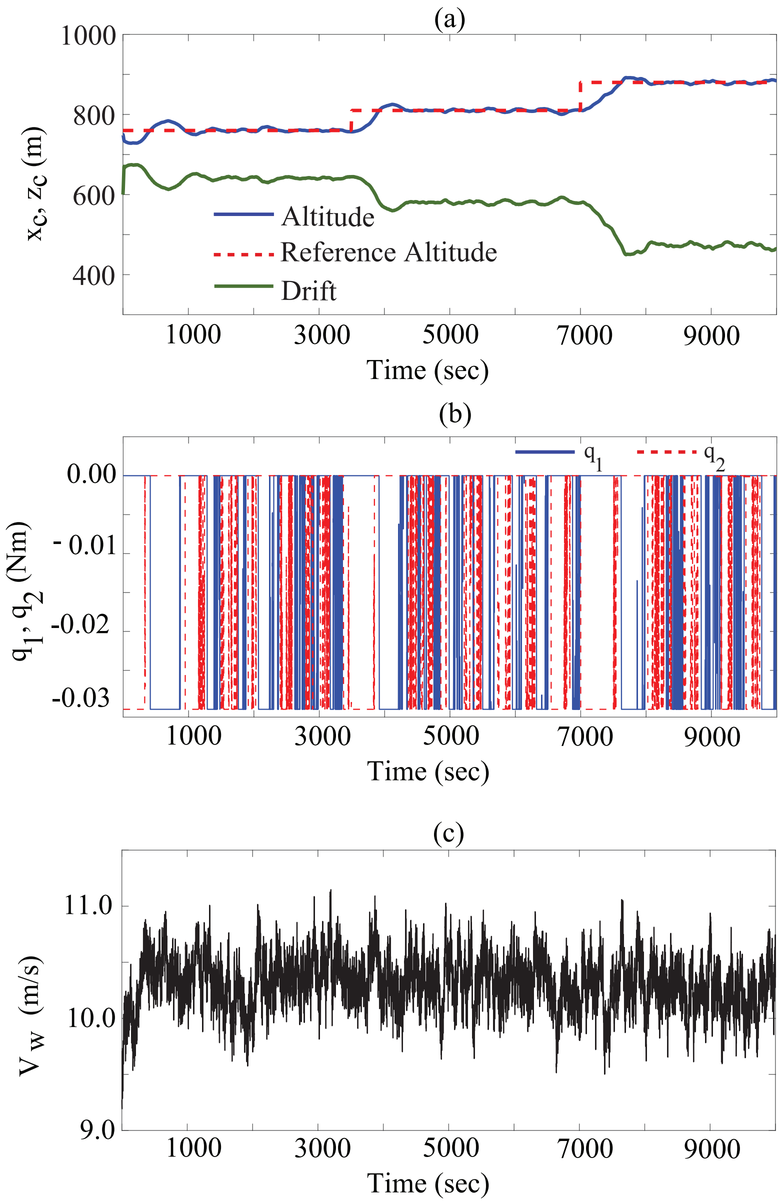

Figure 6.33: Altitude control with PD controller in the presence of variable wind speed: (a) reference set at 760 m, 810 m and 880 m; (b) Applied braking torques;(c) variable wind profile generated by TurbSim

in Q_1 and Q_2 increases as reference altitude is increased. This trend can also be noticed in Fig. 6.30(c) in the P controller case. In Fig. 6.34(d), the corresponding rotor speeds are presented. The

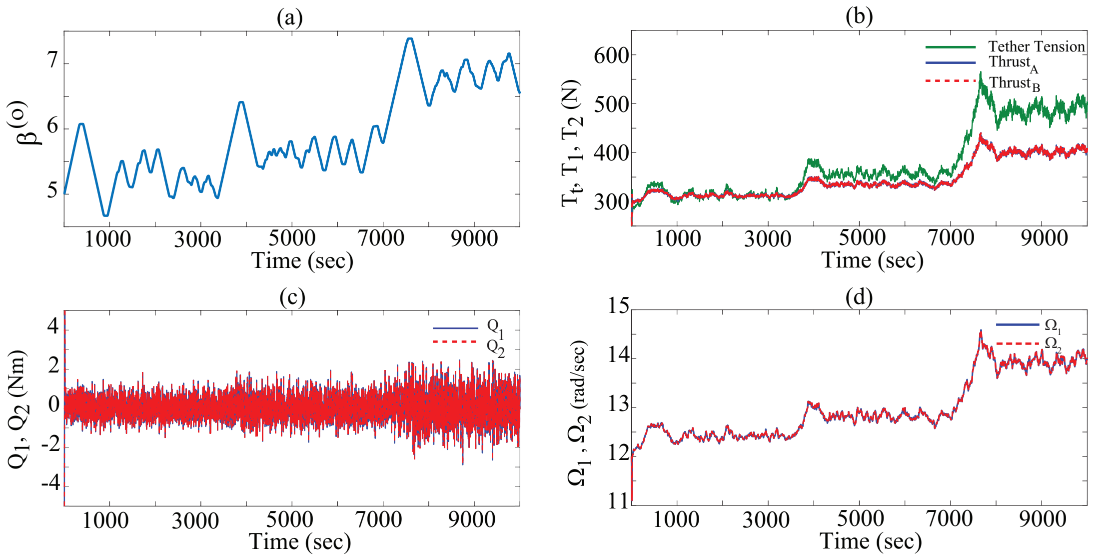

Figure 6.34: PD controller performance in the presence of variable wind speed: (a) Pitch angle; (b) Tether Tension and Thrust forces; (c) Aerodynamic torques Q_1, Q_2; (d) Rotational speeds Ω_1, Ω_2

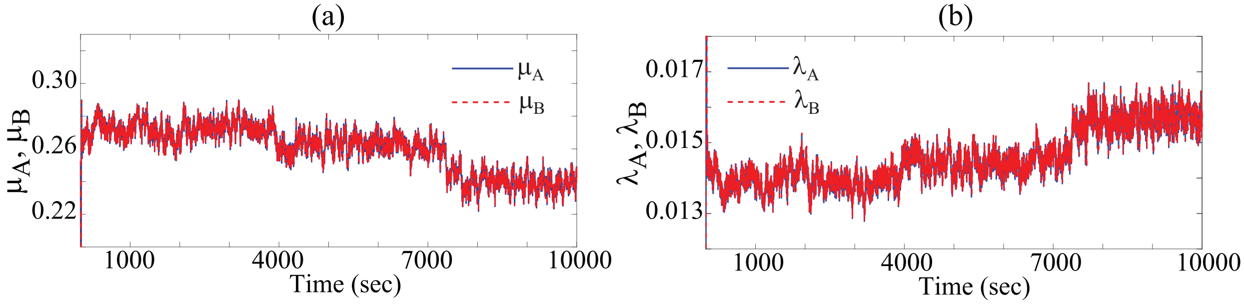

Figure 6.35: PD controller performance in the presence of variable wind speed: (a) Tip-speed ratio; (b)Inflow ratio

rotor speeds in general increase as autogyro follows increasing desired altitude. But, they differ very slightly due to braking action, which is reflected through β in Fig. 6.30(a). The high tip-peed ratios shown in Fig. 6.35(a) are associated with low reference altitude discussed in Chapter 4. Both the tip-speed and the inflow ratios are influenced by the unsteady wind field. The oscillations

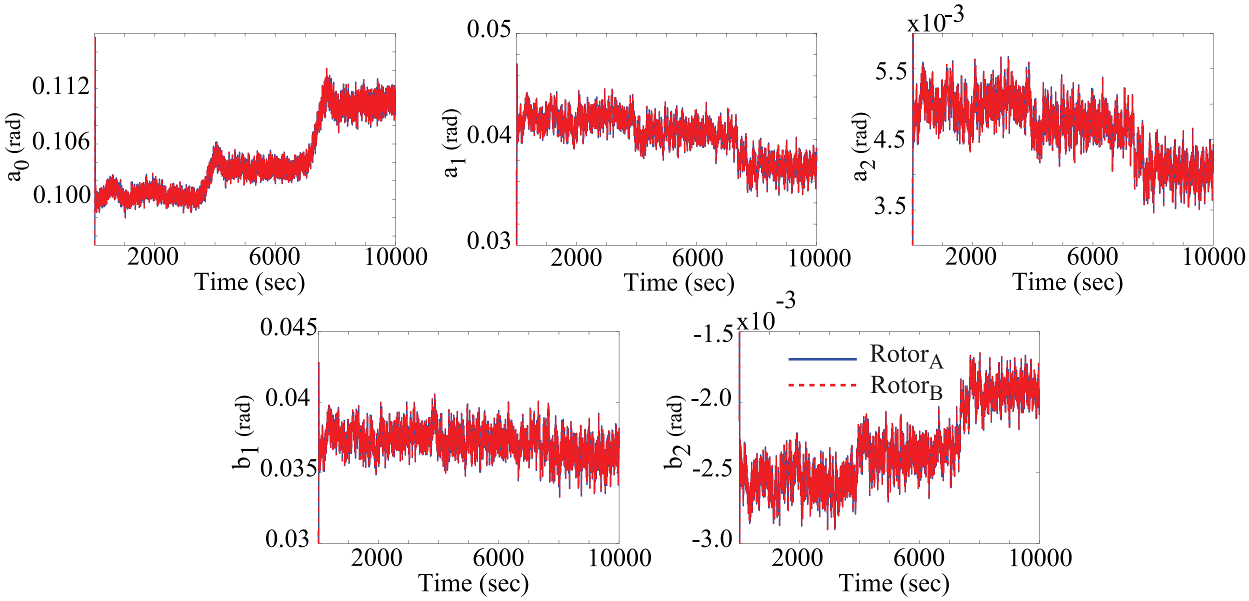

Figure 6.36: PD controller performance in the presence of variable wind speed: Fourier coefficients

present in the Fourier coefficients in Fig. 6.36 exhibit the dependency of blade flapping on wind speed. The superimposed response of rotor A and rotor B, as seen in Figs. 6.35 and 6.36, indicate that unsteady wind field influences the two rotors in a similar way.

CHAPTER 7: CONCLUSION

7.1 Summary

This thesis explores the idea of establishing a tethered multirotor autogyro system to be a potential candidate for an energy-efficient surveillance device that may replace drones. A dynamic model of such a system is developed in the 2D plane by extending upon the existing steady-state model which combines Blade Element Theory (BEM) and static catenary mechanics. Kinetic analysis is done to produce equations of motion of the system. An overview of transient properties is given and equilibrium characteristics are analyzed and presented through simulating the model without applying any control. Operating regions of the system are identified where control action can be effective with respect to the tip-speed ratio and the system's pitch angle. It is also shown that the operating regions are mostly insensitive to the change in wind speed although they get narrower with lower wind speeds. However, the operating regions change with tether length indicating the hovering capability of the system.

Next, a pitch and altitude control study of the system is conducted. A proportional feedback controller is designed which takes braking torques as control inputs. The simulation results show that the designed controller performs well in tracking the reference altitude making the error go to zero. Moreover, a closed-loop dynamic analysis is done to explain how the control action yields zero steady-state error. However, the simulation results exhibit that the proposed proportional controller is not so effective when the autogyro operates at an altitude less than 85% of the tether length associated with a high tip speed ratio. This may be attributed to the low tether tension provided by the slack tether as seen from the simulation results. So, a proportional-derivative (PD) controller is proposed to overcome this limitation in the design. The simulation results show that the PD controller is successful in both high and low-altitude tracking and also it tracks the altitude perfectly at lower wind speeds. The robustness of the PD controller is demonstrated through a closed-loop dynamic study likewise.

Simulation results are presented by demonstrating the hovering abilities of the autogyro while wind speed drops suddenly. The designed Proportional controller can sustain hovering up to the drop of wind speed to 8m/s while maintaining a higher altitude. Further lowering the wind speed caused instabilities in the system when the P controller is in action. However, the PD controller allows the system to maintain altitude even at 6 m/s wind speed within the operating range.

Next, simulation results showing the ability of the horizontal motion of the system in X direction while maintaining a certain altitude are presented. Within the operation region presented in Chapter 4, the system can move in the X direction by reeling in or out the tether where the braking of the rotors maintains the altitude. This is a crucial factor for the autogyro to surveil effectively.

Finally, the study has been extended to evaluate the performance of both the controllers, P and PD, in the presence of a variable wind profile. Results show a good agreement between the system's altitude and the desired altitude in the variable wind profile.

The main focus of this research is to demonstrate the feasibility of braking torque as a control input in controlling the quadcopter-based autogyro's altitude while capturing the transients. This study has successfully achieved this goal by considering a reduced-order model that alleviates some of the complexities of the proposed highly nonlinear systems and allows to concentrate on the control standpoint of the system. Important control characteristics, for example, which controller can be used and where control action would fail can be identified via this developed model. However, to convert this theoretical concept into a practical surveillance device, a higher fidelity model needs to be developed.

7.2 Future Extensions

To achieve in-flight maneuverability and more credibility for the practical application of the presented quadcopter-based tethered autogyro following extensions will be added to the present studies:

1. A comprehensive dynamic model will be developed relaxing the assumption of thrust forces being always along the rotor axes.
2. An extensible tether model will be developed to prevent instabilities caused by the taut tether incorporating tether drag forces in the aerodynamic model.
3. The thorough dynamic model will include flapping degrees of freedom of the system considering dynamic flapping of the blades unlike the reduced order model considered in this study.
4. Positions of the blades will be considered to develop aerodynamic forces and torques instead of the averaged ones considered in this study.
5. Once the detailed model is developed, it will be extended to a full 3D dynamic model considering the effect of the longitudinal force and the lateral torque on the system.
6. Ongoing work also includes a complete stability analysis of the designed controllers.
7. From the control perspective, plans include investigating the switching between the autorotation and powered flight modes when wind is not available
8. Optimization problems can be formulated to find an energy-optimal path in wind fields by investigating the overall energy efficiency of trajectories.

Although a more robust dynamic model will add fidelity to the control study, the reduced order model studied in this research outlines the important characteristics required for control action such as actuation type. It also facilitates the stability analysis of such highly nonlinear systems with coupled equations of motion. A comparison study is required between the reduced order model and the high fidelity model so that the reduced order model can be used for future control endeavors.

LIST OF REFERENCES

[1] W. J. Ockels, "Laddermill, a novel concept to exploit the energy in the airspace," *Aircraft design*, vol. 4, no. 2-3, pp. 81–97, 2001.

[2] M. Canale, L. Fagiano, and M. Milanese, "High altitude wind energy generation using controlled power kites," *IEEE Transactions on Control Systems Technology*, vol. 18, no. 2, pp. 279–293, 2009.

[3] "Tethred aerostat radar system," 2020, https://atlas-lta.com/tethered-aerostats/ [Accessed: (3/23/2024)].

[4] J. B. Wheatley, "An aerodynamic analysis of the autogiro rotor with a comparison between calculated and experimental results," Tech. Rep., 1935.

[5] M. Zhang and X. Li, "Drone-enabled internet-of-things relay for environmental monitoring in remote areas without public networks," *IEEE Internet of Things Journal*, vol. 7, no. 8, pp. 7648–7662, 2020.

[6] K.-W. Chen, M.-R. Xie, Y.-M. Chen, T.-T. Chu, and Y.-B. Lin, "Dronetalk: An internet-of-things-based drone system for last-mile drone delivery," *IEEE Transactions on Intelligent Transportation Systems*, vol. 23, no. 9, pp. 15 204–15 217, 2022.

[7] J. C. Hodgson, S. M. Baylis, R. Mott, A. Herrod, and R. H. Clarke, "Precision wildlife monitoring using unmanned aerial vehicles," *Scientific reports*, vol. 6, no. 1, p. 22574, 2016.

[8] J. Sun, J. Li, T. Zhou, K. Yang, S. Wei, N. Tang, N. Dang, H. Li, X. Qiu, and L. Chen, "Toxicity, a serious concern of thermal runaway from commercial li-ion battery," *Nano Energy*, vol. 27, pp. 313–319, 2016. [Online]. Available: https://www.sciencedirect.com/science/article/pii/S2211285516302130

[9] J. McConnell and T. Das, “Equilibrium behavior of a tethered autogyro: Application in extended flight and power generation,” *Journal of Applied Mechanics*, vol. 89, no. 9, p. 091003, 2022.

[10] G. Riegler and W. Riedler, “Tethered wind systems for the generation of electricity,” *J. Sol. Energy Eng.; (United States)*, vol. 106, 5 1984. [Online]. Available: https://www.osti.gov/biblio/6392567

[11] M. Garcia-Sanz and C. H. Houpis, *Wind energy systems: control engineering design*. CRC press, 2012.

[12] P. Pugh, “Wind generator kite system,” Tech. Rep., 1984.

[13] B. Lansdorp and P. Williams, “The laddermill: Innovative wind energy from high altitudes in holland and australia,” *Windpower 2006*, 2006.

[14] P. Williams, B. Lansdorp, and W. Ockels, “Modeling and control of a kite on a variable length flexible inelastic tether,” in *AIAA Modeling and Simulation Technologies Conference and Exhibit*, 2007, p. 6705.

[15] P. Williams, B. Lansdorp, and W. Ockels, “Nonlinear control and estimation of a tethered kite in changing wind conditions,” *Journal of guidance, control, and dynamics*, vol. 31, no. 3, pp. 793–799, 2008.

[16] P. Williams, B. Lansdorp, and W. Ockesl, “Optimal crosswind towing and power generation with tethered kites,” *Journal of guidance, control, and dynamics*, vol. 31, no. 1, pp. 81–93, 2008.

[17] M. Canale, L. Fagiano, and M. Milanese, “Kitegen: A revolution in wind energy generation,” *Energy*, vol. 34, no. 3, pp. 355–361, 2009.

[18] J. Alonso-Pardo and G. Sánchez-Arriaga, “Kite model with bridle control for wind-power generation,” *Journal of Aircraft*, vol. 52, no. 3, pp. 917–923, 2015.

[19] U. Fechner, R. van der Vlugt, E. Schreuder, and R. Schmehl, “Dynamic model of a pumping kite power system,” *Renewable Energy*, vol. 83, pp. 705–716, 2015.

[20] F. RAPPOLT and R. SHERIDAN, “The utility of small aerostats for surveillance missions,” in *5th Lighter-Than Air Conference*, 1983, p. 1973.

[21] R. Ashford, “Military and civilian applications for tethered aerostats,” in *7th Conference on Sounding Rockets, Balloons and Related Space Systems*, 1986, p. 2513.

[22] V. Gawande, P. Bilaye, A. Gawale, R. Pant, and U. Desai, “Design and fabrication of an aerostat for wireless communication in remote areas,” in *7th AIAA ATIO Conf, 2nd CEIAT Int’l Conf on Innov and Integr in Aero Sciences, 17th LTA Systems Tech Conf; followed by 2nd TEOS Forum*, 2007, p. 7832.

[23] C. Vermillion, B. Glass, and A. Rein, “Lighter-than-air wind energy systems,” in *Airborne wind energy*. Springer, 2013, pp. 501–514.

[24] S. Jones and J. Krausman, “Nonlinear dynamic simulation of a tethered aerostat,” *Journal of aircraft*, vol. 19, no. 8, pp. 679–686, 1982.

[25] C. Lambert and M. Nahon, “Stability analysis of a tethered aerostat,” *Journal of Aircraft*, vol. 40, no. 4, pp. 705–715, 2003.

[26] A. Rajani, R. S. Pant, and K. Sudhakar, “Dynamic stability analysis of a tethered aerostat,” *Journal of aircraft*, vol. 47, no. 5, pp. 1531–1538, 2010.

[27] T. Das, R. Mukherjee, and J. Cameron, “Optimal trajectory planning for hot-air balloons in linear wind fields,” *Journal of guidance, control, and dynamics*, vol. 26, no. 3, pp. 416–424, 2003.

[28] K. Mohsin, M. Odeh, T. Ngo, and T. Das, “Load reduction of wind turbines using integrated torque, collective pitch, and individual pitch control actions*,” in *2023 American Control Conference (ACC)*, 2023, pp. 1505–1510.

[29] T. Hasan, D. Sarker, T. Ngo, and T. Das, “Stabilization of the wind turbine floating platform using mooring actuation,” *IFAC-PapersOnLine*, vol. 56, no. 3, pp. 535–540, 2023, 3rd Modeling, Estimation and Control Conference MECC 2023. [Online]. Available: https://www.sciencedirect.com/science/article/pii/S2405896323024126

[30] D. Sarker, T. Hasan, T. Ngo, and T. Das, “Causality-free modeling of a floating wind turbine semisubmersible platform with validation results,” *IFAC-PapersOnLine*, vol. 56, no. 3, pp. 559–564, 2023, 3rd Modeling, Estimation and Control Conference MECC 2023. [Online]. Available: https://www.sciencedirect.com/science/article/pii/S2405896323024163

[31] A. Gessow and G. C. Myers Jr., *Aerodynamics of the Helicopter*. Macmillan Company, New York, 1952.

[32] H. Glauert, “A general theory of the autogyro,” *Presented by the Director of Scientific Research Air Ministry, Reports and Memoranda No. 1111 (Ae. 285)*, 1926.

[33] C. N. H. Lock, “Further development of autogyro theory - part 1,” *National Advisory Committee for Aeronautics, Reports and Memoranda No. 1127 (Ae. 299)*, 1927.

[34] C. N. H. Lock, “Further development of autogyro theory - part 2: A general treatment of the flapping motion,” *National Advisory Committee for Aeronautics, Reports and Memoranda No. 1127 (Ae. 299)*, 1927.

[35] J. B. Wheatley, “An analytical and experimental study of the effect of periodic blade twist on the thrust, torque, and flapping motion of an autogiro rotor,” 1937. [Online]. Available: https://api.semanticscholar.org/CorpusID:55228999

[36] B. H. Charnov, *From Autogiro to Gyroplane: The Amazing Survival of an Aviation Technology*. Praeger Publishers, Westport CT, 2003.

[37] J. G. Leishman, *Principles of Helicopter Aerodynamics*. Cambridge University Press, 2000.

[38] A. Cuerva, A. Sanz-Andres, J. Mesegeur, and J. L. Espino, “An engineering modification of the blade element momentum equation for vertical descent: An autorotation case study,” *Journal of the American Helicopter Society*, vol. 51, no. 4, pp. 349–354, 2006.

[39] R. Pegg, U. S. N. Aeronautics, S. Administration, and L. R. Center, *A Flight Investigation of a Lightweight Helicopter to Study the Feasbility of Fixed-collective-pitch Autorotations*, ser. NASA technical note. National Aeronautics and Space Administration, 1969. [Online]. Available: https://books.google.com/books?id=0ADF2UkAgngC

[40] P. Talbot and L. Schroers, “A simple method for estimating minimum autorotative descent rate of single rotor helicopters,” Tech. Rep., 1978.

[41] H. H. Heyson, “A momentum analysis of helicopters and autogyros in inclined descent, with comments on operational restrictions,” Tech. Rep., 1975.

[42] D. Seter and A. Rosen, “Dynamics of systems that include wings in autorotation,” *Journal of Dynamic Systems Measurement and Control-transactions of The Asme*, vol. 121, pp. 248–254, 1999. [Online]. Available: https://api.semanticscholar.org/CorpusID:120578415

[43] S. Houston, “Analysis of rotorcraft flight dynamics in autorotation,” *Journal of guidance, control, and dynamics*, vol. 25, no. 1, pp. 33–39, 2002.

[44] B. McCormick, “A numerical analysis of autogyro performance,” in *2002 Biennial International Powered Lift Conference and Exhibit*, 2002, p. 5950.

[45] B. W. Roberts, D. H. Shepard, K. Caldeira, M. E. Cannon, D. G. Eccles, A. J. Grenier, and J. F. Freidin, "Harnessing high-altitude wind power," *IEEE Transactions on Energy Conversion*, vol. 22, pp. 136–144, 2007.

[46] S. Rimkus and T. Das, "An application of the autogyro theory to airborne wind energy extraction," *ASME Dynamic Systems and Control Conference (DSCC), Palo Alto, CA*, October, 2013.

[47] S. Rimkus, "A lab-scale experimental framework for studying the phenomenon of autorotation," 2014.

[48] B. Salih, "An introductory study of the dynamics of autorotation for wind energy harvesting," Master's thesis, University of Central Florida, 2014.

[49] S. Mackertich and T. Das, "A quantitative energy and systems analysis framework for airborne wind energy conversion using autorotation," in *2016 American Control Conference (ACC)*, 2016, pp. 4996–5001.

[50] S. Mackertich, "Dynamic modeling of autorotation for simultaneous lift and wind energy extraction," Master's thesis, University of Central Florida, 2016.

[51] T. K. Das, R. Mukherjee, R. Sridhar, and A. Hellum, "Two dimensional modeling and simulation of a tethered airfoil system for harnessing wind energy," in *Dynamic Systems and Control Conference*, vol. 54754, 2011, pp. 811–818.

[52] T. Noboni, J. McConnell, and T. Das, "Altitude control of a tethered multi-rotor autogyro in 2-d using pitch actuation via differential rotor braking," in *2023 American Control Conference (ACC)*, 2023, pp. 2848–2854.

[53] D. C. Rye, "Longitudinal stability of a hovering, tethered rotorcraft," *Journal of*

Guidance, Control, and Dynamics, vol. 8, no. 6, pp. 743–752, 1985. [Online]. Available: https://doi.org/10.2514/3.20050

[54] S. S. Houston, "Identification of autogyro longitudinal stability and control characteristics," *Journal of Guidance, Control, and Dynamics*, vol. 21, no. 3, pp. 391–399, 1998. [Online]. Available: https://doi.org/10.2514/2.4271

[55] C. Lopez and V. Wells, "Dynamics and stability of an autorotating rotor/wing unmanned aircraft," *Journal of guidance, control, and dynamics*, vol. 27, no. 2, pp. 258–270, 2004.

[56] Y. Ma, Z. Cai, N. Liu, and Y. Wang, "System composition and longitudinal motion control simulation of vehicular towed autogyro," in *2016 IEEE Chinese Guidance, Navigation and Control Conference (CGNCC).* IEEE, 2016, pp. 1018–1023.

[57] D. Rezgui and M. H. Lowenberg, "On the nonlinear dynamics of a rotor in autorotation: a combined experimental and numerical approach," *Philosophical Transactions of the Royal Society A: Mathematical, Physical and Engineering Sciences*, vol. 373, no. 2051, p. 20140411, 2015.

[58] D. Rezgui and M. H. Lowenberg, "Nonlinear blade stability for a scaled autogyro rotor at high advance ratios," *Journal of the American Helicopter Society*, vol. 65, no. 1, pp. 1–19, 2020.

[59] J. Hau, X. Xia, C. Sun, X. Li, Y. Yan, and M. Zhang, "Predictor-based model reference adaptive controller design for the longitudinal motion of a hybrid autogyro," in *2021 33rd Chinese Control and Decision Conference (CCDC)*, 2021, pp. 1146–1150.

[60] S. Rimkus, T. Das, and R. Mukherjee, "Stability analysis of a tethered airfoil," *2013 American Control Conference*, pp. 5601–5606, 2013.

[61] N. D. Kelley and B. J. Jonkman, “Overview of the turbsim stochastic inflow turbulence simulator,” National Renewable Energy Lab.(NREL), Golden, CO (United States), Tech. Rep., 2005.